2014

Study of ^{18}NE using the array for Nuclear Astrophysics and Structure with exotic nuclei

Laura Pratt
Louisiana State University and Agricultural and Mechanical College, llinha2@lsu.edu

STUDY OF ^{18}NE USING THE ARRAY FOR NUCLEAR ASTROPHYSICS
AND STRUCTURE WITH EXOTIC NUCLEI

A Dissertation

Submitted to the Graduate Faculty of the
Louisiana State University and
Agricultural and Mechanical College
in partial fulfillment of the
requirements for the degree of
Doctor of Philosophy

in

The Department of Physics and Astronomy

by
Laura E. Pratt
B.S., Tulane University, 2008
May 2014

I want to dedicate my thesis to Sergeant Stubby of the United States Army of WWI, whose life was an inspiration through the darkest hours of my thesis.

ACKNOWLEDGEMENTS

TABLE OF CONTENTS

ABSTRACT

Reactions involving radioactive nuclei play an important role in stellar explosions, but limited experimental information is available due to difficulties in producing and studying radioactive nuclei. Several facilities aim to provide greater access to these unstable isotopes at higher intensities, but more efficient and selective techniques and devices are required to be able to study many important reactions. The Array for Nuclear Astrophysics and Structure with Exotic Nuclei (ANASEN), a charged particle detector designed by Louisiana State University (LSU) and Florida State University (FSU), was created for this purpose. ANASEN is used to study the reactions important for the αp- and rp- processes with proton-rich exotic nuclei by providing essentially complete solid angle coverage through an array of 40 silicon-strip detectors backed with CsI(Tl) scintillators, covering an area of roughly 1300 cm^2. ANASEN includes an active gas target/detector using a position-sensitive annular gas proportional counter that allows direct measurement of (α,p) reactions in inverse kinematics. Measurements with a partial implementation of ANASEN were first performed at the RESonator SOLenoid Upscale Transmission (RESOLUT) radioactive beam facility of FSU during the summer of 2011. This included stable beam experiments and measurements of the $^{17}F(p,p)^{17}F$ and $^{17}F(p,\alpha)^{14}O$ reactions that are important for understanding the structure of ^{18}Ne and the $^{14}O(\alpha,p)^{17}F$ reaction rate.

We report in detail on one experiment using a 55 MeV beam of ^{17}F to bombard a 2 mg/cm^2 thick polypropylene target. Scattered protons were detected in a silicon strip detector array in coincidence with recoiling heavy ions in a gas ionization chamber that provided clean identification of the reaction channels. The center-of-mass energy for each event was reconstructed from the proton energy and angle, allowing the $^{17}F(p,p)^{17}F$ elastic scattering cross section to be measured between center-of-mass energies of 2.053 MeV and 2.985 MeV. The measured cross sections were fit with theoretical cross sections using phenomenological R-matrix theory. We conclusively observe two resonances. One corresponds to a 1^- state in ^{18}Ne, and we determine $E_x = 6142$ $(5)_{stat}$ $(8)_{sys}$ keV with total width $\Gamma = 45$ (12) keV. We are also able to set a lower limit on the proton partial width to the ground state of $\Gamma_p > 15$ keV at the 90% confidence level. We also observe a 2^- state that we determine to be at $E_x = 6373$ $(8)_{stat}$ $(8)_{sys}$ keV with a total width equal to the partial width to the ground state of $\Gamma = \Gamma_p =$ of 87 (15) keV. While we can not resolve a previously reported 3^- resonance in this same energy regime, we can set a stringent limit on its proton partial width to the ^{17}F ground state of $\Gamma_p < 4$ keV at the 90% confidence level.

CHAPTER 1. INTRODUCTION

Most stars in the Galaxy are observed to reside in systems of two or more stars. Some of these systems are bound in such close orbits that interactions between the stars lead to dramatic events. Novae and X-ray bursts, which occur in such closely interacting binaries, are the most common stellar explosions in the Galaxy. More than 100 known systems in the Galaxy exhibit periodic X-ray bursts lasting 10 to 100 s and recurring on timescales as short as hours. About three dozen nova explosions are observed in the Galaxy each year, and with likely recurrence times of 10^4-10^5 years, there could be millions of these systems in our Galaxy.

Novae and X-ray bursts occur when hydrogen-rich matter from one star in the system (often a star expanding into the giant phase) overfills its gravitational boundary defined by the Roche lobe. Matter can then be transferred onto a compact companion through an accretion disk, where nuclear reactions occur, producing energy and increasing the temperature. In classical nova explosions the compact companion is a CO or ONe white dwarf. Reactions between the hydrogen-rich fuel and the abundant carbon and/or oxygen in the white dwarf provide the bulk of the energy generation through the hot CNO cycle, increasing temperatures at the base of the accretion layer. This rise in temperature is not accompanied by expansion and cooling since pressure is predominantly supplied by electron degeneracy pressure, and a thermonuclear runaway ensues. A chain of proton captures and beta-decays can occur close to the chain of stable isotopes with elements perhaps as heavy as calcium produced with a ONe white dwarf [Sta99]. Reactions that affect the nucleosynthesis of gamma-ray emitters (^{18}F, ^{22}Na and ^{26}Al), heavier elements like silicon and sulfur, and isotopes measured in presolar grains are particularly important for interpreting observations.

X-ray bursts result from a similar Roche Lobe overflow in a binary system, but the accreting compact object is a neutron star supported by neutron degeneracy pressure. Type I X-ray bursts, as illustrated in Figure 1-1, are generally characterized by a fast rise in X-ray luminosity (less than 10 s) caused by the exponential dependence of nuclear reaction rates on temperature, with slower decline (up to 100 s or more) of the energy/light output that is slowed by the slow radioactive decays of the isotopes produced and the time needed for the cooling of the neutron star's surface. After the burst, the binary star system returns to a quiescent state, and this process starts again. In a given X-ray burst system, these explosions typically repeat at intervals of several hours to days, and the explosions
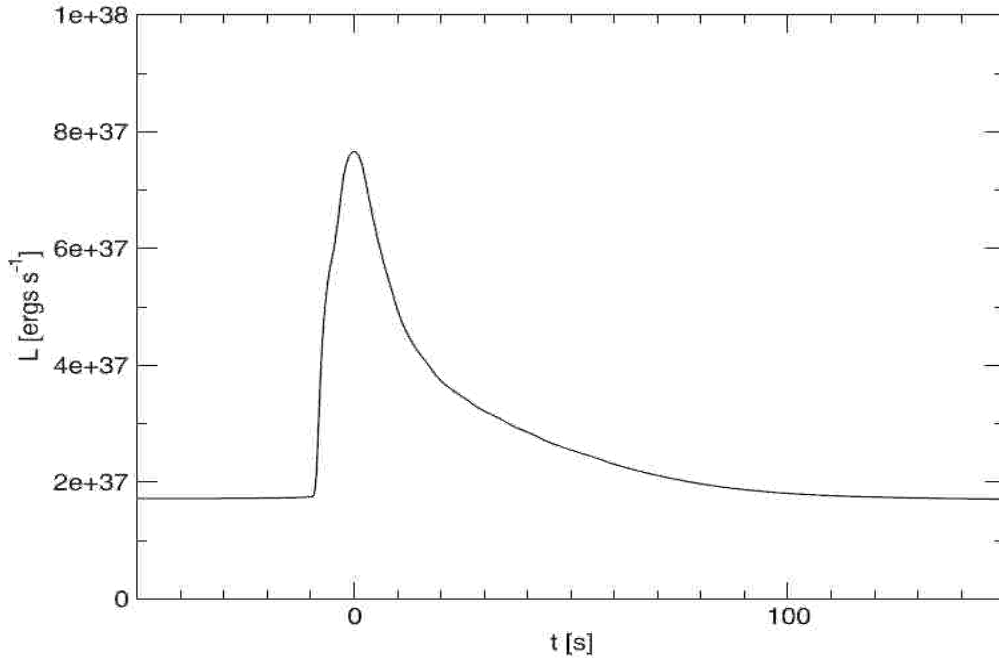
Figure 1-1   Calculated X-ray luminosity of a typical X-ray burst [Fis08].

have been observed to occur at regular intervals for a given system or sporadically. The majority of X-ray bursts are Type I X-ray bursts. Type II X-ray burst binary star systems are rare. There are a few documented cases, which are characterized by a start and stop of the burst with no gradual decay from its peak intensity. These X-ray bursts are believed to be caused by a very high accretion rate from the main sequence star to the neutron star [Sin83].

The greater gravitational potential on the surface of the neutron star results in much higher peak temperatures in X-ray burst explosions than in novae. Sequences of nuclear reactions occur involving nuclei far from stability, and elements as heavy as tin can be synthesized [Sch99]. Here, α-induced reactions, particularly (α,p) reactions on certain light proton-rich isotopes (^{14}O, ^{18}Ne, ^{22}Mg, ^{26}Si, …), and (p,γ) reactions on nuclei closer to the proton-drip line have substantial influence on energy generation and the X-ray light curves. These nuclear reaction rates also determine the composition of the burnt ashes of the explosion, which influences the later evolution of the system, including possibly setting the conditions for superbursts [Str02]. The reaction rates also provide the composition of the neutron star crust [Sch99], necessary to our understanding of binary star systems.

By studying these events, we can gain insights into the structure of white dwarfs and neutron stars and into the evolution of such binary systems. This also provides critical information on accretion and mixing mechanisms that play a crucial role in many astrophysical environments but remain an enigma. A wealth of new observational data is

becoming available from ground-based instruments, and orbiting X-ray and gamma-ray observatories are providing new insights. However, our understanding of novae and X-ray bursts remains limited, in part due to a lack of nuclear data regarding radioactive isotopes that play a key role in the explosions. Sensitivity studies have been conducted using astrophysical models to identify the most important nuclear reactions occurring in novae and X-rays bursts [Par08]. The rates of reactions are individually varied in the astrophysical models [Heg07, Woo07], and the impact on observables like the energy generation (light curve) and elements produced is studied. The results from such sensitivity studies do depend upon assumptions of the particular astrophysical model and may not be sensitive to effects that arise from a coupling of several reactions [Gal08, Wor13, Zam12]. However, some individual reactions do show a prominent impact on astrophysical models, and the importance of such reactions for astrophysics is manifest.

Many of the nuclear reactions that have been shown to have an important impact on novae and X-ray bursts involve radioactive nuclei, and the rates of such reactions often have great uncertainties. Low-energy beams of radioactive nuclei are now being developed that provide an opportunity to address these important uncertainties for the first time. Measurements using low-energy radioactive ion beams promise to significantly improve our understanding of the measured optical light-curves from stellar explosions, of observations by orbiting X-ray and gamma-ray observatories, and of neutron-star composition. The U. S. Nuclear Science Advisory Committee recommended that to "*measure properties of and reactions on selected proton-rich nuclei in the rp-process to determine radionuclide production in novae and the light output and neutron star crust composition synthesized in X-ray bursts*" [SPM08] is one of the key milestones for the U.S. Nuclear Science Program.

In these cases, the nuclear reaction rate, <σv>, is the quantity of interest for astrophysical models. The reaction rate describes, for a given temperature, the number of nuclear reactions occurring per time per particle pair. This quantity is the integral of the cross section multiplied by the relative velocity and weighted by the speed distribution. Since the energy distribution of particles is thermal in a stellar environment, a Maxwell-Boltzmann Distribution is assumed.

$$\langle \sigma v \rangle = \sqrt{\frac{8}{\pi \mu}} (kT)^{3/2} \int_0^\infty \sigma E e^{-E/kT} dE \qquad (1\text{-}1)$$

Equation 1-1 is the reaction rate written with the Maxwell-Boltzmann Distribution. In this equation, μ is the reduced mass of the system. The Boltzmann constant, k, is multiplied by the temperature of the system, T, and kT is indicative of the most probable relative energies at a given temperature. The cross section of the reaction is

represented by σ, and E is the center-of-mass energy. The most probable energies for astrophysical temperatures are lower than the classical energy required to overcome the Coulomb repulsion for charged particles. The cross section for charged-particle reactions is then proportional to the probability of tunneling through the Coulomb Barrier, $e^{-\sqrt{\frac{E_g}{E}}}$, resulting in an exponential dependence of the cross section, where $E_g = \frac{2\mu}{\hbar^2}(\pi Z_1 Z_2 e^2)^2$. Often the cross section is rewritten as the tunneling probability multiplied by another factor, called the astrophysical S factor. The introduced S factor accounts for all other nuclear effects in the cross section [Rol73].

From this point the reaction rate can be written as the integral of the Maxwell-Boltzmann and Coulomb exponentials with an S factor, and integrated over all energies, as seen in Equation 1-2. The Maxwell-Boltzmann Distribution is proportional to $e^{-\frac{E}{kT}}$. This creates an integral of two competing exponentials, which results in a relatively narrow range of energies that will have the largest effect upon the reaction rate. This range is called a Gamow Window, and is illustrated schematically in Figure 1-2.

$$\langle \sigma v \rangle = \sqrt{\frac{8}{\pi\mu}}(kT)^{\frac{3}{2}} \int_0^\infty S e^{-\sqrt{E_G/E}} e^{-E/(kT)} dE \qquad (1\text{-}2)$$

The energy range of the Gamow window is so low in energy that direct measurements have historically been inaccessible due to the small cross sections that arise from the small probabilities for penetrating the Coulomb barrier at such low energies. The best estimates were often obtained from measurements taken over a range down to the lowest possible energy and used for extrapolation. This method leads to erroneous results in cases where resonances are present without additional information. Knowledge of possible resonance energies, spin-parities, and widths are necessary to create an accurate estimation of the reaction rate. Indirect and direct measurements are utilized to provide complementary information to improve our understanding of the nuclear reaction rates.

We have developed a charged-particle detector array, the LSU-FSU Array for Nuclear Astrophysics and Structure with Exotic Nuclei (ANASEN) that enables reaction studies with radioactive ion beams to measure the resonant properties that are needed to understand the most important reactions occurring in novae and X-ray bursts. ANASEN is designed to be used primarily for measurements of (α,p) reactions and indirect studies of resonant properties using reactions like proton elastic and inelastic scattering using radioactive ion beams. Measurements of (α,p) cross sections will directly determine the rates of (α,p) reactions that are important in X-ray bursts and will
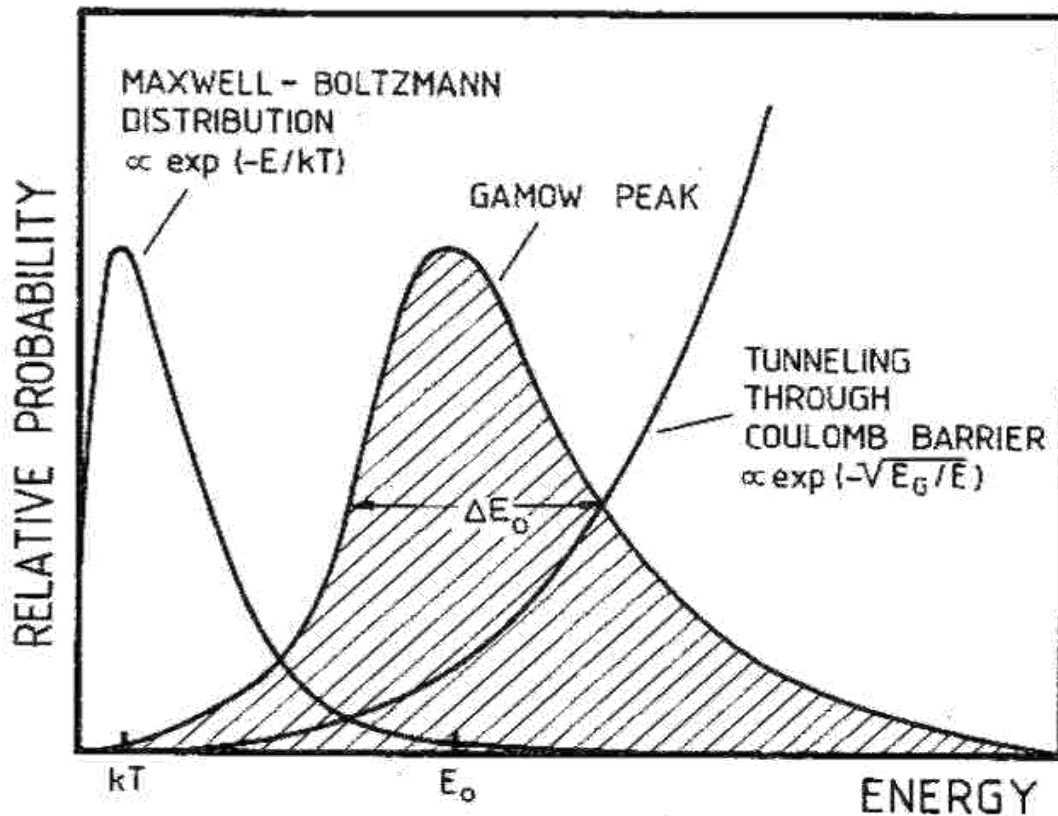
Figure 1-2   Relative probabilities schematically illustrated as a function of energy. Figure reproduced from [Rol88].

provide a critical test of statistical models that provide the only basis for current estimates of most (α,p) reaction rates of interest. Measurements like proton elastic and inelastic scattering are important to indirectly determine the properties (energies, angular momenta and proton partial widths) of some of the nuclear levels that are important in (p,γ) and (α,p) reactions and are not accessible by direct measurement. While direct measurements of (p,γ) reactions are needed at the most important resonances in these reactions, such measurements are especially difficult, requiring both high radioactive beam intensities and substantial experimental infrastructure (like large recoil separators). More straightforward studies like proton elastic and inelastic scattering are needed first to understand the energy level structure of these nuclei and to help identify what are, in fact, the most important resonances.

This dissertation focuses on the development of the silicon-strip detector array and electronics that is the heart of ANASEN, on the development of heavy ion recoil chambers (HIRC) for ANASEN, and on the first measurement with radioactive ion beams using an early implementation of ANASEN. A brief overview of ANASEN is provided in Chapter 2. In Chapter 3 we describe the development and testing of the silicon strip detector array for ANSAEN. The development of the HIRC is discussed in Chapter 4.

Chapter 5 delves into the motivation for studying ^{18}Ne, while Chapter 6 examines the ^{17}O test experiment. Next, we explain the ^{17}F+p experiment and R-Matrix analysis drawn from the data in Chapters 7 and 8. To finish we report on the development of ANASEN and its new home at MSU's National Superconducting Cyclotron Laboratory in Chapter 9 and conclude with a brief summary in Chapter 10.

CHAPTER 2. ANASEN OVERVIEW

The Array for Nuclear Astrophysics and Structure with Exotic Nuclides (ANASEN) is a multi-configuration detector system that uses 5 different types of detectors (proportional counter, QQQ3 silicon detectors, Super X3 silicon detectors, CsI(Tl) scintillating crystals, and a heavy ion recoil detector) to allow studies with high efficiency and resolution of reactions utilizing new low intensity exotic beams. A unique feature of ANASEN is the capability to include a position-sensitive proportional counter surrounding the beam axis in an active-target mode. This allows very thick gaseous targets to be used without compromising the energy resolution. Silicon-strip detectors (manufactured by Micron Semiconductor) surround the proportional counter in a barrel configuration with up to 3 rings of 12 rectangular (75x40.3x1 mm) detectors. An annular segmented silicon strip detector array at forward angles closes one end of the barrel. Backing the silicon detectors are trapezoidal Thallium-doped Cesium Iodide, CsI(Tl), scintillation crystals that provide full energy information for even high energy protons. A heavy ion gas ionization chamber is location downstream of the silicon detector barrel around $\theta_{lab}=0°$ to provide coincident detection of heavy ions at very forward angles.

Figure 2-1 is a SolidWorks representation of the inner pieces of ANASEN beside a photo of the assembly. The front of the chamber has a 2 μm thick Ti (or Kapton) foil window where the beam enters the chamber from the vacuum of the beam line. The window can support a pressure differential of up to 500 Torr without breaking. As the beam travels through the chamber, the incident ions can react with nuclei in the target gas, producing intermediate compound nuclei that typically decay by emission of charged particles. The emerging light particles are measured as they pass through the proportional counter, providing position and energy loss information. Then the light particles travel into a silicon detector, giving a second position and energy measurement. Protons with energies greater than about 12 MeV punch through the silicon and deposit the remainder of their energy in the CsI(Tl) crystal detector. From the 2 position measurements and the energy measurement in the silicon, the kinematics of reactions are accurately determined on an event-by-event basis. The inner proportional counter can also be removed and replaced with a solid target for some studies.

2.1 Proportional Counter

The position-sensitive gas-filled proportional counter extends along the beam axis for 43 cm. The gas is chosen for each experiment as the target and the detector medium. The proportional counter is made of 5 rings of wires
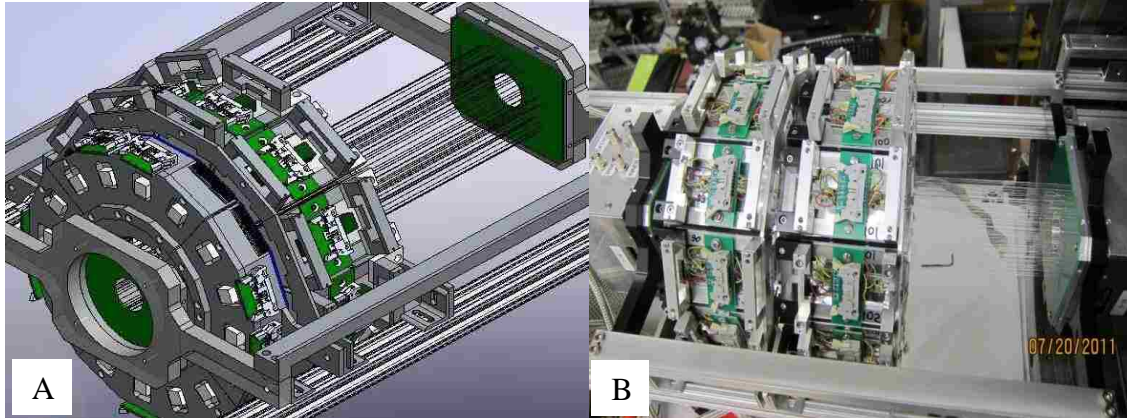
Figure 2-1   Solidworks design [A] and photograph of [B] ANASEN showing CsI detectors surrounding silicon array and proportional counter.

suspended between two circuit boards to which they have been soldered. The central ring of wires contains 19 spring-loaded anode wires equally spaced 3 cm fazSrom the beam axis, operated at high positive voltage, and made up of 7 μm diameter carbon nanofiber. This material has high, uniform resistivity of 4 kΩ/cm, good position resolution, and high gain. Each anode wire is interspersed with cathode (grounding) wires made of gold-plated tungsten. The second and fourth rings of wires are all grounded, to form a trapezoidal pattern Faraday cage around the anode wire. The innermost (and outermost) ring of wires maybe charged to a positive voltage to suppress delta electrons from drifting into the proportional counter region. Figure 2-2 shows the electric field simulation for the proportional counter configuration. A photograph looking down the center axis of the proportional counter is in Figure 2-2. A heavy charged ion going through the proportional counter region will leave an ionized trail of gas. The electrons are accelerated by the high positive voltage and create an avalanche of charged gas near the wire. The position of the traveling particle is determined by charge division method using the signal from both ends of each anode wire.

2.2 Silicon Detectors

Surrounding the proportional counter is a barrel of silicon detectors that we have developed in conjunction with Micron Semiconductor. Silicon strip detectors were chosen for ANASEN because a large area can be covered while achieving precise energy and good position information. The Model Super X3's are double-sided, segmented, 75x40.3x1 mm silicon-strip detectors. This design was adapted from the X3 detectors used for ORRUBA [Pai07]. One feature of the Super X3 detectors is that the back ohmic faces of the detector are segmented into four segments
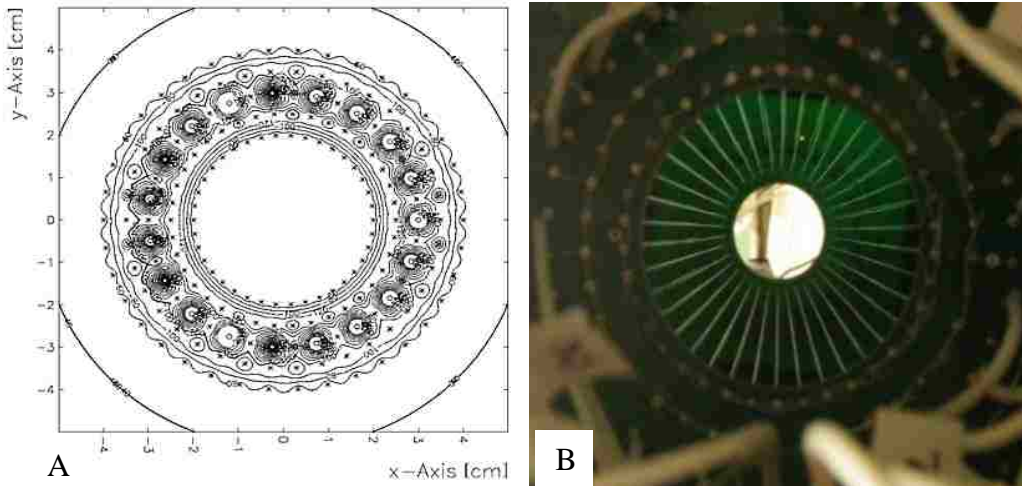
8

Figure 2-2 Electric field calculation for the proportional counter [A]. Photograph of the proportional counter [B].

of 18x40 mm in dimension that are used to determine the energy independent of position. These detectors have four resistive strips that are 75 mm long and 10 mm on the front face. There are 12 signals, 8 front and 4 back, for each of these detectors. A CAD rendering featuring the front side of a Super X3 detector is shown in Figure 2-3. We tested the performance of the first suite of detectors using a [241]Am source of alpha particles. The testing of the detectors is described in sections 3.2 through 3.6. Comparison of signals from the front horizontal resistive strips with the full energy measurement provides position resolution of about 1.5 mm along the beam axis.

Annular double-sided silicon detectors were designed to cover a large fraction of the angular range for forward angles. These detectors are double-sided with an inner and an outer diameter of 55 and 99 mm, respectively. This design creates a 210 cm^2 coverage area, with the largest radius possible using 4 pieces of silicon (using 15 cm wafer technology). The QQQ3 design has 16 front rings and 16 back segments with 4 quadrant detectors creating a complete set. The front rings and the back segments are depicted in the CAD rendering featured in Figure 2-4. Both of the segmented silicon detectors, Super X3 and QQQ3, are 1 mm thick, and high energy protons can punch through the Si in some high energy cases, $E_p > 12$ MeV [Kno00].

2.3 CsI(Tl) Crystals

We have worked with SCIONIX to design trapezoidal-shaped 2 cm thick CsI(Tl) crystals, to ensure that the full energy is measured for particles that can penetrate through the silicon array. Nearly all particles of interest stop in the silicon strip detectors, and the choice of CsI provides a much more cost effective solution (than adding another layer of silicon) for identifying events that penetrate through the silicon layer. There are two different geometries of

9
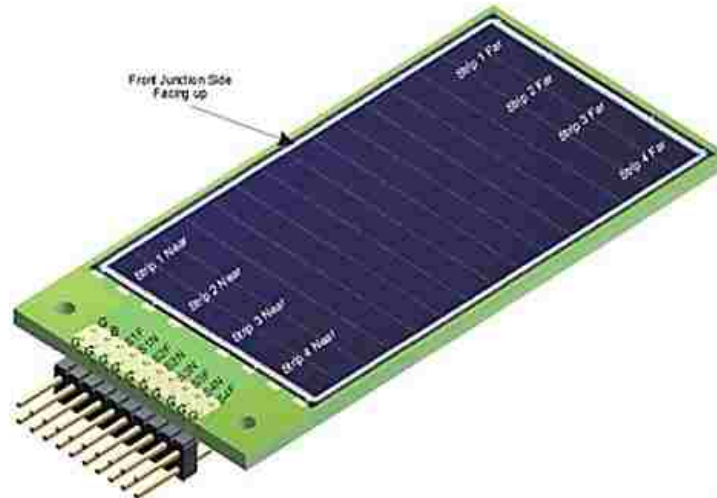
Figure 2-3   CAD rendering of a Micron Super X3 silicon detector, four 75 mm long strips run from the near end to the far end as indicated.
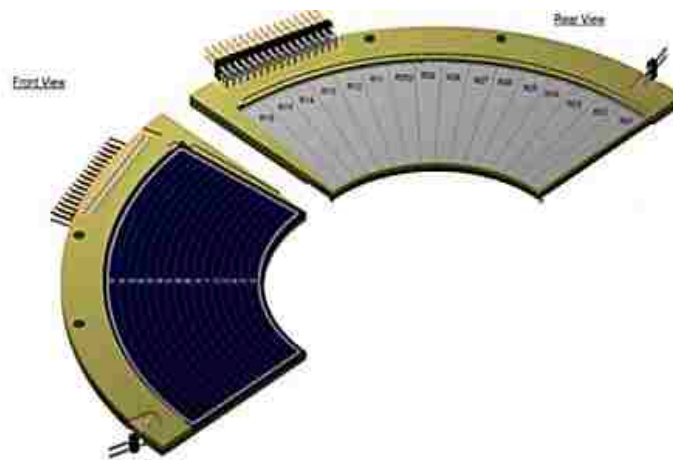
Figure 2-4   CAD rendering of a QQQ3 detector.

CsI(Tl) detectors used in ANASEN, shown in Figure 2-5. Type I has been designed to fit behind a Micron Super X3 detector. The face of the crystal will cover the back side of the silicon detector and will extend outward so that the experimental particles will not leave the crystals on the sides. Type II has been designed so that an arrangement of 16 crystals can fully cover the downstream silicon detectors in pie shaped segments, four for each QQQ3 detector. Each crystal is wrapped in aluminized mylar, and has built-on preamps which are read out by 2 P-type, Intrinsic type, N-type (PIN) diodes. The energy resolution with a ^{241}Am source is 7% under optimal noise conditions as shown in Figure 2-6. This resolution is limited by variation in the efficiency of light collection due to geometry and scintillator properties.
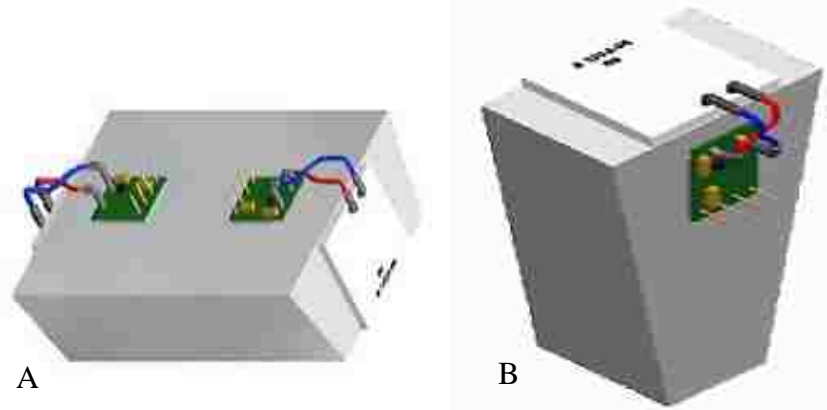
Figure 2-5   CAD rendering of CsI(Tl) detectors, type 1 [A] and type II [B].
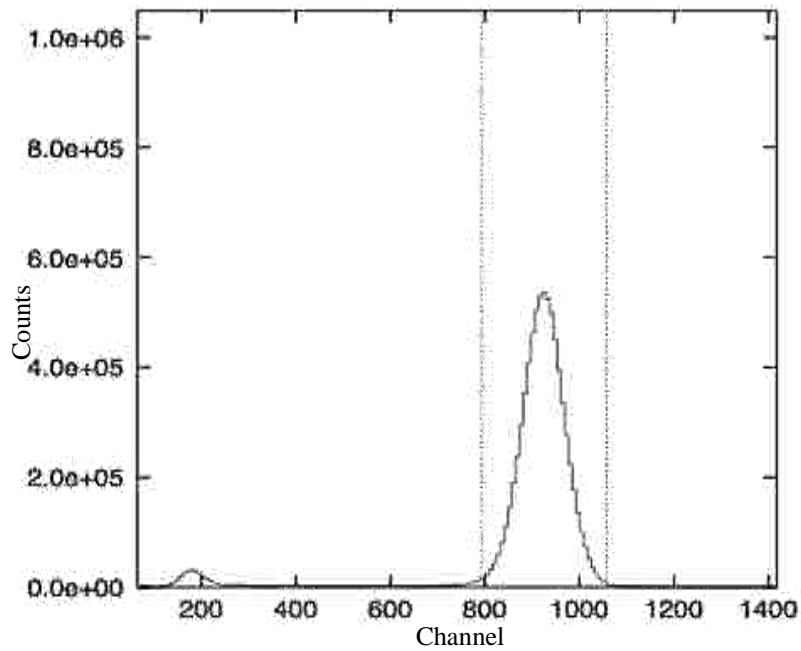
Figure 2-6   Energy spectrum of a [241]Am source taken with a CsI(Tl) detector.

2.4 Heavy Ion Recoil Counter (HIRC)

A HIRC was developed for beam diagnostics, and for coincident heavy ion detection in some experiments. During reactions with a heavy beam on a light target, recoiling heavy ions are emitted at forward angles at energies comparable to that of the incident beam. The HIRC is mounted around $\theta_{lab}=0°$ downstream of ANASEN and is separated from ANASEN by a thin Mylar window. This counter provides coincidence detection of heavy ions with high efficiency for some reactions, and is most effective when a solid target is used that fixes the location of the reaction vertex. The gas in the heavy ion gas ionization chamber can be independently controlled from that in the

ANASEN active-target. The use of a gas ionization detector allows the Z of heavy ions to be determined by their relative energy loss. The robust nature of the design also allows it be used under high count rate conditions without damage.

The HIRC is housed in a NW250 chamber that holds ten pairs of alternating anode and ground planes oriented perpendicular to the beam axis, spaced ~ 17 mm apart. The first version of the detector used in the experiments described here consisted of 10 anode copper planes (20x20 cm outer dimensions, 11 cm window) with 1 mm spaced wire grids, Figure 2-7. Incident particles will travel through a 10 mm dead zone of gas before the first plane. The heavy ion recoil chamber typically uses isobutane gas to get the best energy resolution possible, or uses CF_4 where high count rates are needed. In front of the chamber there is a laterally moveable beam stop suspended on a wire that can be used to prevent the direct beam going into the chamber.

2.5 Electronics

With the combination of the proportional counter, silicon detectors, and CsI(Tl) detectors, there are roughly 800 channels of electronics in the full configuration of ANASEN. To deal with this high channel count in a cost effective manner, ANASEN utilizes Application-Specific Integrated Circuits (ASICs) of the HINP16C design by Washington University [Eng07].

Each HINP16C ASIC handles the pulse-shaping, timing, and triggering of 16 channels of data. The system as a whole has 2 ASICs HINP16C chips per board, with 16 boards in the system, handling up to 512 channels in one motherboard, Figure 2-8. Analog signals from all channels are multiplexed into XLM flash ADC's ANASEN uses 2 motherboards and XLM modules. A VME-USB Wiener interface is used to send the collected digital data from the front end processor using National Superconducting Cyclotron Laboratory Data Acquisition system that is used at the ReAccelerated 3 MeV/u Beam Line (ReA3) at NSCL and at the Fox Accelerator Laboratory at FSU.

External preamplifiers are used to optimize the energy resolution and dynamic range. We developed a 72-channel preamplifier system for the silicon detectors based on the Indiana University's LASSA preamplifier chip; with a gain of 27 mV/MeV and a 30 μs fall time that matches the shaping of the HINP16C ASICs [Dav01]. In Figure 2-9 is an electronic schematic of a cross section of a Super X3 with the electronics of the preamplifier system. There is an auxiliary resistor built into each channel of the preamplifier box which augments the detector resistance from the end of front side strip before it reaches the preamplifier system. We defined this additional

Figure 2-7   A photograph of the grids for the heavy ion recoil chamber being assembled to a NW250 flange.

Figure 2-8   Photograph of the ASICs HINP16C system with 5 chip boards installed.
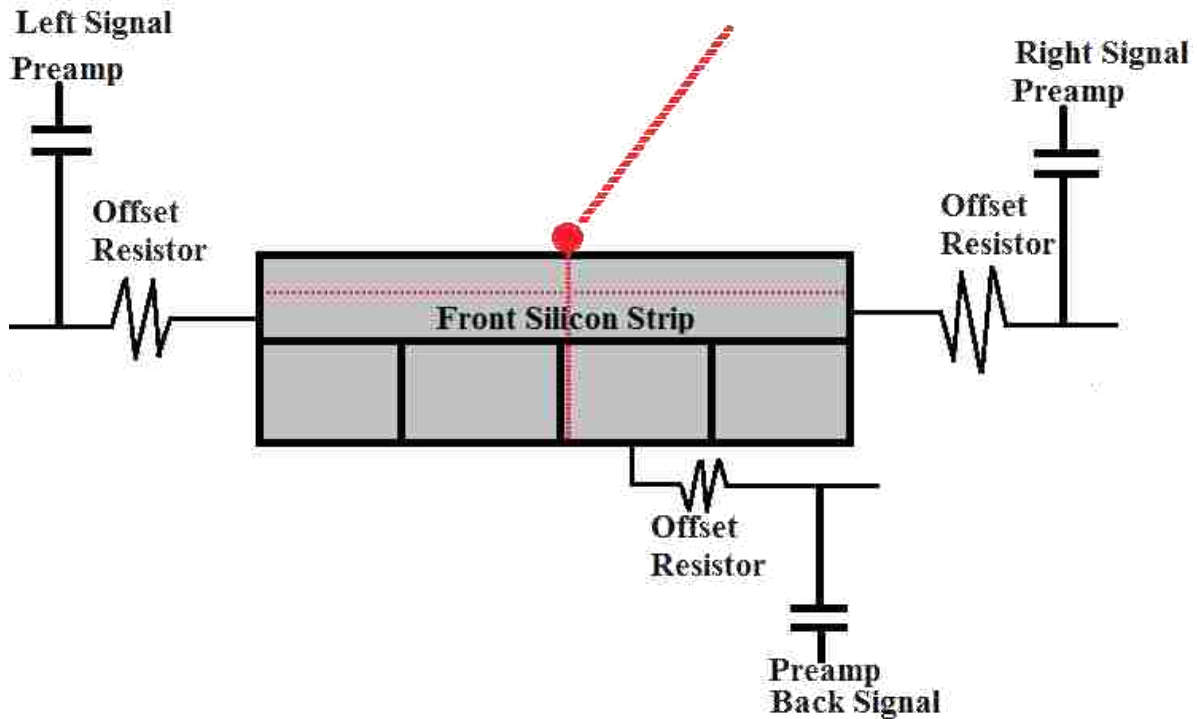
Figure 2-9   An electronic schematic of a front silicon strip with offset resistors and a charged particle interaction
with signal division.

resistor as an "offset resistor" that helps make the relative resistance from the 2 sides closer to the same value for

each silicon strip. To simplify the system, all the channels have the same valued offset resistor. In Chapter 3, the

tests for various resistor values for this system are outlined and the decision to use a 50 Ohm offset resistor is

explained.

This new preamplifier configuration is able to pack 72 signals in a housing configuration that is only 2.5" thick.

With a complete ANASEN implementation comprising roughly 800 signals, handling a high-density of electronics

without losing resolution becomes a priority. We designed a circuit board feed-through to map 6 Super X3 detectors

through of regular density Insulation Displacement Connector (IDC) to high density IDC cabling to get the signals

out of the vacuum. Signals are also regrouped so that the Micron Super X3 signals go into the preamp box in the

most researcher friendly arrangement.

CHAPTER 3. SILICON DETECTOR ARRAY DEVELOPMENT

3.1 Super X3 Calibrating Setup

The initial performance testing of the Super X3 detectors was performed at LSU using a ^{241}Am alpha source, which has nearly monoenergetic alpha emission at 5.48 MeV. All of the detectors were characterized in a similar fashion, and the performance of all the Super X3 detectors was found to be fairly consistent. Here we will describe in detail the testing procedure and present results for the first two prototype detectors, nicknamed "Charm" (Micron Serial #2792-12) and "Strange" (Micron Serial #2792-20), whose performance was typical.

The detectors were mounted in NW 250 mm International Standards Organization- Large Flange 6-way cross (NW250 ISO-LF 6-way cross) with the alpha source located roughly 40 cm away from the detectors. The system was pumped down to the low 10^{-7} Torr scale using a combination of a Leybold dry roughing pump and a turbo molecular pump mounted directly on the cross. A special ribbon cable was constructed that allowed Charm and Strange to be connected to a single, standard 2x20 (0.254 cm pitch) vacuum feedthrough. The front-end LASSA preamplifiers developed for ANASEN were used. The preamplifier motherboards were designed to mount directly to the chamber to amplify the signals as soon as possible after exiting the chamber that effective serves as a Faraday cage. In our initial testing, we used 15 mV/MeV preamplifer chips, but we ultimately adopted higher gain chips (30 mV/MeV) for ANASEN to improve our energy and position resolution.

A schematic of the electronics setup used in the testing is shown in Figure 3-1. Two Mesytec Nuclear Instrumentation Module (NIM) shaping amplifiers were used in the tests. A Mesytec 16 fold Spectroscopy Amplifier with Discriminators and Multiplicity Trigger (STM-16+) was used for the front signals (negative polarity) from both detectors, and a Mesytec 8 Channel Spectroscopy Amplifier with Timing Filter Outputs (MDS-8) was used for the 8 back signals (ohmic, positive polarity) from both detectors. A short ribbon to a lemo adapter was constructed to connect the backside signals to the MDS-8. All signals were processed using a 32-channel CAEN's Model V785 peak-sensing Analog-to-Digital Converter (ADC). The event trigger and gate for the ADC were generated using the common Timing Filter Amplifier (TFA) timing output of the MDS-8. The timing output was first sent to a Phillips 779 amplifier (10x amplification) then to a Phillips 715 Constant Fraction Discriminator (CFD). A 607 cm long Radio Guide-174 Type (RG174) lemo cable was used for the delay of the CFD to match the slow rise time of the silicon pulses. The CFD threshold was set to approximately 35 mV.
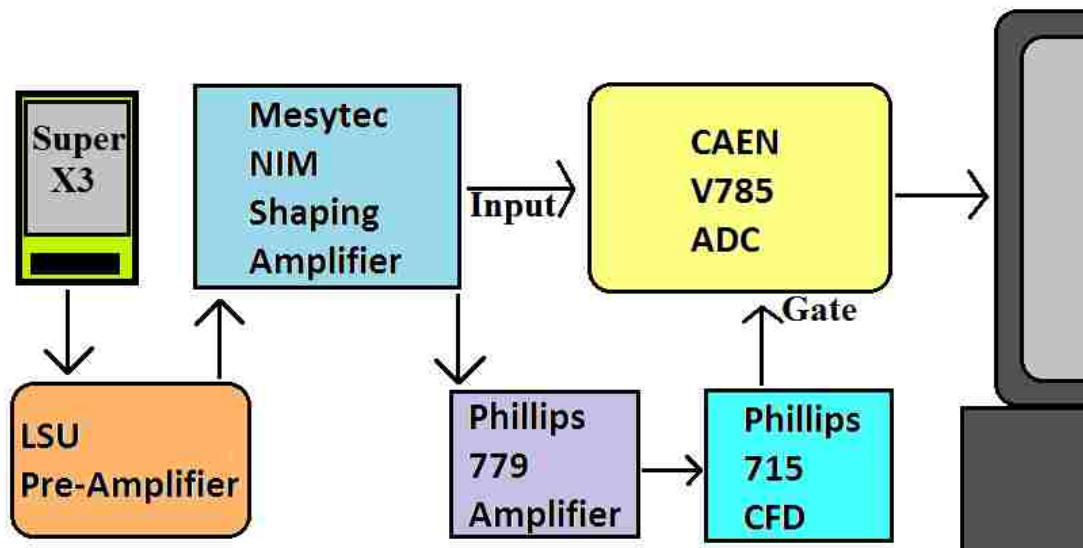
Figure 3-1   A drawn electronic schematic of the calibration test.

Care was taken to reduce noise in the system to probe the energy resolution of the detectors and front-end electronics independent of external noise. Pickup of Radio Frequency (RF) noise from the turbopump was common to all the channels of electronics, but was suppressed by judicious grounding, braiding the LSU Si-36 preamplifier box ground to one of the MDS-8 lemo connectors and to the frequency converter of the turbo pump. External shielding of some cabling, especially the ribbon cable connecting the preamplifier system to the shaping amplifiers, was also helpful in reducing noise pickup. Figure 3-2 to Figure 3-5 below illustrates the setup.

The Oak Ridge Physics Acquisition System (ORPHAS) with a Motorola Model MVME-5500 Single-board computer for VME (Versa Module Europa) bus was used to collect digital data from peak sensing ADCs. A FORTRAN program *anasen.f* was written using the SCANOR library as part of the ORPHAS package to process the data.

3.2 Super X3 Front Side

The "front" (junction or p-type) of the Super-X3 detectors is divided into four strips 1 cm wide by about 7.5 cm in length. The front of the detector has a resistive layer, and a wire bond at each end of each strip connects to a pad on the PCB holding the detector. The size of the two signals can then be compared by resistive charge division to determine the position of the particle on the detector. Histograms of data from the [241]Am source are shown in Figure 3-6. The signals for each end of the strip are shown, which are indicative of the position since the source energy is nearly mono energetic.

16
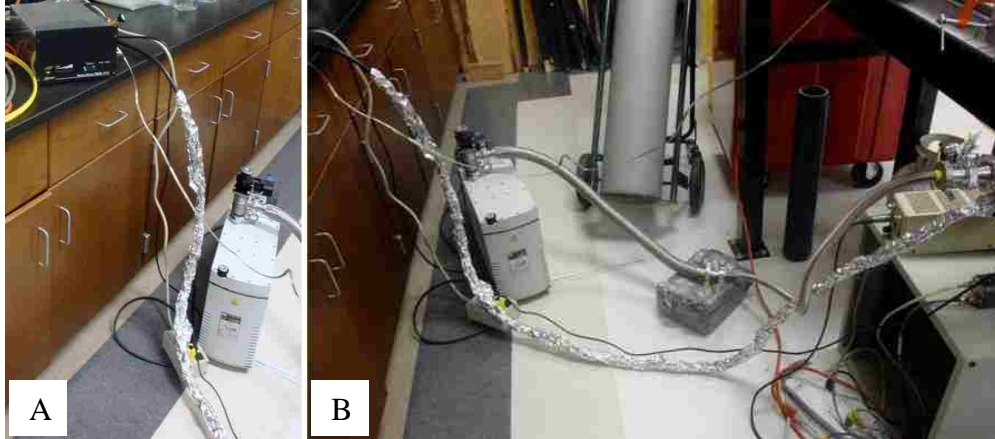
Figure 3-2   It was beneficial to place the turbo pump frequency converter [A] as far as possible away from the chamber, with a robust ground connection (using a braid) between the frequency converter and the pump/chamber to reduce noise[B].
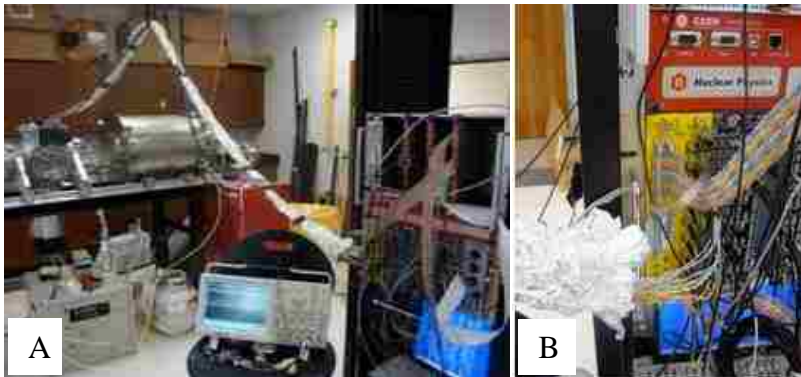
Figure 3-3   The ribbon and grounding cables were bundled and encased with aluminum foil. There is a photograph of the transition from the chamber to the electronics crate [A], and then a photograph zoomed into the electronics crate [B].
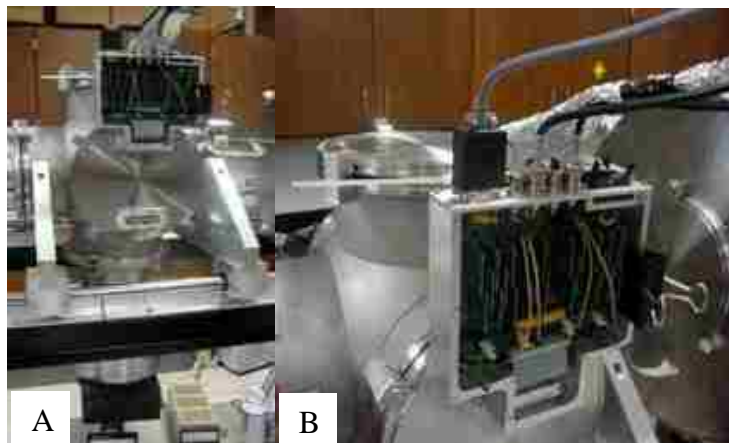
Figure 3-4   A photograph of the LSU Si-36 preamplifier box connected to the chamber [A]. A photograph close-up of the far left power cable; there are two BNC connectors for the silicon detector high voltage, and ribbon cables encased in aluminum foil [B].
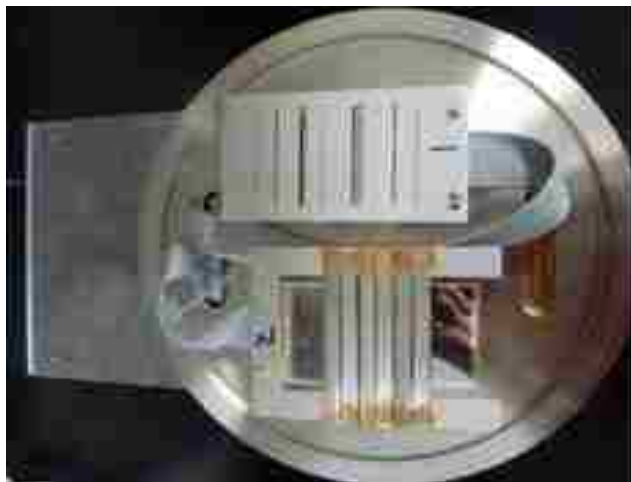
Figure 3-5   Close-up of the setup inside the chamber, illustrating connection of the special cable ribbon cable.
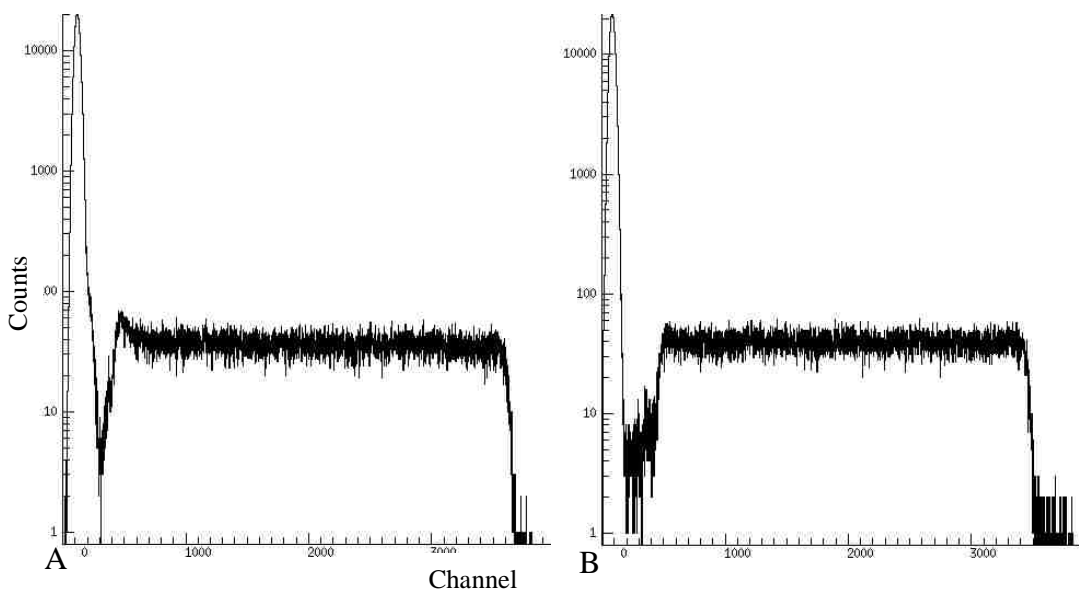
Figure 3-6 Ungated sample spectra from left [A] and right [B] ends of a strip on detector "Charm".

The total energy from the alpha particle can be calculated as the sum of the left and right sides of each front strip. Sample spectra from one strip of the "Charm" detector are shown in Figure 3-7. The position of the alpha particle is calculated by taking the ratio of the signal from the left side to the total energy and multiplying by 1000. The total energy can be taken as either the sum of the front signals or the signal from the back (non-resistive face). A two-dimensional plot of total energy versus position, one side compared to the total energy, is also shown in Figure 3-7 for a sample strip of "Charm". The electronic gains for each side of the strip are slightly different, and gain coefficients have been added in software to match the gain for the two ends of the strip, assuming linear gain with energy.

18
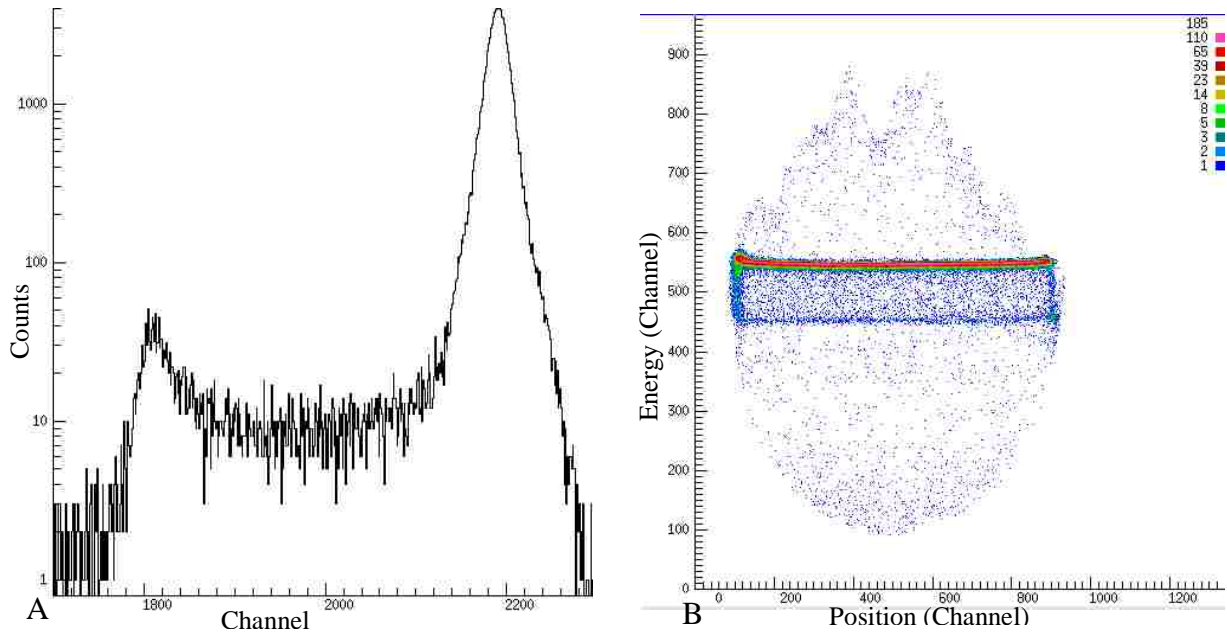
Figure 3-7 The energy spectra (Left+Right) of a front strip [A]. Graph of energy versus position for a front strip of the detector "Charm" [B].

The full energy peak has a Full-Width Half-Maximum (FWHM) of 26.3 channels with a centroid located at channel 2191.2. Those values are used to calculated an energy resolution of 66 keV. Figure 3-8 shows the same energy versus position plot as Figure 3-7, except zoomed on the y-axis range. This better shows the dependence of the energy on position. Derivations from linearity are clearly observed in response to the position of the alpha on the silicon strip.

The data shown in Figure 3-8 is the same as that in Figure 3-7, but with an expanded energy scale, and was taken with 50 Ω offset resistors. The total energy peak was fit with a Gaussian function with a linear background to extract the centroids and widths (FWHM). The resolution was calculated by the Equation 3-1. The energy resolution determined from each resistive strip is tabulated in Table 3-1.

$$\frac{FWHM}{Centroid}(5485.6\ keV) = resolution\ in\ keV \tag{3-1}$$

Near the ends of each strip there is significant nonlinearity. A selection gate was added to the energy-versus-position spectra to allow for selection of events corresponding to only a small range of positions on the detector. Figure 3-9 shows an example of the gate, added to select events that correspond to only a small range of positions near the middle of the strip. The comparison of the energy (Left+Right) from this narrow range of positions allows us study the energy resolution in response to the change of offset resistors. This also helped analyze the nonlinearities found at the edges of the detector. Where this effect is small, it was most apparent with 50 Ohm offset

19
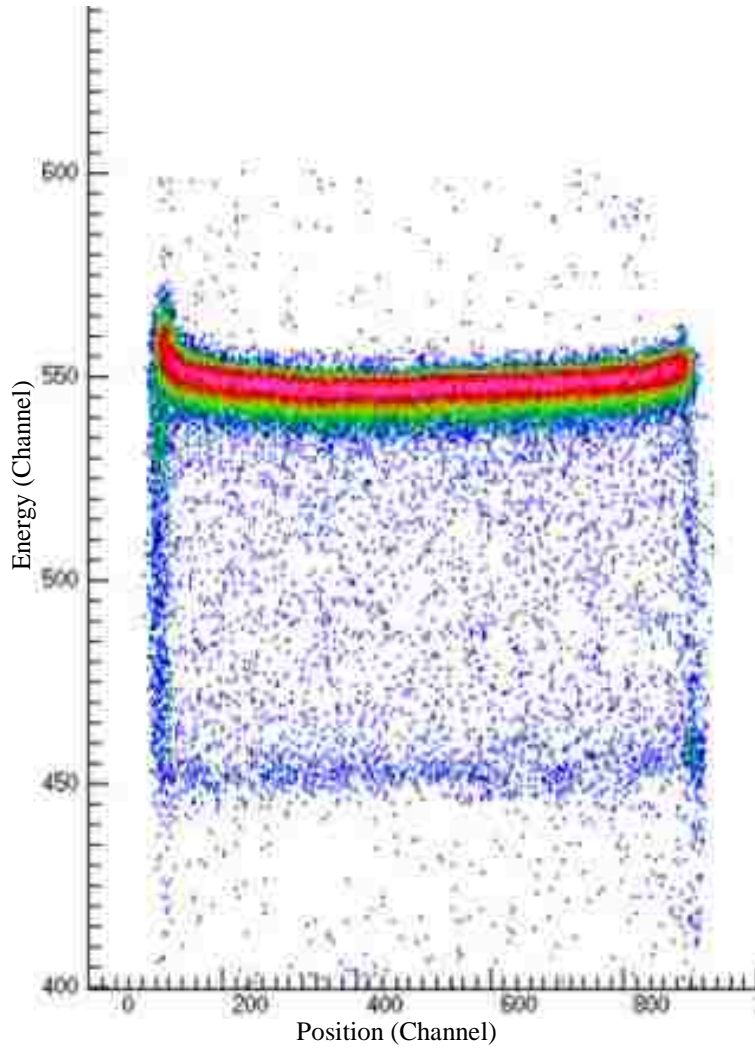
Figure 3-8 Energy plotted as a function of position for a sample strip in Detector "Charm", zoomed in from the center part of Figure 3-7.

Table 3-1 Measured energy resolution for Left+Right from each strip.

Graph	Detector	Centroid (chan)	FWHM (chan)	Resolution in keV
201	Charm strip 1	2191.2	26.5	66.4
202	Charm strip 2	2189.5	32.6	81.7
203	Charm strip 3	2189.7	27.6	69.2
204	Charm strip 4	2188.2	26.4	66.1
Avg				70.9
205	Strange strip 1	2182.2	26.5	66.6
206	Strange strip 2	2190.7	20.6	51.7
207	Strange strip 3	2193.2	30.5	76.2
208	Strange strip 4	2187.7	27.5	69.1
Avg				65.9
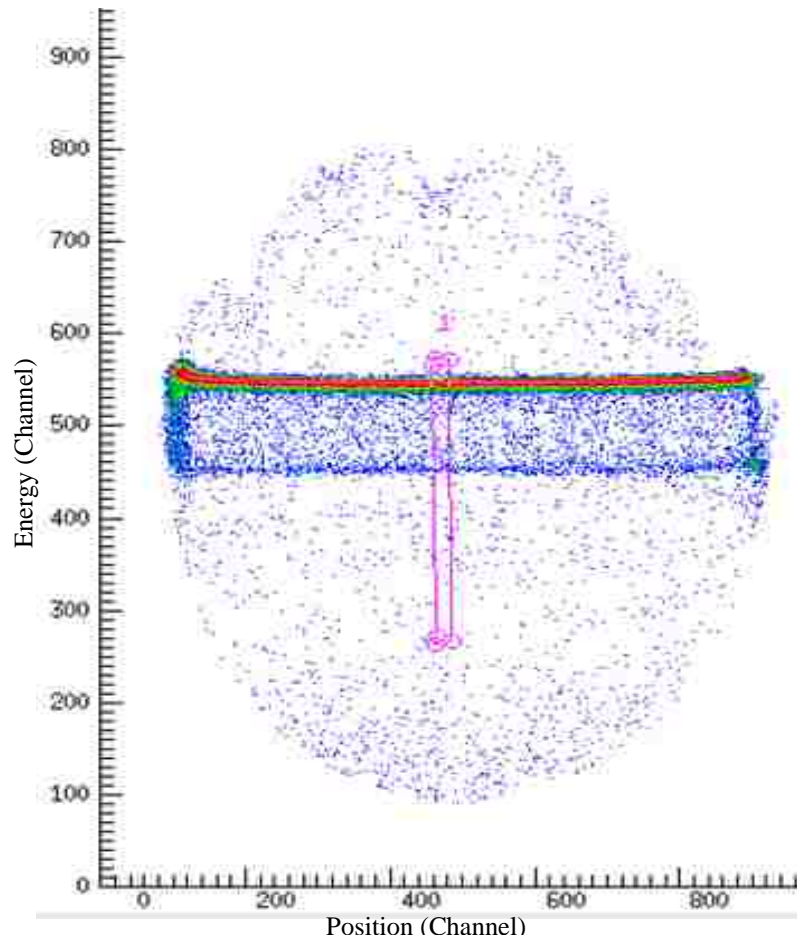
Figure 3-9   A sample energy versus position plot, illustrating the gate that was used to the study the energy resolution for a narrow range of positions.

resistors. In Figure 3-10 we show both the energy (Left+Right) for all events, and the energy only within the selection gate is also shown. We compared the centroid and width for the energy (Left+Right) determined for all events (having both a Left and Right signal above the ADC threshold) and for only those events falling within the gate illustrated in Figure 3-9. It was clear that there is a significant decrease in resolution, caused by nonlinearities in energy response versus position. However, this effect seems to arise predominantly from the very ends of the strip.

3.3 Super X3 Back Side

There are four backside signals from each detector, which were calibrated in the software with linear coefficients. The gain-matched energy spectra are found in plots from the back strips in Figure 3-11. The gain of each channel was set to put 10 MeV in channel 4000, or 2.5 keV/channel, which was done for the Left+Right energy spectra. The energy resolution from the back side strips was far superior to that from the front side strips, and the 3

21
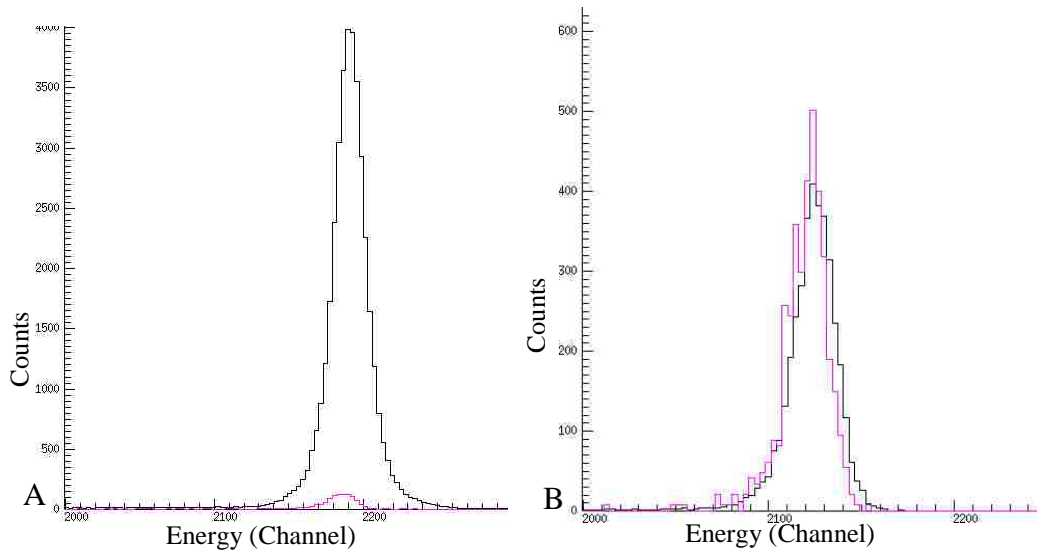
Figure 3-10 Total energy for all events (black) and limited to events within the gate shown in Figure 3-9 [magenta] [A]. The two curves have been arbitrarily normalized to allow for easier comparison of the shapes [B].
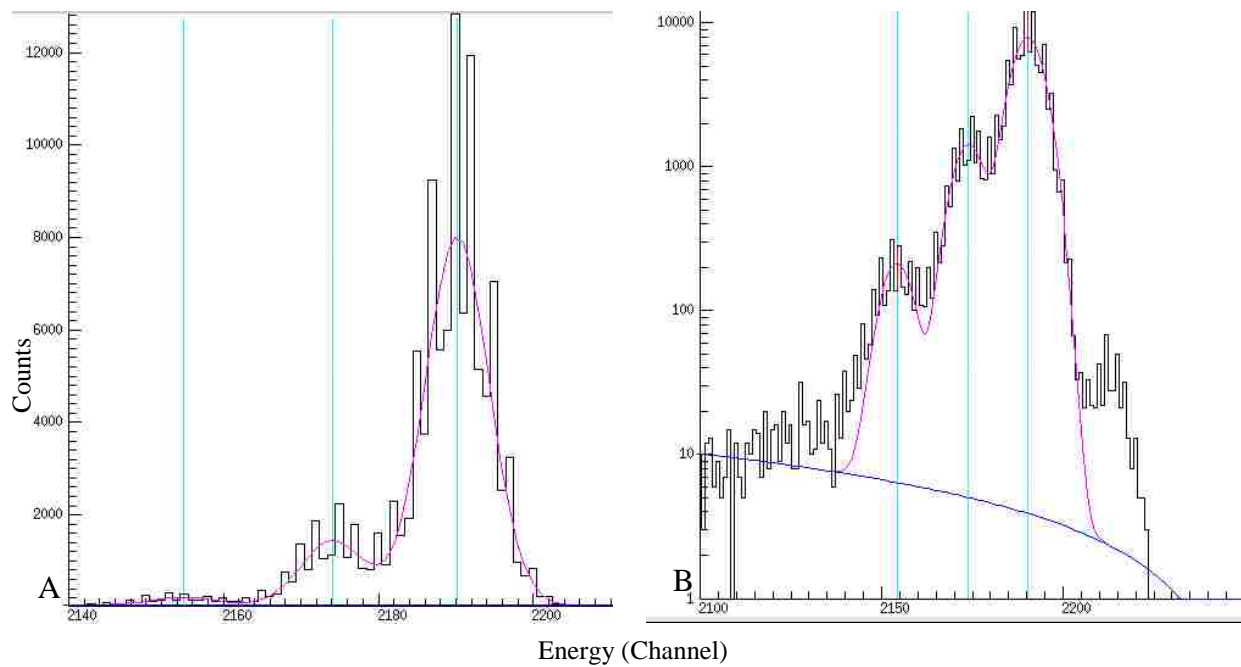
Figure 3-11   Energy spectrum from the first back segment of "Charm", with the three energy peaks fitted with a Gaussian fit plus background term. A linear scale graph is shown [A] besides the same graph in y log scale [B].

alpha lines in [241]Am (see Table 3-2) were nearly resolved in each strip. We fit each of the back side strips with a combination of 3 Gaussian peaks that were forced to have the same width. The energy resolution for the back segments is about 25 keV, about a factor of 2.5 improvement over using the front strips, illustrating the substantial benefit from using the back side signals to determine the full energy for events.

22

Table 3-2   Relevant alpha energies and branching ratios in [241]Am.

α Energy(keV)	Branching ratio (%)
5388	1.4
5442.9	12.8
5485.6	85.2

3.4 Offset Resistor Variability

An increase in the value for the offset resistors is expected to improve the energy resolution (linearity) from the front (resistive) side, but at the cost of decreased position resolution. This is better quantified in tests with a mask in front of the detector discussed later. Initial runs were taken with unmasked detectors and different values for the offset resistors. The energy response versus position was observed and showed increased nonlinearities with higher values of offset resistors (using alphas into the front side).

Due to the resistive coating built into the front side of the Super X3 detectors, the back side gives superior energy resolution. As a result, improving the energy resolution from the resistive strips is not *a priori* important. However, increasing the offset resistors has other important benefits, e.g. providing clearer definition of the ends of the strip and less dependence of the efficiency on energy and position. Testing was done with front side resistors of 50, 270, 470, 1,000, and 2,000 Ω. The energy resolution was determined through a Gaussian fit to the collected data using the three strongest alpha lines in [241]Am using the back strips. Figure 3-12 shows comparative results for 50, 470, 1,000, and 2,000 Ω and the results are reported in Table 3-3.

It is evident that energy resolution and the gain decrease on the back nonresistive signals as the offset resistance is increased. This required a decision of whether the preamplifier boards should be split: one resistance for the front and another for the back of the Super X3 detectors. The position resolution is best with 470 or 1,000 Ω offset resistors, but 50 Ω offset resistors would provide the best energy resolution from the back. However, it is strongly preferred to use a single value for the offset resistance in all channels so that a preamp motherboard can be used with any configuration of silicon strip detector.

3.5 Effective Length and Position Resolution

The detectors were mounted with masks in front of the detectors to restrict the position of the alpha particles to further study the effect of different offset resistors while checking the effective length and the position resolution. Detectors Charm and Strange were mounted with the front (resistive) side of the detectors facing the alpha source.
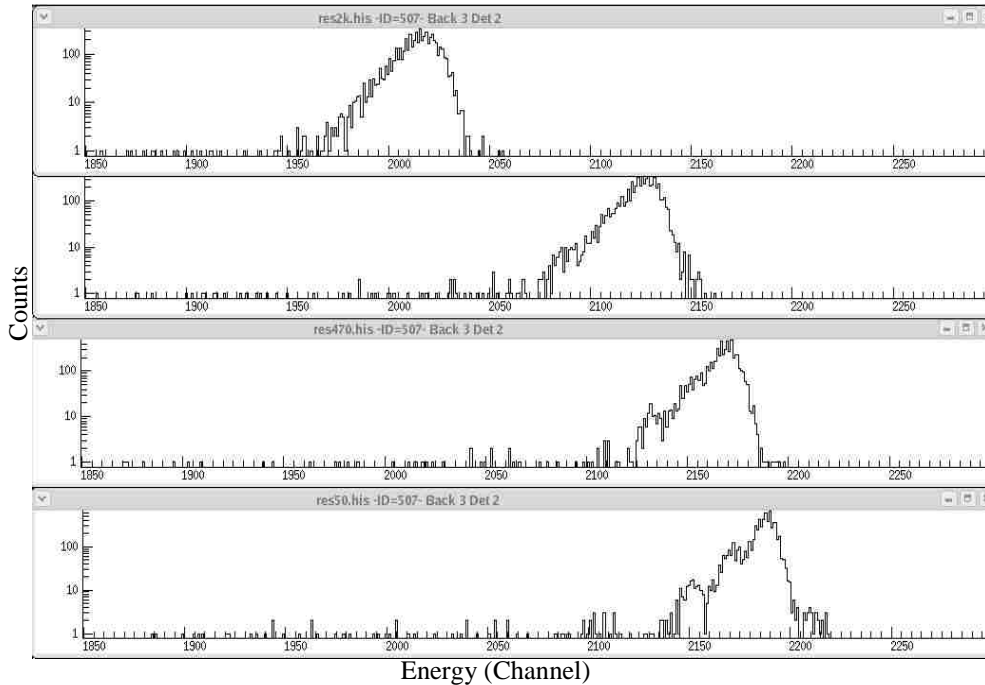
Figure 3-12   The four different offset resistances of 50, 470, 1,000, and 2,000 Ω, from bottom to top, shown through a detector's back strip. The drop in the gain as the resistance increases is apparent.

Table 3-3   The final results of the unmasked data with offset resistor variation.

Resistance (Ω)	Avg Resolution in keV		Avg FWHM in keV	
Ω	Charm (Front)	Strange (Front)	Charm (Back)	Strange (Back)
50	70.87	65.89	24.2	26.1
270	63.0	61.5	26.9	27.7
470	64.5	58.9	26.4	26.3
1,000	65.7	61.1	26.55	28.8
2,000	74.4	64.6	30.6	33.0

Data were collected with identical offset resistors for both front and back sides of the detectors using resistances of 50, 470, 1,000, and 2,000 Ω. Due to the fact that the detectors were masked, and the run was of short duration, only the main peak of the alpha source was fitted and subsequently compared.

The two masks (Mask 1 and 2) are shown in Figure 3-13. Mask 1 is a thin aluminum sheet with 7 slits of varying widths and distances apart from each other. Mask 2 is a thin U-shaped aluminum sheet with 6 strips of aluminum affixed midway on the U-shape, equally spaced. With Mask 2, the ends of the strips are illuminated,

24

Figure 3-13 Mask 1, showing varying slits and distances apart [A]. Mask 2, which does not cover the ends of the detectors and features five identical slit widths and spacing [B].

allowing simultaneous determination of the position calibration and the effective length of the strip. The specified active area of the silicon detectors has a length of 75 mm, but measurements with a ruler indicate the active length may be closer to 73 mm. The masks were mounted using stainless steel nuts at a distance of approximately 1.5mm from the front face of the detec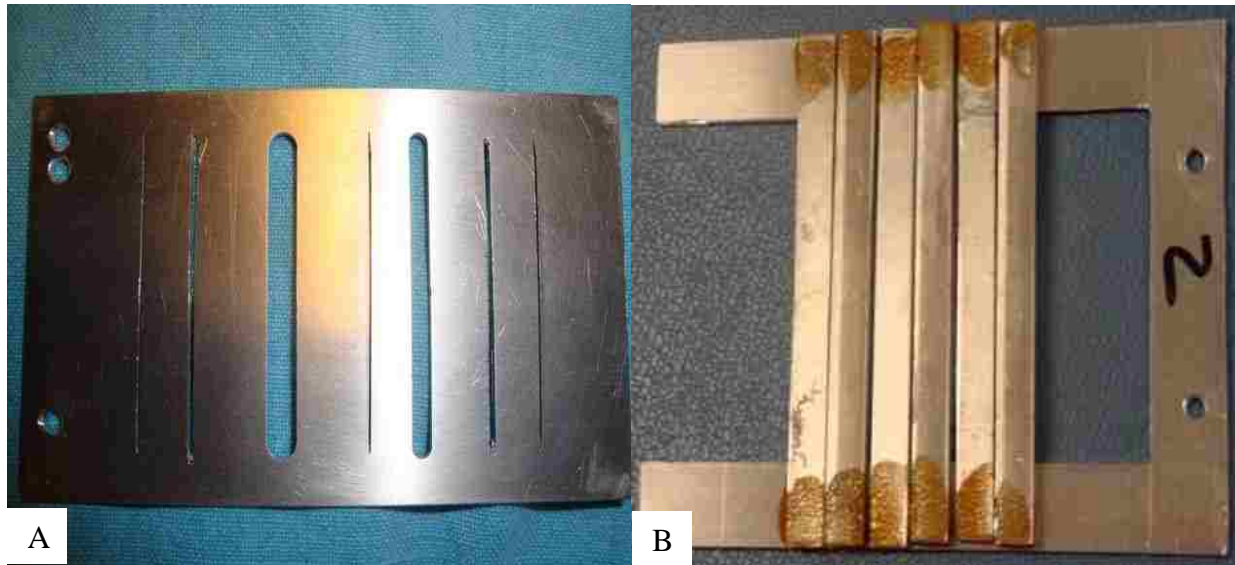tors. The detectors remained approximately 37 cm from the alpha source, so that parallax from the mask to the detectors should be small. Tests were performed with 150 volts applied to the detectors--sufficient for full depletion. As indicated in the calibration measurements described later, for alphas entering from the front, this is not necessarily an important requirement. Data were collected for 12 to 17 hours, depending on count rate.

Below is the data for each detector and analysis. For Mask 1, slits 1, 4, and 7 are 0.3 mm wide and slits 1 and 7 are located 66 mm apart. The centroid and the FWHM were found by fitting the peaks with a Gaussian fit, as shown in Figure 3-14. Slits 2 and 6 are 0.8 mm wide; the centroid and the FWHM were measured to check the resolution. For Mask 2, all the slits are 0.8 mm wide. This mask was produced so that the ends of the strip could also been illuminated while simultaneously accurately calibrating the position from the location of each slit, as seen in Figure 3-13. We identify the end of the strip by the channel located halfway up its leading edge. For each of the five peaks, the centroid and the FWHM were recorded. The distance between slit 1 and slit 5 for Mask 2 was 28 mm, as shown in Table 3-4.
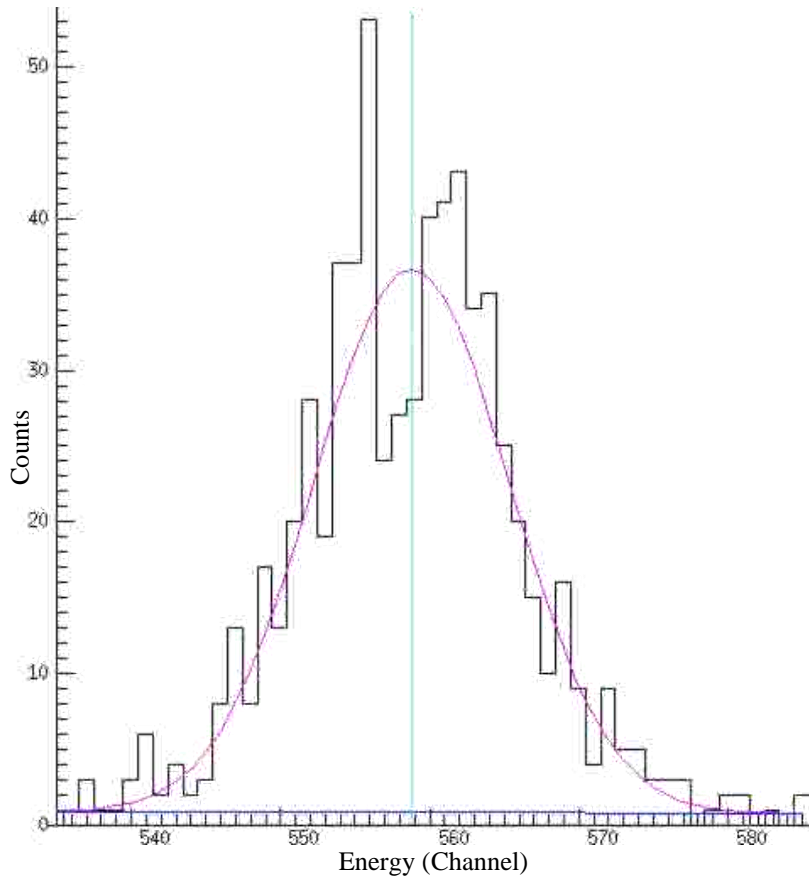
Figure 3-14 A screenshot of a Gaussian fit of peak 4. This indicates a centroid at channel 558.8 with a FWHM of 15.05 channels.

Table 3-4 A list of the slits of importance and their location on each mask.

Mask 1		Mask 2	
Slit	Location (mm)	Slit	Location (mm)
1	0	1	0
2	8.5	2	7
4	37.5	3	14
6	57.5	4	21
7	66	5	28

Plots showing the counts versus position and the energy versus position using 50 Ω offset resistances are shown in Figure 3-15. Since peaks 1, 4, and 7 are the same width, we can used these centroids and FWHM's to determine the resolution of the detector. Slits 1 and 7 are 66 mm apart, so calculating the difference between the channels of the centroids and dividing this by the distance apart we can obtain a chan/mm calibration.

$$\frac{[Centroid(7) - Centroid(1)]}{66\ mm} = \frac{(860.9 - 139.1)channel}{66\ mm} = 10.9\ channel/mm \tag{3-2}$$
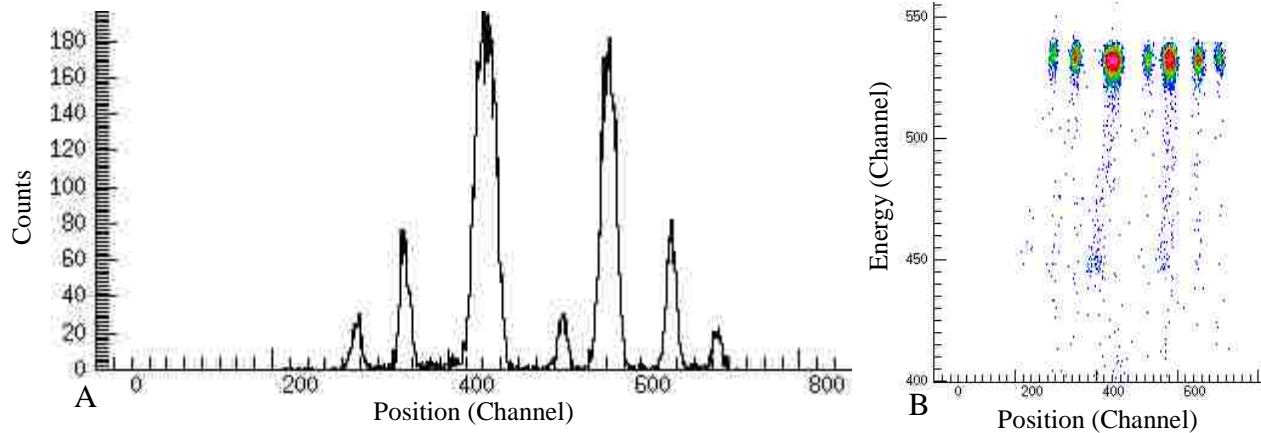
Figure 3-15 Counts versus channel is shown for a set of calibration data for Mask 1 [A]. Energy versus position is shown for the same data, same mask [B]. Peaks 1, 4, and 7 have the same widths, whereas peaks 2 and 6 are a similar but slightly larger width.

The resolution of this strip in the detector was found by taking the average of the FWHM's 1,4, and 7 then dividing by the channel/mm number calculated above.

$$\text{Resolution:} \quad \frac{Avg.FWHM}{\left(\frac{Channel}{mm}\right)} = \frac{15.33 \; channels}{10.9 \; channel/mm} = 1.4 \; mm \qquad (3\text{-}3)$$

Slits 2 and 6 are three times as wide as the slits 1, 4, and 7. If the resolution was dominated by the width of the slits, the FWHM would be 3/8 times smaller for slits 1, 4, and 7 than for slits 2 and 6. However, the measured FWHM of slits 2 and 6 was observed to be slightly larger (about 8%) than the narrower slits. Due to the slight difference in the FWHM when comparing slits of different widths, we are confident that the resolution for the 0.3 mm slit is dominated by the intrinsic resolution and not geometry. From this, it can be reasonably concluded that the FWHM measured for the 1, 4 and 7 slits is a fair representation of the resolution of the detector for 5.49 MeV alpha particles.

Mask 2 is the mask with the ends of the detector unshielded and five slits of identical width and distance apart. Since the widths of the slits in this mask are less than 1 mm, we can conclude from the measurements with Mask 1 above that the widths of the measured peaks from this mask should also provide a good test of the absolute position resolution of the detector. The graphs from this setup each represent a different strip on the front of detector Strange.

These tests were repeated using different values for the offset resistances in the preamplifier motherboards. Table 3-5 gives a summary of the data for the masked test on Detectors Charm and Strange. Using the known location of the five peaks, the channels/mm can be determined for each offset resistor. Using this result, the two

27

Table 3-5   Summary of the position resolutions and effective lengths for the masked tests.

Resistance (Ω)	Detector Charm (mm)			Detector Strange (mm)		
	Mask 1	Mask 2		Mask 1	Mask 2	
	Resolution	Resolution	Effective Length	Resolution	Resolution	Effective Length
50	1.4	1.4	68.8	1.4	1.4	69.5
270	1.4	1.5	70.4	1.5	1.4	70.8
470	1.5	1.5	70.5	1.5	1.5	71
1,000	1.9	1.7	71.3	1.7	1.6	71.25
2,000	1.9	1.9	70.8	1.9	2.1	71.25

values that mark the FWHM can be used to calculate the effective length. Each detector has data taken with each mask at each different resistance, 50, 470, 1,000, and 2,000 Ω.

Energy and energy versus angle plots using 50 and 470 Ω offset resistors are compared in Figure 3-16. It was clear that significant nonlinearities near the end of the strip are substantially improved using 470 Ω offset resistors. Since energy resolution on the front strips is not a primary concern, and since using a higher offset resistance also degrades the energy resolution on the back signals, (see Table 3-3) we chose to use a 50 Ω offset resistance to be used for all channels. This allows any channel on the preamplifier motherboard to be used for any detector type. However, it should be noted that nonlinearities in the position (and energies) are expected when using resistive strips (Super X3). It is interesting that changing the resistors on the front strips negatively impacts the energy resolution on the back (nonresistive) side, even though the series offset resistance on these channels was maintained at 50 Ω.

3.6 Voltage Bias

Detectors "Charm" and "Strange" were mounted with the back (ohmic or n-type) side of the detectors facing the alpha source to test the bias voltage required for full energy depletion. Since [241]Am's   5.485 MeV alphas penetrate only 25 μm into silicon [Kno00], the detectors have to be very close to fully depleted to produce a reliable signal for alphas entering from the back of the detector. A bias test was done taking short measurements at 100, 120, 140, 160, and 180 V for each detector.

Figure 3-16 shows energy versus position at different bias levels in separate colors. If the voltage is too low, then a reduction in the measured energy or efficiency at some positions on the detector will occur resulting from in complete charge collection in the surface region that is not depleted.
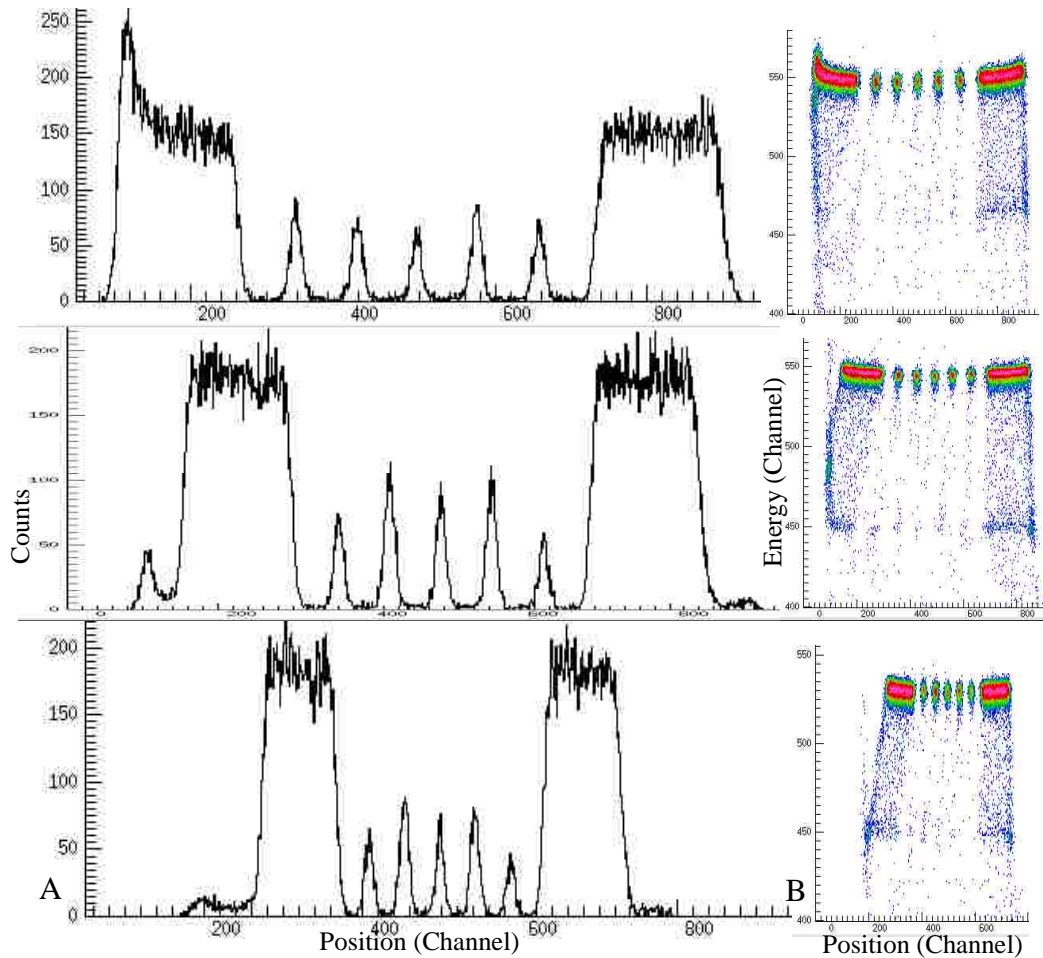
Figure 3-16 Counts versus position that is representative of the data collected with Mask 2 with 50 (top), 470 (middle), and 2,000 (bottom) Ω resistors [A]. A energy versus position graph for the same data [B].

Figure 3-16 shows energy versus position at different bias levels in separate colors. If the voltage is too low, then a reduction in the measured energy or efficiency at some positions on the detector will occur resulting from in complete charge collection in the surface region that is not depleted.

The manufacturer of the detectors, Micron Semiconductor, provides test data for each detector including capacitance versus voltage plots that indicate a depletion voltage for the detectors. Figure 3-17 shows such a plot for Detector 2792-12, aka "Charm". The C-V plot indicates a voltage bias of 100 volts is sufficient for depletion of this detector. However, the alpha test data shown in Figure 3-18 indicates that 100 volts is not sufficient bias to fully deplete the detector, and that a voltage closer to 140 V is required. Below is Table 3-6 of a sample centroid for detector Charm's calibrated front strip, compared to detector Strange's calibration front strip. This is followed by Table 3-7 which does the same comparison, but this time with a calibration back strip from each detector. From

Figure 3-17   Manufacturers' documentation for detector "Charm".

Figure 3-18 Voltages of 100 (black), 120 (magenta), 140 (blue), and 160 (green) for Detector "Charm", depicting the sum of the left and right signals.
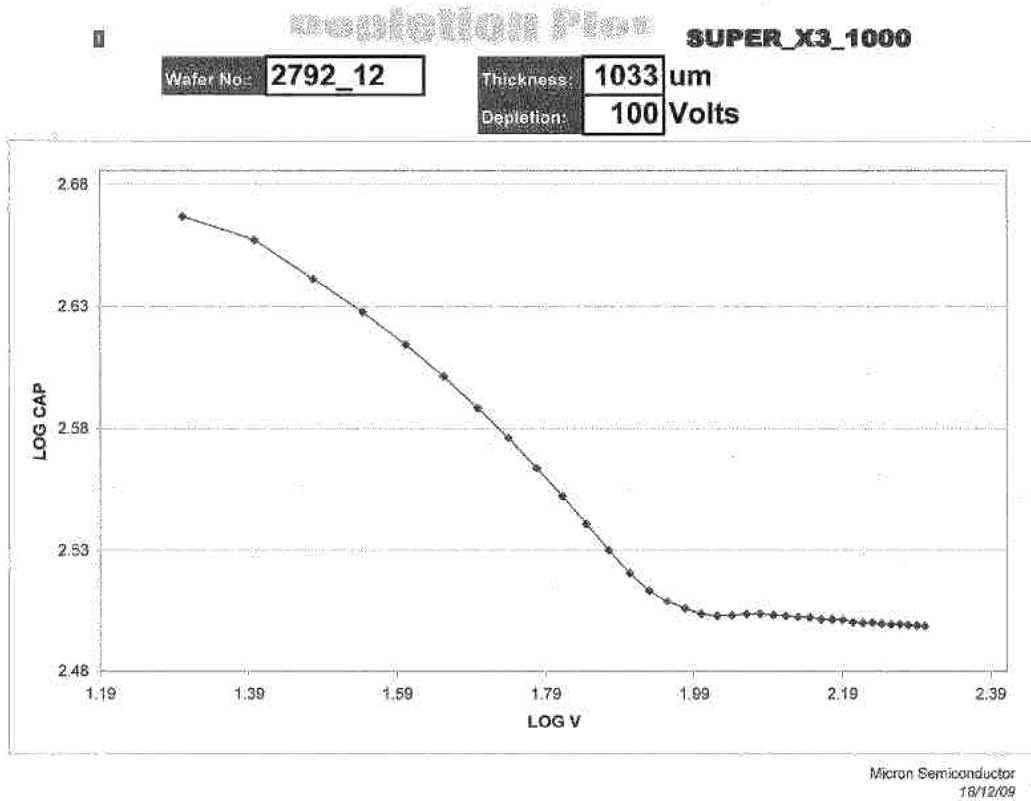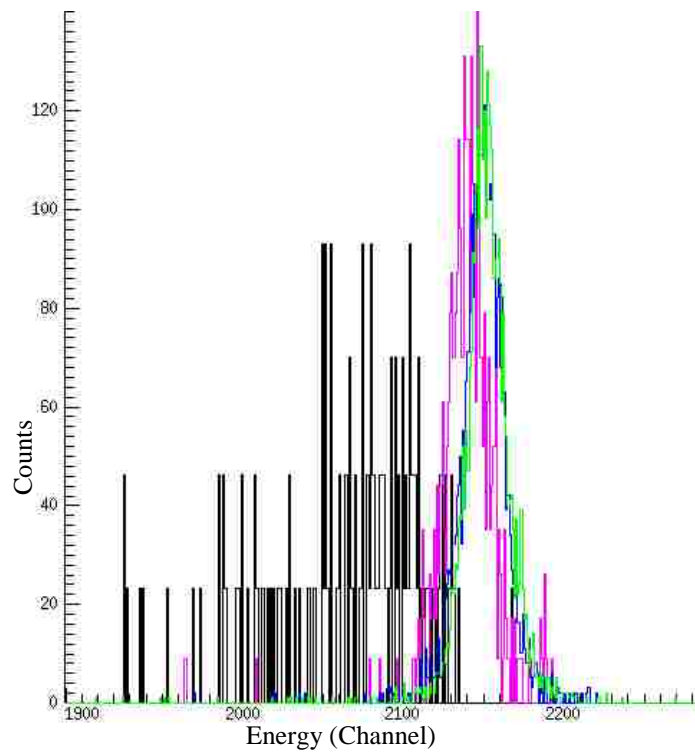
Table 3-6   The end results of the voltage bias test, front side.

Voltage Bias	Detector Charm Graph Front				Detector Strange Graph Front			
	Centroid	FWHM	FWHM (keV)	Counts/min	Centroid	FWHM	FWHM (keV)	Counts/min
100	2096.5	77.2	201.9	2	2101.2	78.6	205.3	2
120	2149.8	25.4	64.8	10	2149.8	27.3	69.8	13
140	2160.4	28.0	71.2	43	2155.8	28.1	71.4	51
160	2162.6	27.5	69.8	93	2158.1	26.1	66.4	93
180	2165.1	27.9	70.6	115	2159.6	27.0	68.7	111
200	2166.1	28.5	72.2	114	2161.1	26.8	68.1	109

Table 3-7   The end results of the voltage bias test, back side.

Voltage Bias	Detector Charm Graph Back				Detector Strange Graph Back			
	Centroid	FWHM	FWHM (keV)	Counts/min	Centroid	FWHM	FWHM (keV)	Counts/min
100	2003.1	67.7	185.3	2	2030.7	70.0	189.1	3
120	2122.3	16.8	43.5	9	2144.3	19.6	50.2	8
140	2152	12.3	31.5	41	2159.7	13.7	34.8	37
160	2156.3	12.8	32.5	83	2164.8	12.1	30.6	79
180	2157.9	12.8	32.5	92	2166.6	12.0	30.4	101
200	2158.8	12.5	31.7	96	2166.8	12.5	31.7	100

studying the change in the FWHM, the shift of the centroid, and the counts/min for each observed bias, we determined the recommended bias voltage for the other Super X3 ANASEN detectors.

3.7 Summary

In this section the results from tests at LSU using a ^{241}Am alpha source to study the performance of the first two Super X3 Detectors "Charm" and "Strange" are reported. Tests were performed in three separate configurations. First, the detectors were mounted with the front (resistive) side facing the source. Gains were matched and the linearity of the energy response with position was tested using different values for the "offset" resistors in the preamp motherboard that are in series with the inputs from the front (resistive) strips. In the second series of tests, we flipped the detectors again so that the front side was facing the ^{241}Am alpha source and placed aluminum masks between the detectors and the source. In this configuration, we calibrated and studied the position resolution of the detectors, as well as measured the effective length of the strips. In the third series of tests, the detectors were mounted with the rear (ohmic) side facing the source to study the response of the detectors as a function of bias voltage. The same tests were performed with other ANASEN detectors as well, with similar results.

The depletion plots provided with the detectors indicate full depletion to be 100 and 90 volts for detectors Charm and Strange, respectively. However, our bias tests show an increase in the measured signal size with voltages up to about 140 V for alphas impinging on the rear (ohmic) face. A significant increase in efficiency was also observed between 140 V and 160 V, though there was little change in the measured energy response in this range. We find in general that about 50% over bias is required relative to the manufacturer's specification to achieve full depletion. However, given about a 25V drop in voltage in the 10 MΩ preamp resistor (for typical 2.5 μA leakage current around this voltage), this corresponds to about 25-35% over bias as compared to the Micron specifications, which is comparable to previous experience.

By summing the measured energy signals from the two ends of the front strips, an energy resolution (combining all positions) was found to be between 60-75 keV for all resistive strips on both detectors. A significant part of this resolution was observed to be due to nonlinearity with position (especially for low values of the offset resistance). When gating on only a narrow range of positions, the energy resolution from the front face was found to be about 30% improved (to less than 50 keV on all strips).

An important new feature implemented in the Super X3 design is the segmented, non-resistive, ohmic (back) face that provides improved resolution, as well as a built-in means for calibrating position on the resistive face. The energy resolution from the back face was found to be between 24 and 33 keV for the back segments in all tests.

Analysis of the data also informed our decision regarding the selection of the series "offset" resistance to be included in the preamplifier mother boards. These offset resistors are surface-mounted components in the new 72-channel preamplifier unit under development and are not easily modified. An increased value in the offset resistance degrades the position resolution from the front strips. As for counterarguments, higher values for the offset resistance reduces nonlinearities, produces clearer definition of the ends of the strips, and mitigates problems arising when the signal is low and similar in strength to noise. The position resolution was found to be approximately 1.4 mm, even when using the smallest values for the offset resistance. Position resolution is the most important factor for the front signals, while energy resolution is the most important factor for the nonresistive channels. The LSU 72-channel preamplifier motherboards will be used in a variety of configurations, and 50 Ω offset resistors were chosen for all channels to achieve the best overall position and energy resolution. We must be aware, however, that some nonlinearities are expected in position determinations for events occurring near the end of the resistive strips.

CHAPTER 4. HEAVY ION RECOIL CHAMBER

The reactions of interest for astrophysics with radioactive ion beams generally involve bombarding a light target with a heavy incident nucleus. In these cases the heavy reaction products typically are emitted at small laboratory angles with energies per nucleon similar to that of the incident beam due to the high kinematic compression from the center-of-mass to laboratory frame. A heavy ion detector capable of Z identification and fast counting rates can be particularly powerful for selecting the reaction channel of interest, particularly as radioactive ion beams are often contaminated with other isotopes than the one of interest. We have developed a gas ionization detector for heavy ion detection with ANASEN. The detector is housed in a NW250 chamber mounted downstream from the ANASEN chamber around $\theta_{lab}=0°$.

Particles enter the chamber through a 6.4 cm diameter 2 mg/cm^2 mylar window backed with a supporting wire mesh, and there is a 10 mm dead zone of gas before the first plane. The first version of the counter used in the experiments described here used 20 copper planes with 1 mm spaced wire grids. The grids themselves are attached to thin copper 14 cm wide squares with a 8.9 cm diameter window machined out of the center. The wires are 20 μm thick gold-plated tantalum wires spaced 1 mm apart and affixed to each size of the grid's window with silver conductive double-compound epoxy. Each corner of the square has a hole where the grid is slid on the four support rods mounted to the back flange. Grids are shown in Figure 4-1 B.

We designed, shown in Figure 4-2, and constructed a custom adapter between the experimental chamber and the heavy ion recoil chamber. This transition piece has a disc that can be inserted at $\theta_{lab}=0°$ to block the incident primary beam. Alternatively an aperture is mounted on a different feedthrough that can be inserted to collimate the beam entering the HIRC for tuning purposes. The laterally moveable 11 mm diameter beam blocker is a metal disk soldered to a wire suspended between the top of a U-shaped aluminum piece. The laterally moveable tuning aperture is a thin aluminum sheet with an 8 mm diameter hole bored in the center. The tuning aperture was chemically coated so that the hole would be seen as a black circle on the camera used to help tune the beam. The beam blocker and the tuning aperture can be placed together to fully block the window of the heavy ion recoil chamber. The thick beam blocker is used to prevent the direct beam going into the chamber to cut down on the counts that are not useful to the experimental measurement.
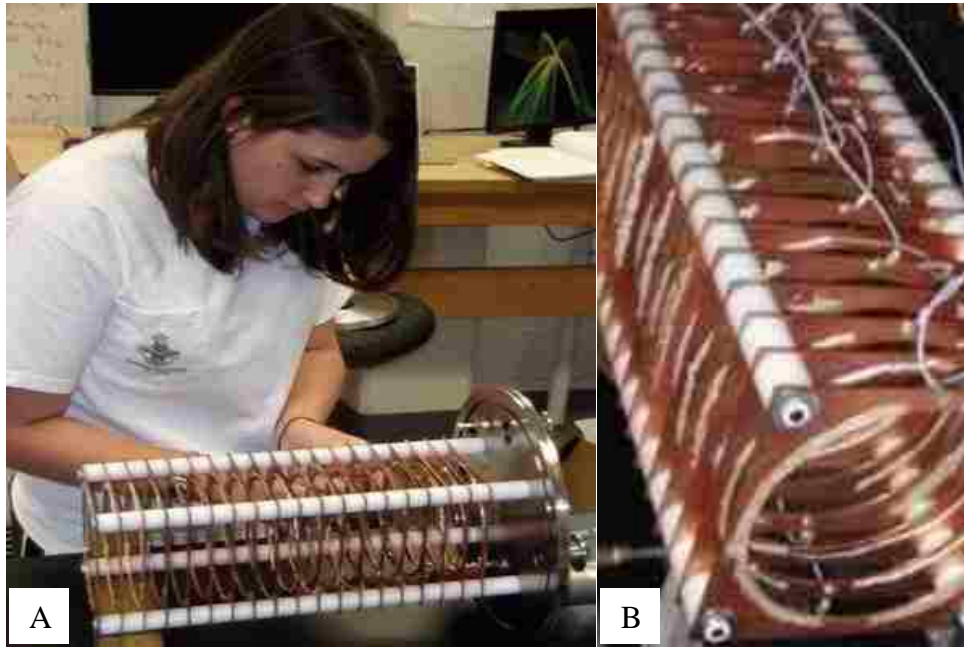
Figure 4-1 LSU undergraduate student, Hannah Gardiner is wiring up cathodes and anodes [A]. A close-up photo of the interior wire grids and electronics housed within the HIRC [B].
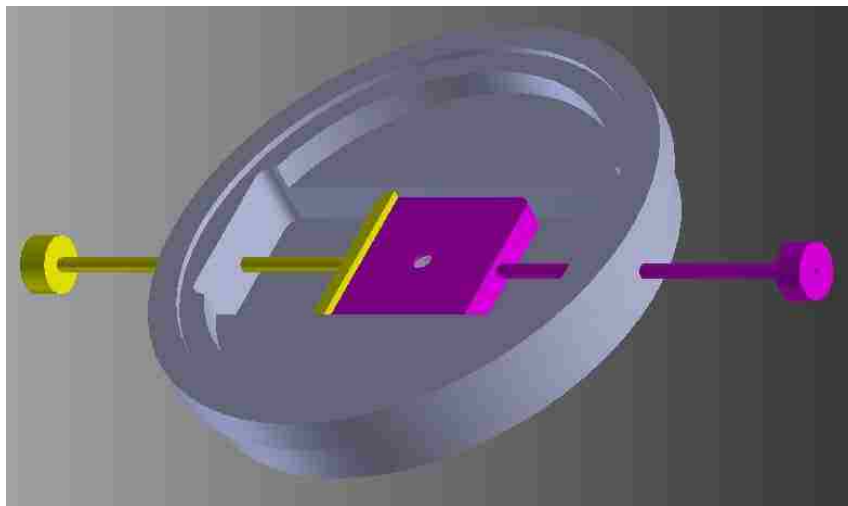
Figure 4-2 An Inventor picture of the adaptive flange for the HIRC with the hole and blocker arms shown in purple and yellow, respectively.

The above described heavy ion chamber was used in the FSU's RESOLUT beam experiments during the summer of 2011. The HIRC was used with a simple arrangement of silicon strip detectors with the ANASEN electronics in a first series of experiments. In the next sections, we will describe two of the first experiments of ANASEN.

CHAPTER 5. MOTIVATION FOR STUDYING ^{18}NE

The structure of ^{18}Ne is important for understanding the rate of the ^{14}O(α,p)^{17}F reaction and X-ray bursts. Energy generation in Type-I X-ray bursts begins slowly with hydrogen burning at lower temperatures by the CNO and hot CNO cycles. Temperatures increase as energy is generated from burning of the nuclear fuel but there is no associated expansion due to the degenerate nature of the system, and the thermonuclear runaway takes off when temperatures reach a sufficient level to ignite the helium burning via the triple-α and α-p processes. The rates of alpha induced reactions are typically much less than for hydrogen induced reactions due to the larger Coulomb barriers, and the (α,p) reactions in the α-p process generally control the rate of energy generation in the explosion. Sensitivity studies have shown that the shape of the light curve and isotopes produced are quite sensitive to the rates of the helium burning reactions, and the first (α,p) reaction in the α-p process is the ^{14}O(α,p)^{17}F reaction [Par08].

The rate of the ^{14}O(α,p)^{17}F reaction is quite uncertain. The most probable energy range (the Gamow window) for (α,p) reactions at temperatures of interest for X-ray burst explosions lies at relatively high center-of-mass energies owing to the Coulomb barrier between helium and the nuclei of interest. At the highest temperatures, the cross sections are typically dominated by many resonances and statistical models of nuclear reactions can provide a fairly reliable estimate of the astrophysical reaction rate. However, the nuclear level density is lower at smaller center of mass energies, and the properties of a small number of isolated resonances can dominate the astrophysical reaction rate at lower temperatures of interest. In such cases, the reliability of statistical models for the reaction rate is questionable. The situation is exacerbated in lighter nuclei, where the Gamow window is lower in energy and the nuclear level density is smaller. In particular, the level density of ^{18}Ne is quite low in the energy regime of interest (excitation energies from about 5.5 to 6.6 MeV) for the ^{14}O(α,p)^{17}F reaction, and it is likely that a single state in the compound nucleus dominates the reaction rate over a broad range of temperatures.

There have been a number of previous studies of ^{18}Ne due in large part to its importance for X-ray bursts. The level structure is summarized in Figure 5-1, and known states between the proton threshold (3.922 MeV) and E_x~7 MeV are summarized in the Table 5-1. Much of the level structure of ^{18}Ne was first established through studies of the (^{3}He,n) and (p,t) transfer reactions [e.g. see Hah96, Til02]. Excitation energies, spin-parities and assignments with analog levels in the mirror nucleus ^{18}O are all well established for states below 6.0 MeV. However, it is the properties of states above 6 MeV that dominate the ^{14}O(α,p)^{17}F reaction rate. We report here on a high statistics
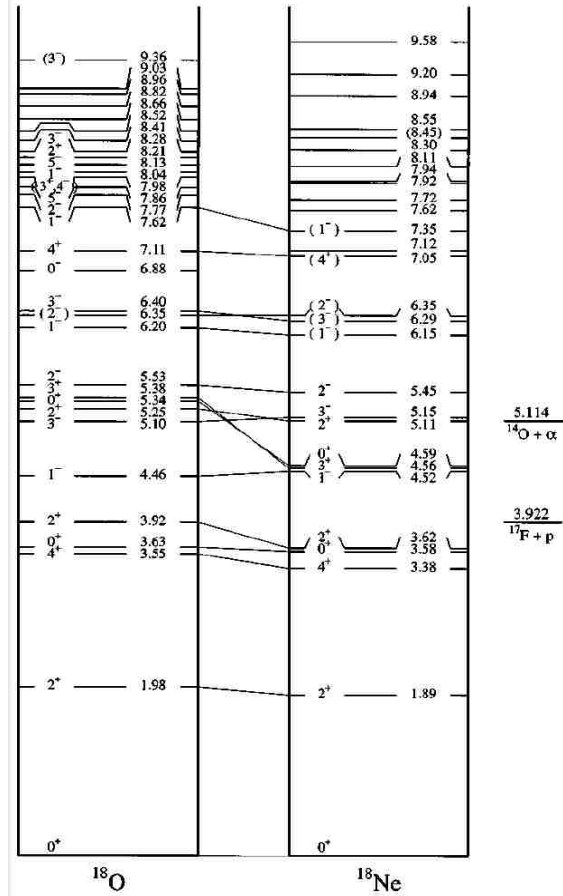
Figure 5-1 Excitation energies (MeV) for ^{18}Ne and the stable isobar ^{18}O. Reprinted from Reference [Hah96].

Table 5-1 A survey of previous literature on energy levels in ^{18}Ne between E_x = 4-7 MeV.

0	J	Wave	Γ_p (keV)	Reference	Note
4.519(4)	1$^-$	P	9 (6)	[Par05]	Γ_p ~ 0.16 keV[a]
4.520(7)				[Hah96]	
4.524(3)	3$^+$	S	18 (2)	[Bar99, Gom01]	
4.527(4)			17 (4)	[Par05]	
4.589(7)	0$^+$	D	4 (4)	[Hah96]	Γ_p ~ 0.08 keV[a]
			2 (6)	[Par99]	
5.106(8)	2$^+$	S	47 (6)	[Hah96]	
			45 (7)	[Par99]	
			42 (4)	[Jun10]	
5.153(8)	3$^-$	P	< 15	[Hah96]	Γ_p ~ 3 keV[a]
			8 (5)	[Par99]	
5.454(8)	2$^-$	P	< 20	[Hah96]	Γ_p < 6 keV[a]
5.467(5)			6 (6)	[Par99]	
6.134(1)	(1$^-$)	P	38 (2)	[Bla03, Bar12]	$\Gamma_{p'}$ = 16 (1) keV
6.150(10)			< 40	[Hah96]	
6.293(10)	(3$^-$)	P	< 20	[Hah96]	
6.305(4)			8 (7)	[Par99]	
6.345(10)	(2$^-$)	P	45 (10)	[Hah96]	
6.358(5)			18 (9)	[Par99]	

[*]Expected width based upon properties of mirror state in ^{18}O.

measurement of ^{17}F+p elastic scattering to improve our understanding of the most important states for the ^{14}O(α,p)^{17}F reaction rate. While only states above the alpha threshold at 5.1 MeV can contribute to the ^{14}O(α,p)^{17}F reaction rate, any states above the proton threshold at 3.9 MeV can influence the proton scattering cross section and may be important for interpreting data from an elastic scattering measurement. Hence, we briefly summarize the present understanding of the ^{18}Ne level structure above the proton threshold.

The 4.52 and 4.59 MeV states are strongly populated in the ^{16}O(^{3}He,n)^{18}N reaction and have been established to be analog states to the 4.46 (1$^-$) and 5.34 MeV (0$^+$) states in ^{18}O, respectively [Til02, Par99, Gar91, Hah96]. These states both have a very narrow width and will not significantly influence the ^{14}O(α,p)^{17}F or ^{17}F+p scattering cross sections in the energy range of interest.

The first 3$^+$ level in ^{18}Ne was long-sought due to its importance for the ^{17}F(p,γ)^{18}Ne reaction rate. It remained elusive until the development of radioactive ion beams that allowed its properties [E_x=4.524 (3) and Γ_p=18 (3) keV] to be accurately determined through a measurement of ^{17}F+p elastic scattering [Bar99,Bar00]. The properties of this state were confirmed by [Gom01] and [Par05]. While this state is below the alpha threshold in ^{18}Ne and has no influence on the ^{14}O(α,p) reaction rate, it presents a broad s-wave resonance in elastic scattering that could influence the energy range of interest in ^{17}F+p scattering through interference with higher lying levels.

The 5.11 MeV (2$^+$) state is also a broad s-wave resonance and could significantly influence the ^{17}F+p scattering cross section. The width of this natural-parity state has been established primarily through high-resolution (p,t) transfer reaction measurements [Par99, Hah96] and recently through a measurement of ^{17}F+p elastic scattering [Jun10], with results all in good agreement. Both the 4.52 (3$^+$) and 5.11 (2$^+$) MeV states lie below the energy region covered in our current measurement, but we include these levels in our analysis with values fixed to previous measurements.

The 5.15 and 5.45 MeV states have been established to be analogs of the 5.10 (3$^-$) and 5.53 (2$^-$) MeV states in ^{18}O, respectively. Direct measurements of the widths of these states, through (p,t) transfer reactions, have large uncertainties essentially consistent with upper limits of about 10 keV. Spectroscopic information from the states in the mirror nucleus ^{18}O predict that these levels should have smaller proton widths. These levels are expected to have a very small influence on the ^{17}F+p elastic scattering cross section in the region of interest but are discussed in more detail in Section 8.

While previous experiments have made improvements in our understanding of the $^{14}O(\alpha,p)^{17}F$ reaction rate, substantial uncertainties remain at lower temperatures arising primarily from the uncertain contributions of 3 resonances corresponding to states in ^{18}Ne at 6.13, 6.30, and 6.36 MeV [Bla03, Bar12, Hah96, Par99]. It seems clear that these 3 states are mirrors to the 6.20 (1$^-$), 6.35 (2$^-$) and 6.40 (3$^-$) MeV states in ^{18}O that were strongly populated in the $^{17}O(d,p)^{18}O$ reaction with p-wave neutron transfer [Li76]. However, it must be recognized that the mirror assignments between these 3 levels, and the spin-parity assignments of the 3 states in ^{18}Ne are tentative.

The 6.13 MeV state has been observed in the $^{16}O(^3He,n)^{18}Ne$ reaction [Hah96, Alm12] and in $^{17}F(p,p')^{17}F$ inelastic scattering [Bla03, Bar12]. The energy of the resonance E_x=6.134 (1) keV and total width Γ=54 (3) keV have been accurately determined by the $^{17}F(p,p')^{17}F$ inelastic scattering cross section[Bar12]. The inelastic scattering cross section also indicates a branching ratio to the first-excited state in ^{18}Ne of 30% or 70%, while a branching ratio measurement from $^{16}O(^3He,n)^{18}Ne^*(p)$ favors a branching ratio of <21% to the first-excited state [Hah96]. However, these results are consistent with either a 1$^-$ or 2$^-$ assignment for the state. The state is intensely populated in the $^{16}O(^3He,n)^{18}Ne$ reaction. The angular distribution is somewhat forward-focused, and Coulomb level shift calculations indicate a preference for this state to be a mirror to the 6.20 MeV (1$^-$) state in ^{18}Ne [Hah96]. On the other hand, the 6.13 MeV state is extremely weakly populated in the $^{20}Ne(p,t)^{18}Ne$ reaction. The state was also observed in a measurement of $^{17}F+p$ elastic scattering [Gom00]. The data from this measurement are shown in Figure 5-2 along with an R-matrix analysis by He *et al.* [He10a] that demonstrates that the shape of structure observed in elastic scattering is not consistent with a 1$^-$ assignment, and a 2$^-$ assignment is preferred. The spin assignment for this level is thus far from conclusive. Firmly establishing this assignment is important as an unnatural parity 2$^-$ state can not be populated in the $^{14}O+\alpha$ channel and will not contribute to the $^{14}O(\alpha,p)^{17}F$ reaction rate, while a 1$^-$ state could dominate the reaction rate at low temperatures.

Information on the other two states of interest at 6.30 and 6.36 MeV comes primarily from the $^{20}Ne(p,t)^{18}Ne$ reaction [Hah96, Par99]. Both states are populated in the (p,t) reaction, and excitation energies are accurately determined. However, no significant information on the spin assignments for the two states exists, and there are discrepancies regarding the widths that come only from line width measurements in the (p,t) reaction. A strong single resonance has been observed in the $^{16}O(^3He,n)^{18}Ne$ reaction near this energy, but no ($^3He,n$) measurement has had sufficient resolution to resolve the two separate states that have been seen in the (p,t) reaction. We performed a
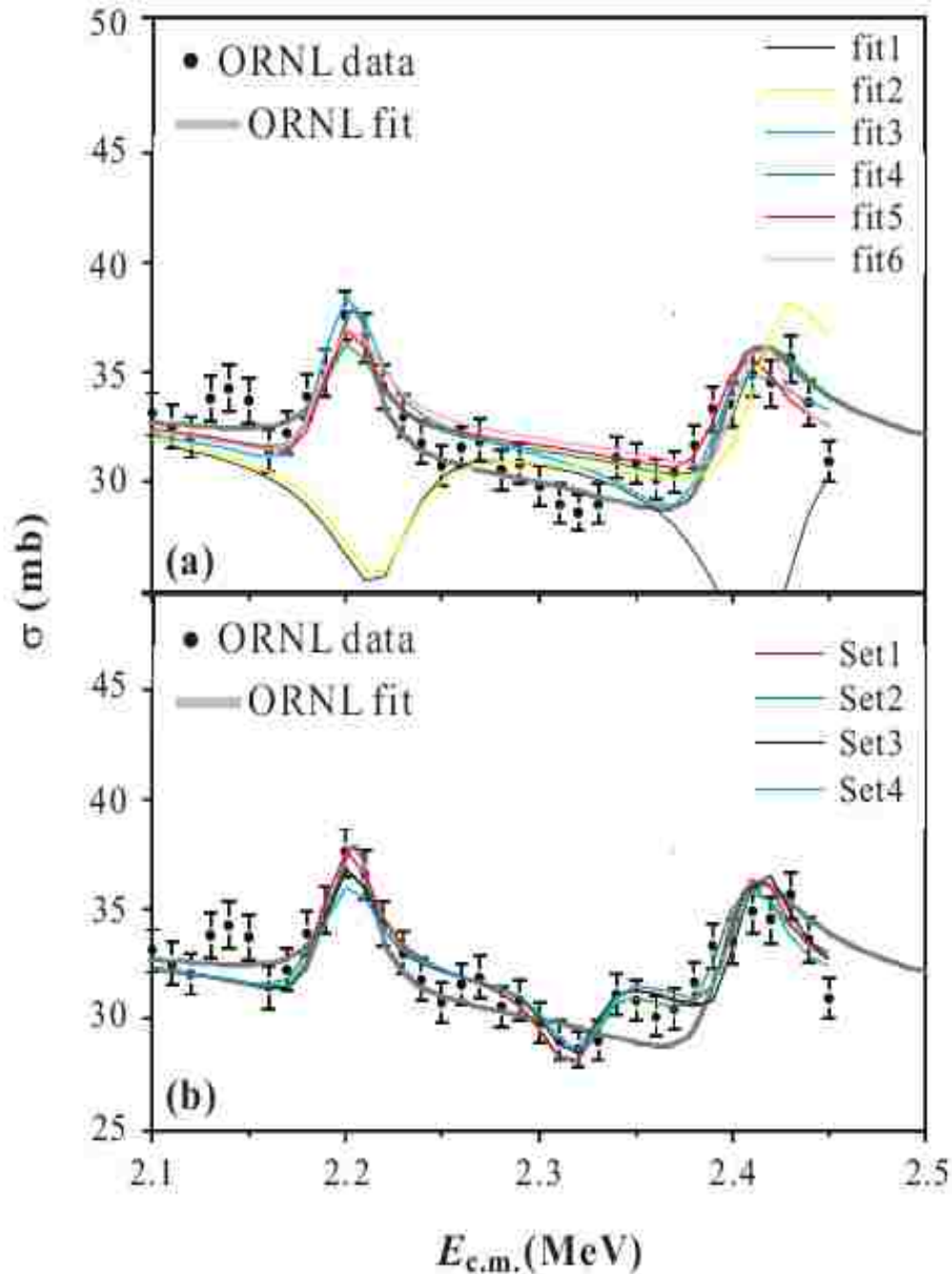
Figure 5-2 Excitation function for the $^{17}F(p,p)^{17}F$ reaction from [Gom00] is shown along with R-matrix analysis by [He10a]. The smooth curves are R-matrix fits to the data with varying assumptions regarding the properties of states in the region. Calculations that reproduce the resonant structure at $E_{cm} \cong 2.2$ MeV ($E_x = 6.13$ MeV) require either a 2- or 3- assignment for the resonance, with a 1- resonance instead producing a minimum (Fit 1 and 2 from the top panel). Figure reproduced from [He10a].

high statistics $^{17}F+p$ elastic scattering measurement in the region of $E_x\sim6-7$ MeV, as well as studying $^{17}F(p,\alpha)^{14}O$ over this energy range, to improve our understanding of the contribution of these low energy resonances to the reaction rate.

CHAPTER 6. ^{17}O TEST EXPERIMENT

During the summer of 2011, a commissioning experiment with a partial implementation of ANASEN was performed at Florida State University's RESOLUT facility in preparation for the ^{17}F+p elastic scattering measurement. A beam of stable ^{17}O was produced from the combination of the tandem and linear accelerators and bombarded polypropylene (CH$_2$) targets. The target ladder had four positions, one that was reserved for a collimator used to help focus the beam. The experimental setup included thick and thin targets of 2.0 and 0.28 mg/cm^2 polypropylene, respectively. An ^{17}O beam with a current occasionally measured at the faraday cup closest to the experimental chamber was used to bombard both thin and thick CH$_2$ targets.

The emitted light particles (protons and alphas) were detected by a telescope of silicon strip detectors consisting of 2 layers, 500 and 1000 μm thick, of Micron Semiconductors Design S2 silicon strip detectors [Mic14]. The front (p-junction) has 48 rings (0.5 mm width) and back (n-junction) has 16 segments with inner and outer radii of 10 and 38 mm, respectively. The second silicon detector was 1.3 cm behind the first. The rings of the ΔE detector and the segments of the E silicon detector faced the target ladder. The front detector was positioned 4.2 cm from the target to subtend, $10.7°<\Theta_{lab}<39.7°$, for the ^{17}O experiment. An energy calibration of the detectors was performed before and after the experiment by increasing the separation between the detectors and inserting a ^{228}Th source between the 2 layers.

The heavy recoil particles were detected by the HIRC (see Figure 2-4). The target ladder was located 20.3 cm upstream from the 1 cm diameter beam blocker, and 25.7 cm from the 6.4 cm diameter window of the heavy ion recoil chamber, so that the HIRC accepts $1.3°<\Theta_{lab}<8.5°$. Figure 6-1 depicts a schematic of the experimental setup including the beam, target, silicon detectors and HIRC. A photograph of inside the scattering chamber is shown in Figure 6-2.

Signals from the silicon detectors were processed using the ANASEN electronics. The silicon telescope signals were first sent through the LSU 72 channel preamplifier system, and then into the ASICs system. The anode signals from the heavy ion recoil chamber were processed using individual Canberra pre-amplifier boxes and then out through NIM ORTEC 572 shaping amplifiers and conventional VME peak sensing ADC's. This was the first experiment for ASICs and for the heavy ion recoil detector.
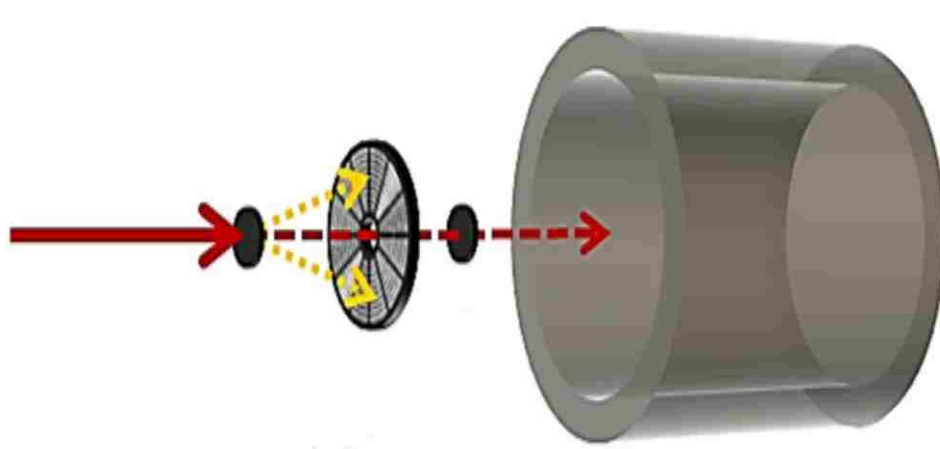
Figure 6-1 A cartoon schematic of the experimental setup, featuring the beam, target, silicon telescope, beam stopper, and heavy ion recoil chamber.

Figure 6-2 Photograph of the inside of the scattering chamber, where the target ladder and silicon telescope were mounted.

6.1 Data and Analysis

We ran a six day test experiment of $^{17}O(p,\alpha)^{14}N$ for calibration and to test the system using a 55 MeV ^{17}O beam. Since this was the first utilization of the heavy ion recoil chamber in an experimental setup, the efficiency had to be measured. The efficiency was determined by how many times oxygen was detected in the ion chamber in conjunction with a proton in the silicon detectors, divided by the total number of protons detected by the silicon detectors. Figure 6-3 shows a plot of measured energy versus laboratory angle (radians). The alphas and the protons in the silicon ΔE versus E plot are clearly distinguished.
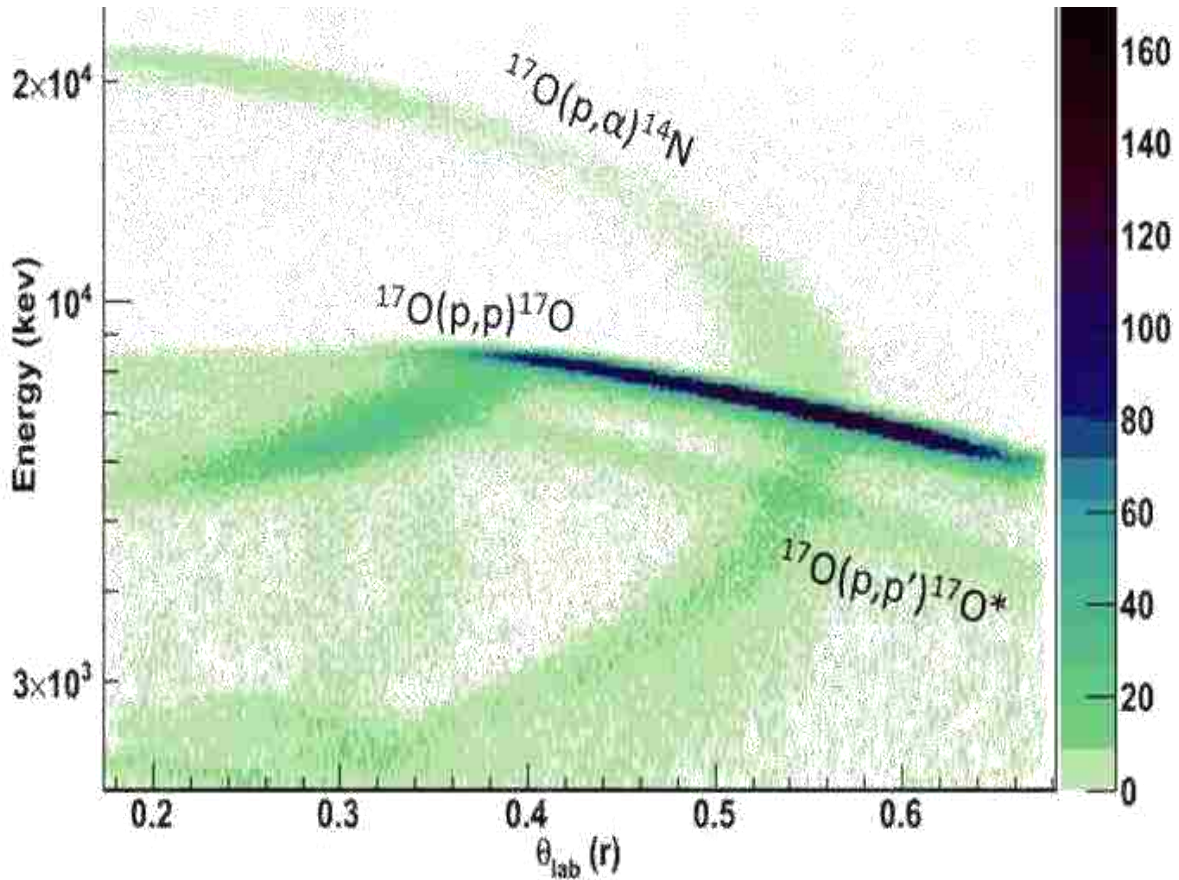
41

Figure 6-3 Total energy (keV) of the second silicon detector versus Θ_{lab} (radians) showing the p's and α's detected by the S2 silicon telescope.

To determine the HIRC efficiency, we select the angles where elastically scattered protons can be unambiguously identified by kinematics alone. We divided the protons into segments according to angle ranges to get the angle dependent efficiency for the HIRC. A similar process was used with the alphas ignoring the area where protons and alphas overlap. The calculations for the efficiency were performed with alphas and protons in regions where only one or the other was present. The efficiencies were determined as a function of angle using the measured yields.

During this experiment we figured out the efficiency of the heavy ion recoil chamber and the resolution of the experimental system as a whole. In the Figure 6-4, we plot the proton energy in keV versus the Segment ID for the S2 energy detector. From this it can be seen that the beam was not centered as the maximum proton energy should be the same for all segments. To compensate, we add a beam offset in the data analysis program. Once the beam was corrected for the offset, the energy versus θ_{lab} of the S2 silicon telescope shown in Figure 6-3 showed a clear separation of the elastic and inelastic scattering.
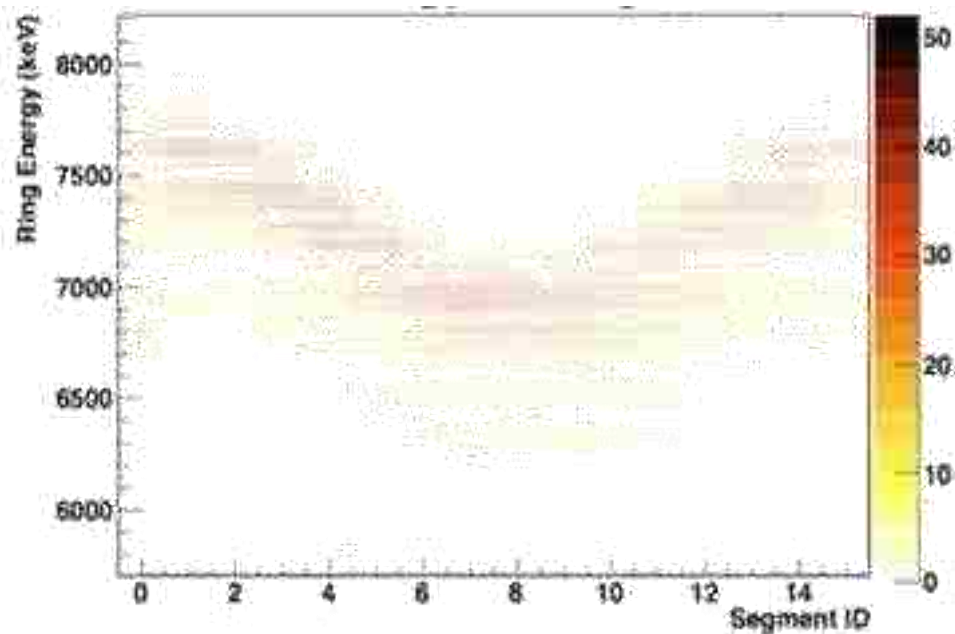
Figure 6-4 Proton Energy in keV versus Segment ID for S2 detector.

The ^{17}O experiment also showed a 70 to 92% efficiency. At forward angles the efficiency is reduced because the heavy ions are lost due to the blocker. The efficiency was also studied independently in measurements with a ^{17}F beam and is discussed in more detail in Chapter 7. This efficiency is within the expected range, but shows that there is still some improvement to be made with this detector.

Figure 6-5 shows a plot of the energy loss in the first 3 anodes versus total energy from the HIRC. Clear separation of oxygen and nitrogen is achieved when the ions deposit their full energy into the gas. Some events are observed with lower total energy than expected. The regular pattern in total energy indicates that these events arise from ions that collide with a wire in the one of the planes of ionization chamber and do not deposit their full energy in the gas. The intensity of each of these groups is about 2% of the total intensity and is consistent with the transmission expected through the wire planes. This result in some ambiguities. This can be mitigated by running at higher gas pressures (to reduce the number of wire planes effectively used). We have also worked on a redesign of the counter to increase the wire spacing as discussed in Chapter 9.

The collaboration agreed that these lines were caused by ions that directly hit the wires making up the wire grids inside the heavy ion recoil chamber. The wires for this heavy ion recoil chamber were spaced 1 mm apart, and it has been hypothesized that this effect will mitigated by changed the spacing between the wires in the grids from 1 to 2 mm spacing.
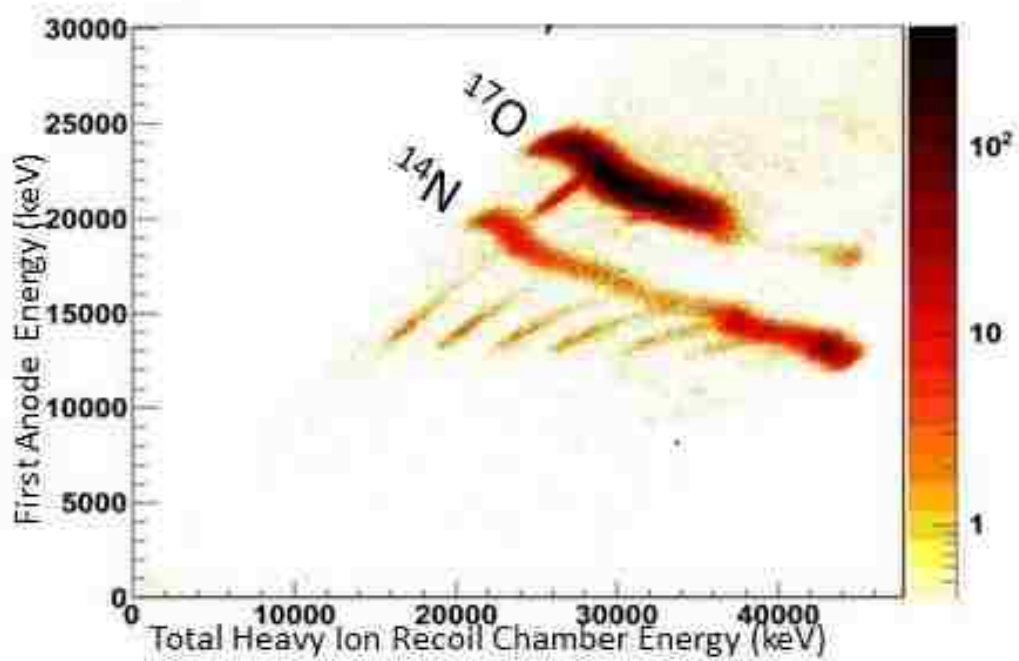
43

Figure 6-5 ΔE versus E of the HIRC for $^{17}O(p,\alpha)^{14}N$ experiment performed at FSU's RESOLUT facility.

CHAPTER 7. ^{17}F+p EXPERIMENT DESCRIPTION

We measured the ^{17}F+p elastic scattering cross section following a similar approach to that used for the ^{17}O+p test experiment. A ^{17}F beam was produced at RESOLUT and used to bombard a 2.05-mg/cm^2 polypropylene (CH$_2$)$_n$ target. Scattered protons were detected in the segmented double-sided silicon telescope that was positioned 6.60 cm downstream of the target ladder to subtend laboratory angles of $8°<\Theta<24°$. The silicon telescope consisted of 65 and 1000 μm thick model S2 silicon detectors manufactured by Micron Semiconductor. Signals from the silicon array were processed using the external LASSA preamps connected to HINP16C preamplifier chips and the ANSAEN ASICs electronic system described previously.

Recoiling ^{17}F ions were detected in the HIRC mounted 25.72 cm downstream from the target with a 6.35 cm diameter mylar window (2 mg/cm^2). This HIRC detector provided ΔE-E particle identification information for heavy ions detected in coincidence with protons. This configuration was tested previously with the ^{17}O(p,α)^{14}N measurement, and the coincidence efficiency was found to be 87% or better, showing a 2% transmission loss per grid. The unscattered primary beam was prevented from entering the ionization counter by a 1 cm diameter disk that was mounted on a wire and inserted in front of the ionization counter entrance window (23 cm from the target) during data collection. The size of the disk was chosen so that the majority of the unscattered beam ($\Theta_{lab}<1.3°$) was blocked, but the scattered ^{17}F ions were able to be detected when protons were detected in coincidence by the silicon telescope. This allowed us the ability to run the beam at a higher current but reduce pileup.

7.1 ^{17}F Beam Production

The major differences between this ^{17}F experiment and the measurement with a ^{17}O beam described earlier are in the use of a thick target, the ^{17}F beam properties, changing to a 65 μm ΔE detector, and the angles covered. The radioactive ^{17}F beam was produced at FSU's RESOLUT facility using the ^{16}O(d,n)^{17}F reaction with an 79 MeV beam of ^{17}O from the Tandem Van de Graff accelerator and the heavy ion linear accelerator. The ^{16}O beam bombarded a (liquid nitrogen) cryogenically cooled deuterium, D$_2$, gas target to produce the ^{17}F beam by the inflight method [Pep09]. This technique takes a beam and sends it through a gas target to create a secondary beam via a nuclear reaction. The recoiling heavy ions downstream of the gas target were collected with a large-bore solenoid magnet, separated from unreacted ^{16}O using the RESOLUT system, producing a ^{17}F beam (~10^5 particles per second) with ~70% purity at the experimental station.

The most important resonances for the $^{14}O(\alpha,p)^{17}F$ reaction are likely the 3 negative parity states in the excitation energy range from 6.1 to 6.4 MeV. The primary aim of this measurement was to provide an accurate and independent measure of the energies and widths of these states. Our chosen approach was to utilize a thick (2 mg/cm^2) polypropylene target in conjunction with a ^{17}F beam at an incident ^{17}F beam energy that would be just slightly above the energy regime of interest. However, the ^{17}F beam is created by the $^{16}O(d,n)^{17}F$ reaction first. The production of ^{17}F is more favorable at higher energies due to the higher production cross section and the more efficient collection of forward-focused reaction products from the (d,n) reaction. Ultimately, a 79 MeV beam of ^{16}O was chosen as the primary incident beam to increase production of the secondary ^{17}F beam, while still covering the energy regime of interest within a target of modest thickness.

Given a 79 MeV incident ^{16}O beam, we calculated the most probable energy for the resulting ^{17}F beam to be 55 MeV using energy loss and kinematic functions found in LISE++ [Tar08]. The ^{16}O beam entered the cryogenic gas cell through a 2.5 μm thick Havar window. After the window, the ^{16}O beam passed through a 40 mm thick gas cell of molecular deuterium, D$_2$, at 350 Torr and 80 K. We calculated kinematics for the $^{16}O(d,n)^{17}F$ reaction (Q=-1.624 MeV) and assumed that the median energy for ^{17}F production would originate from reactions occurring at the center of the gas cell. Energy loss of the beam and products were calculated through the remainder of the gas cell and through the second 2.5 μm thick Havar exit window, with the result that the most probable energy for the ^{17}F beam would be at about 55 MeV. The $^{17}F/^{16}O$ beam downstream of the gas target was collected and separated using RESOLUT, a combination of solenoid and bending magnets. The RESOLUT component settings were optimized to produce a ^{17}F beam with optimal intensity and purity, which measured incident energy of the ^{17}F energy of 54.7 MeV in good agreement with our calculations. With this energy beam and a 2.05 mg/cm^2 thick target, the measurement would cover center of mass energies from of 2.053 MeV to 2.985 MeV, scanning the region where all three important resonances are expected.

The ^{17}F beam was contaminated with a 46 MeV beam of $^{16}O^{8+}$ ions that have nearly the same magnetic rigidity as the ^{17}F beam. In between runs, the disk at 0° was removed, and a 9 mm aperture was inserted for beam tuning and beam purity measurements using the ion counter. Figure 7-1 shows a ΔE versus E particle identification spectrum (a plot of the energy loss in the upstream (ΔE) section of the gas ionization chamber versus the total energy) for a representative run with the beam directly into the ionization chamber with no target. There is a clear distinction
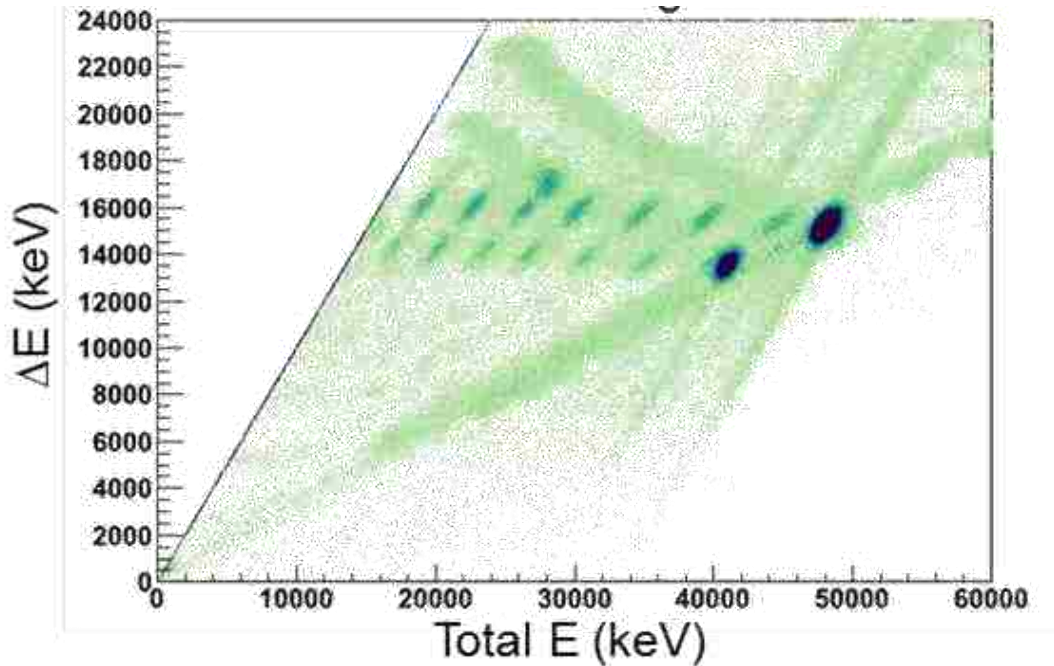
Figure: 7-1 ΔE versus E plot with beam directly into the HIRC, using no target and no blocker. The fluorine line is located above the oxygen line.

between the fluorine and the oxygen ions. The "shadows" periodically appearing at the same ΔE, but lower E than the main F and O groups arise from particles that stop on one of the grid electrodes in the ionization chamber and do not deposit their full energy in the gas in the E section. The average beam current was 3×10^4 ^{17}F/^{16}O ions per second, with an average purity of about 70% ^{17}F.

We accumulated data for a total of 100 hours and 39 minutes, corresponding to a number of total integrated ^{17}F ions of 6.5×10^9 at incident energy of 54.7 MeV on the 2.05 mg/cm^2 CH$_2$ target. In the following sections the analysis and results of the data will be discussed.

7.2 Raw Data

We restrict the analysis to events where only 1 ring and 1 segment in the E silicon detector have data. This cut eliminates all the particles that stop in the ΔE (e.g. heavy ions) and the pulser signal that were introduced into many of the silicon channels as a diagnostic. It also eliminates some events that have cross talk between channels or shared energy between channels. This cut will eliminate a small fraction of proton scattering events, but the cut should be independent of the proton energy, and later we describe the fraction of scattering events that are eliminated. Figure 7-2 is a spectrum of the counts versus the sum of the energy detected by the ΔE and E silicon
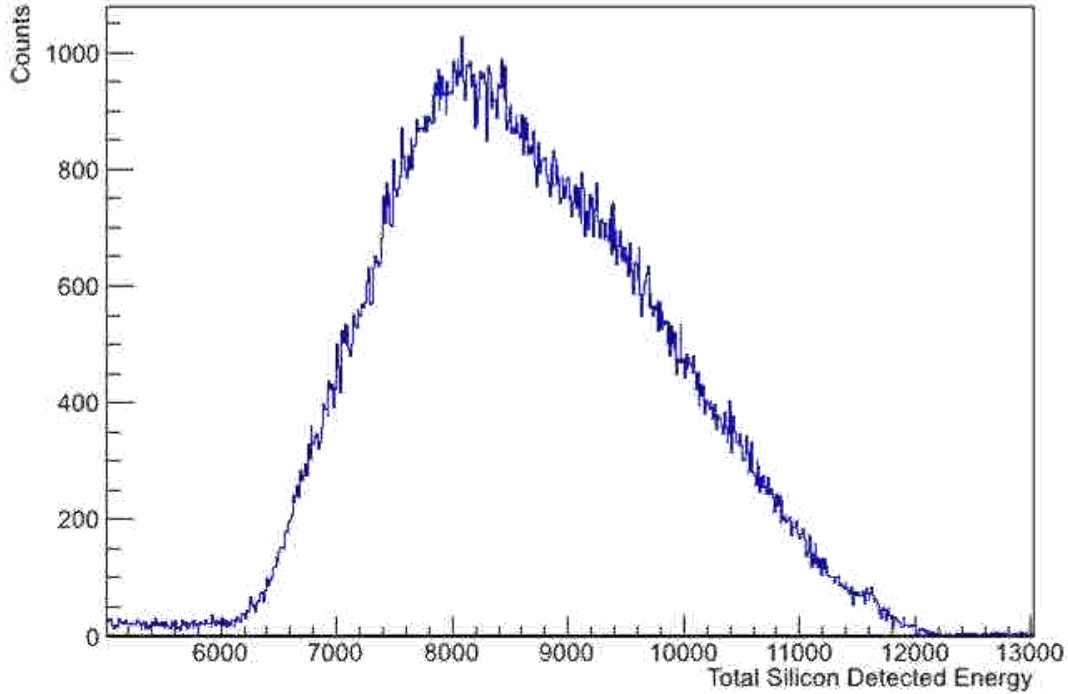
Figure 7-2 Counts versus Total Silicon Detected Energy (keV) from the S2 telescope for the experimental data.

detectors from the experiment without any cuts. This spectrum is predominately elastically scattered protons from all the beam components. The same data with the addition of the 1 ring and 1 segment requirement, and in a ΔE versus E plot of the energy loss versus residual energy detected in the silicon telescope shown in Figure 7-3.

The Z identification in the ionization chamber is crucial for distinguishing $^{17}F+p$ scattering from other channels or reactions due to contaminates in the beam (oxygen). A raw ΔE-E spectrum from the gas ionization chamber for data collected during the experiment using the 2.05 mg/cm^2 polypropylene target is shown in Figure 7-4. The ionization chamber is triggered by events in the silicon strip detector array. Events from $^{17}F+p$ (and $^{16}O+p$) scattering are clearly visible and are well resolved by the Z identification in the ion chamber. It should be noted that the only requirement on this spectrum is that there has been some trigger from the silicon array. Other gating requirements, which are also used below, will greatly reduce the background in the ion chamber spectrum.

7.3 Typical Data Cuts

The fact that the ionization chamber is triggered by an event in the silicon detector telescope has already introduced a loose requirement on a coincidence between the two instruments. However, elastic scattering events can be selected fairly cleanly by introducing a more rigorous time requirement between the two detectors. A Time
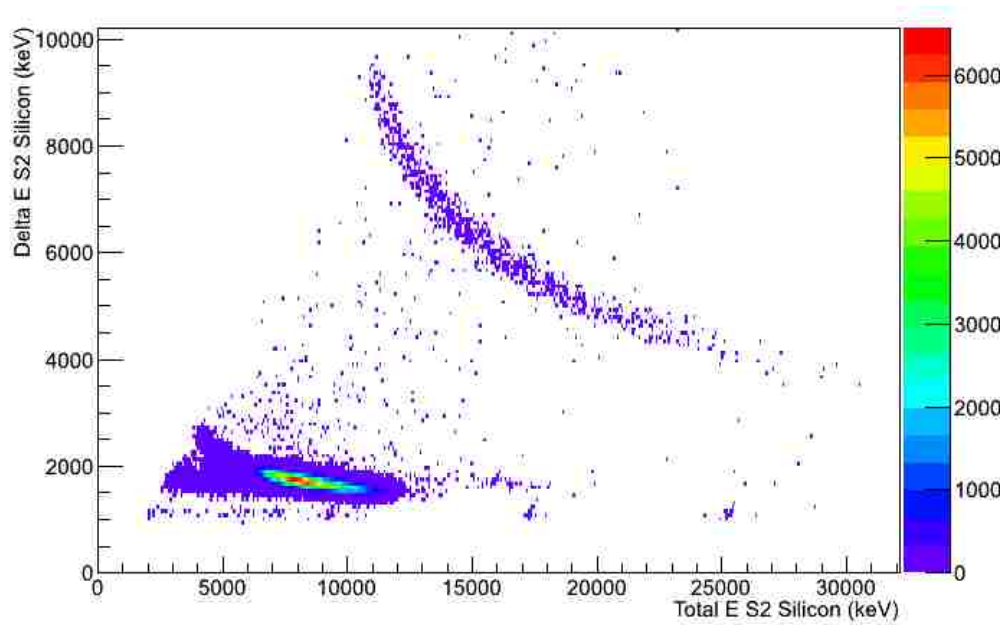
Figure 7-3 ΔE versus E plot of the silicon telescope data with one ring and one segment requirement.
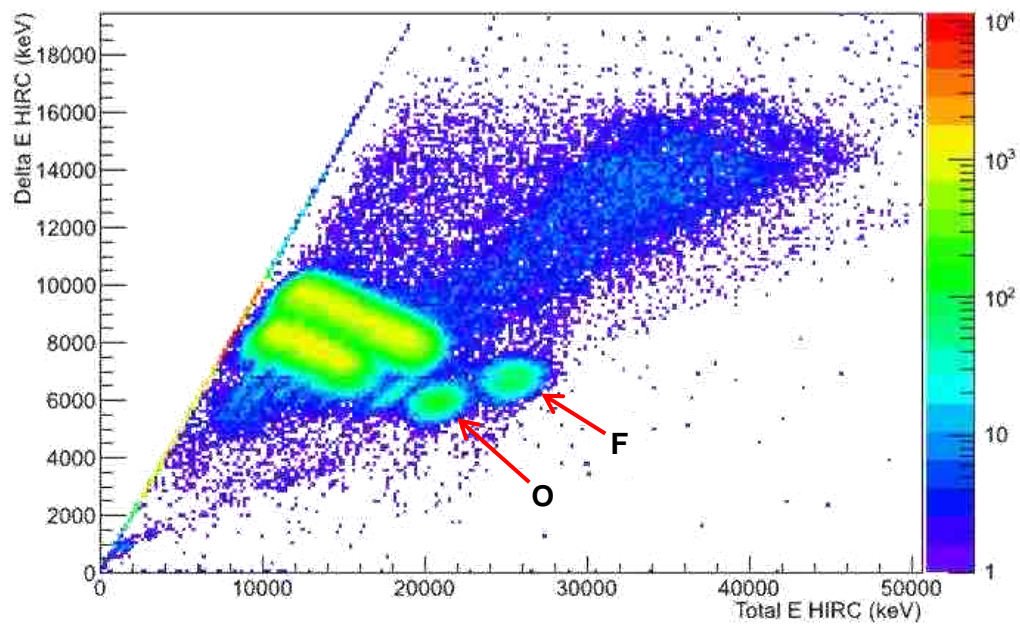

Figure 7-4 ΔE versus E plot of the experimental data with a thick target and blocker.

-Digital-Converter (TDC) signal is generated by a start from an event in the silicon detector and a stop by the ΔE signal from the gas ionization detector. Figure 7-5 shows this TDC signal with a gate on the [17]F+p scattering in the ionization chamber. The coincidence timing peak is clearly identified in this manner, and we set a timing coincidence gate on the TDC signal between the channel range of 1900 and 2300.
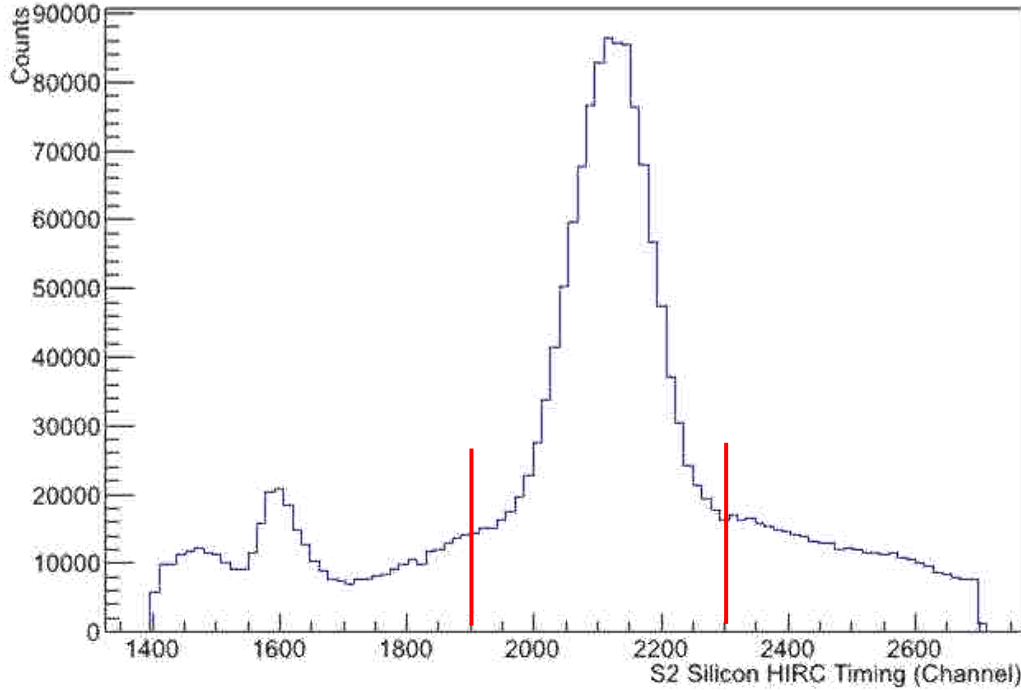
Figure 7-5 Counts versus channel for a time of flight with no cuts. The TDC cut illustrated by two red lines.

A silicon ΔE-E spectrum with the TDC cut applied is shown in Figure 7-6. The TDC cut has already highly suppressed the alphas that result from fusion evaporation as can be seen in comparison to Figure 7-3. Proton events can be very cleanly selected by gating on the silicon ΔE-E. Unfortunately, as can be seen in Figure 7-7, the protons, and especially the high energy protons, are close to the low energy threshold in the ΔE detector. The ASIC electronics does not always trigger reliably so close to the threshold, and it is clear from Figure 7-6, that there are a significant fraction of high energy proton events that have no recorded signal in the silicon ΔE. Due to kinematic calculations, the highest energy that protons can deposit in the ΔE detector is expected to be 2.55 MeV, and the observed highest energy for the proton band in the silicon is in good agreement with this expectation. To recover events that have signals below threshold in the ΔE, we select events in the E silicon detector which deposit less than 3 MeV or no energy in the ΔE silicon layer as proton events. This acts as a quite clean identification of protons without losing events where the proton signal in the ΔE is below the electronic threshold.

A ΔE-E ID particle identification spectrum from the HIRC with the one ring, one segment, and TDC requirements is shown in Figure 7-8, which can be compared to Figure 7-4 that shows the same ΔE-E spectrum without these requirements, illustrating the suppression of randomly correlated background. The good Z
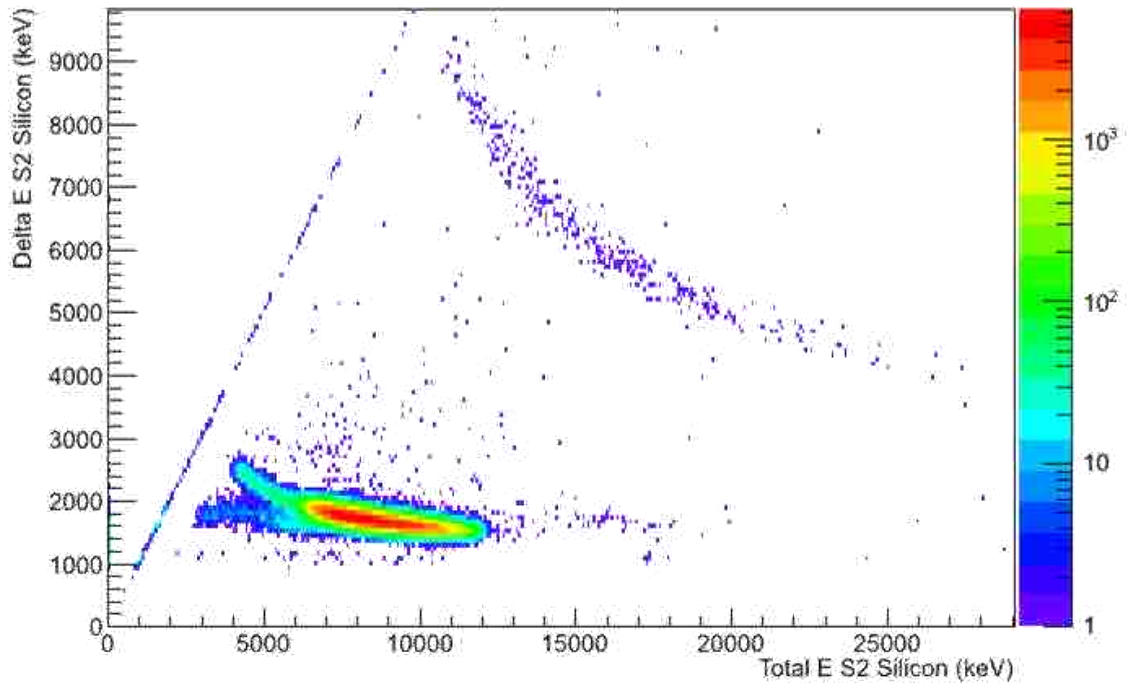
Figure 7-6 ΔE versus E plot for the silicon telescope with the TDC cut, and 1 ring and 1 segment requirements in the E detector.
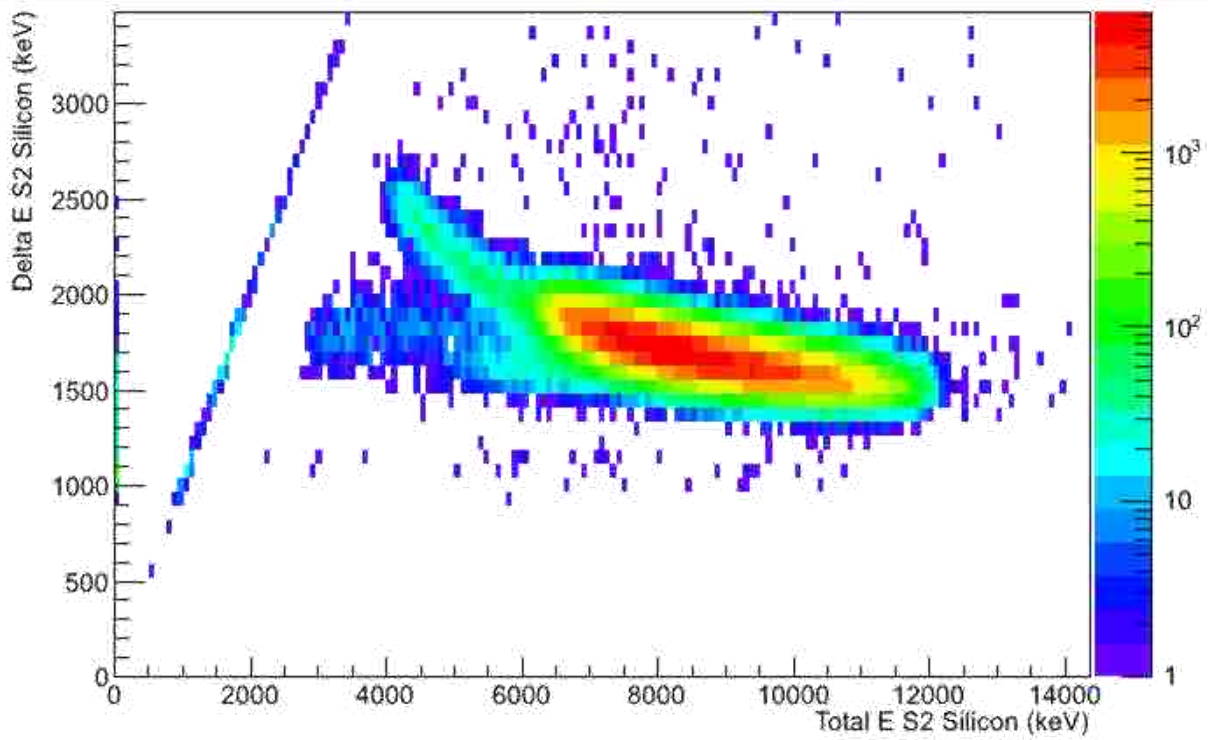

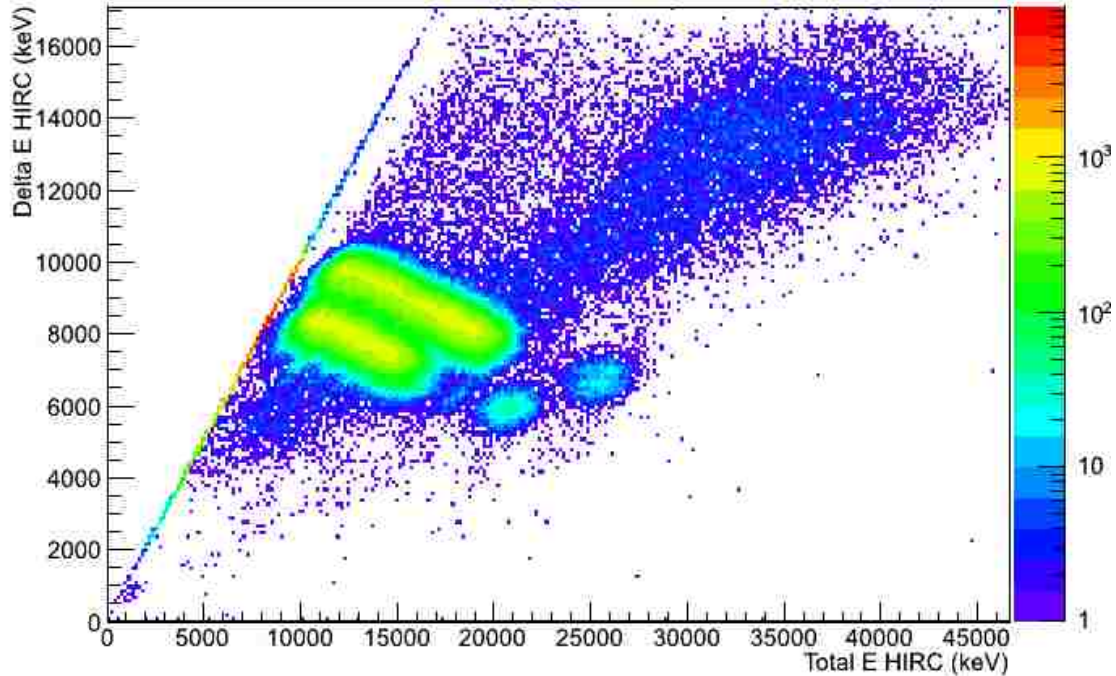Figure 7-7 ΔE versus E of the silicon telescope zoomed in on the protons.

Figure 7-8 ΔE versus E graph for the heavy ion recoil chamber with the TDC cut, 1 ring and 1 segment requirements in the E detector.

identification of the ionization chamber is important for separating the ^{17}F+p and ^{16}O+p elastic scattering events, which are kinematically similar for a given beam energy. A fluorine cut was made to select the ^{17}F+p scattering events by placing a two dimensional gate on the events as shown in Figure 7-9. Note that the highest energy group that is separated from the ^{17}F+p scattering events corresponds to leaky ^{17}F beam that misses the target and directly enters the ionization chamber. This group is in random coincidence, and is very highly suppressed by the TDC cut.

There is good separation of the fluorine and oxygen in the ionization chamber when there is a signal in both ΔE and E, but some low energy fluorine and oxygen ions do not pass through the ΔE and thus do not deposit energy in the E detector. The particles that stop in the ΔE fall on a line in Figure 7-8 and 7-9 where the summed E+ΔE value is identically equal to the ΔE. It should be noted that the separation between the line of particles stopping the ΔE and the groups that deposit energy in the E arises from the electronic threshold for observing particles in the E section of the ionization chamber.

The next step was to investigate the contribution of particles that stop in the ΔE in the ionization chamber. Figure 7-10 shows counts versus the energy detected by the segments of the E silicon detector that has been calibrated by a ^{228}Th source for protons acted on different ion groups in the HIRC. The spectrum, marked by a blue
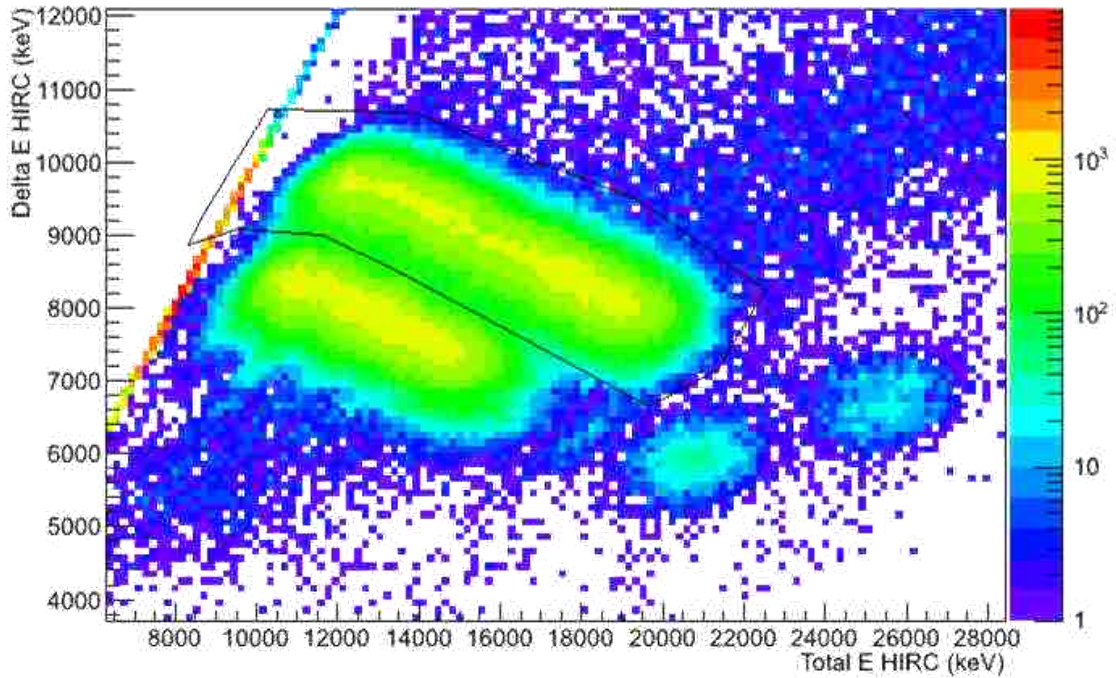
Figure 7-9 Same as Figure 7-8 but zoomed in to show the gated fluorine cut.

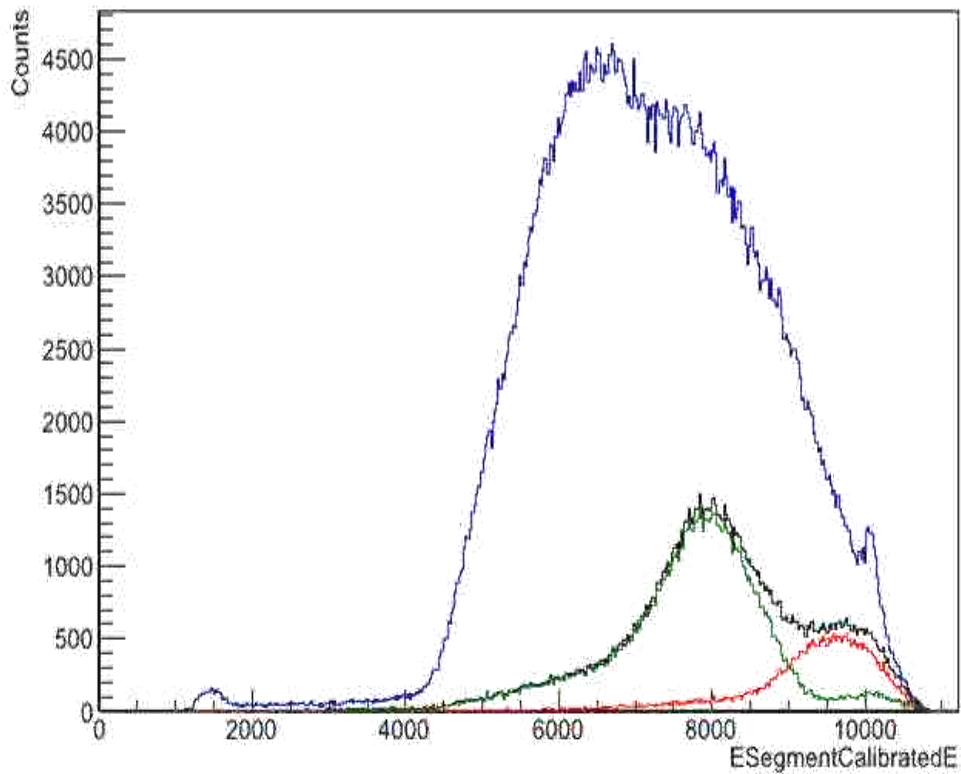

Figure 7-10 Counts versus energy detected by the segments of the E silicon detector that has been calibrated by [228]Th, where blue is all ions, black is all ions that stopped in the first anode, red is the fluorine gate of the line, and green is the oxygen gate of the line.

line, with the most events is all the protons that are detected in coincidence with the HIRC including oxygen and fluorine.

The black line in Figure 7-10 is the protons gated on the heavy ions that deposited energy only in the first anode. The smaller red peak to the far right under the blue curve is the fluorine portion of the line. Those counts represent nearly 50% of the protons which scatter in the first 10% of the target detected in this experiment. The green peak on the left is the portion of the line that corresponds to the oxygen in the heavy ion recoil chamber. There is overlap between the oxygen and fluorine in the proton spectrum. There is a significant dip between the oxygen and fluorine in the ΔE equal E line of the heavy ion recoil chamber, and we are able to make a clear enough cut between protons scattered from the oxygen and fluorine that the overlap is minimal. The heavy ion events that stop in the ΔE must be included to describe the cross section.

In Figure 7-11, we plot protons from the ΔE-E line of the HIRC versus lab angle calculated from the E silicon detector. As it can be seen from Figure 7-11, there is no angular dependence of the protons that are in coincidence with the fluorine atoms that stopped in the first anode of the heavy ion recoil chamber. Therefore, there is no reason to exclude this data from the analysis.

7.4 Beam Alignment

In the ^{17}O test measurement we found that the beam was not perfectly centered on the axis of the silicon detectors. We also found in the ^{17}F run that the beam was slightly off center, though in a different direction. Since the lab angle is one important ingredient in reconstructing the center of mass energy for each event, we determined this beam offset as described below, and corrected for it in the data analysis.

The misalignment of the beam on the axis of the silicon detectors is clear when one looks at the measured energy of particles as a function of the azimuthal angle. There should be no energy dependence on azimuthal angle, and this is the clearest indication of misalignment. In Figure 7-12, we plot the measured energy from the E silicon detector versus the azimuthal angle, which in this case just corresponds to the segment number on the silicon E. The waviness observed in the highest energy protons results from the incident beam misalignment. We corrected for this by introducing an x_0 and y_0 offset parameter in the position of the beam at the target position in our analysis. We use this offset to calculate the polar and azimuthal angles from the segment and ring number for each event assuming that the incident beam direction is perpendicular to the plane of the detectors. While the beam trajectory (i.e. the
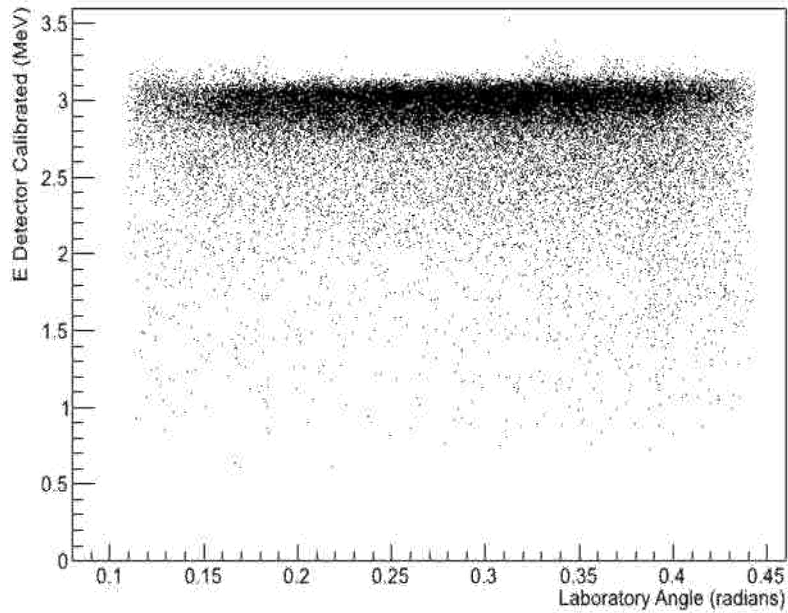
Figure 7-11 Proton Center of Mass Energy versus Lab Angle for the E silicon detector.
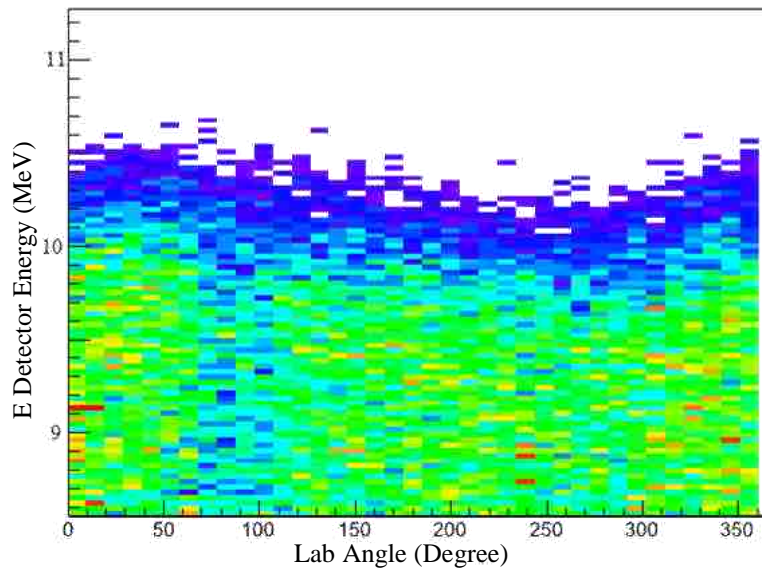
Figure 7-12 E Detector Energy (MeV) versus Lab Angle (Degree) with no beam offset.

angle instead of, or in addition to, the position at the target) might also be off, we are able to eliminate any observed

the azimuthal angle dependence of the kinematics, by introducing a slight offset in the beam position at the target.

Figure 7-13 shows the measured energy versus the azimuthal angle the values for the beam off of (x_0= -1.3 mm, y_0= -2.0mm). The maxima and minima in the energy versus azimuthal angle shift, which the azimuthal dependence
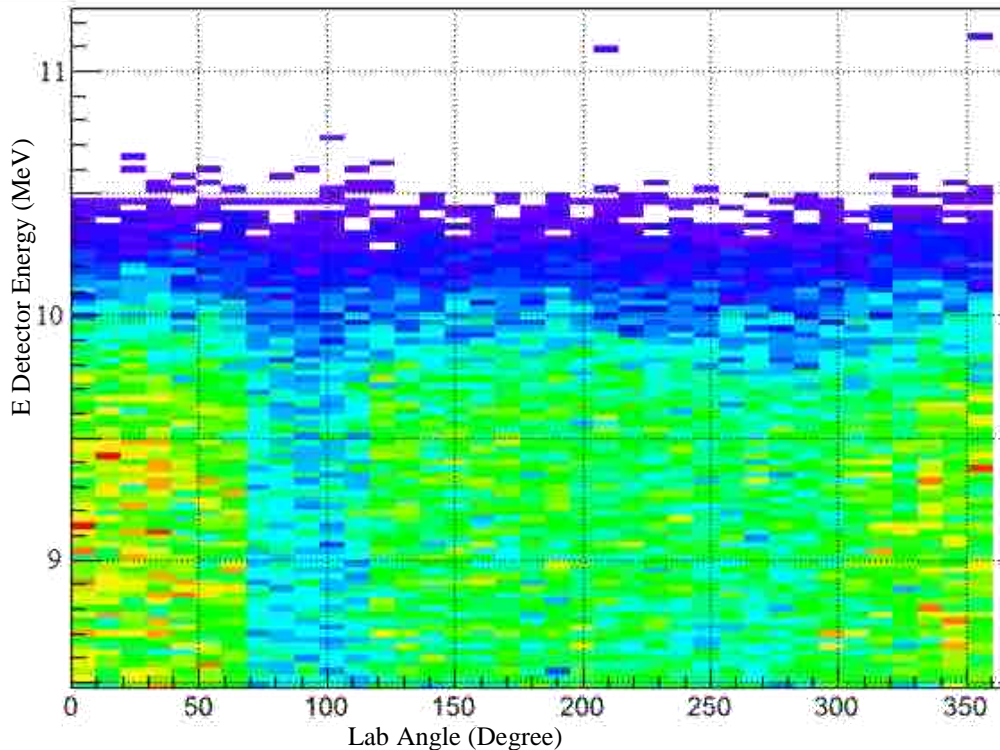
Figure 7-13 E Detector Energy (MeV) versus Lab Angle (Degree) with -1.3 mm x and -2.0 mm y beam offset.

of the kinematics has been largely eliminated. This beam offset technique has been used successfully in the analysis of the [17]O experiment described previously.

The offset in the Figure 7-14 is set at ($x_0 = $ -2.6 mm, $y_0 = $ -4.0 mm) or double the determined offset. Comparing the energy versus degree graph to Figure 7-12 it is obvious that the bumps and dips have switched places between the two graphs. The comparison between the Figures 7-12 to 7-14 indicates the validity of the beam offset that was used for these experiments.

7.5 Energy Calibration

The energy calibration is one of the most important aspects of this experiment as the primary goals are to accurately determine excitation energies and widths for observed resonances. We determine the energy for the silicon strip detectors using the rear segments (ohmic side) of the S2 silicon strip detectors, and we calibrated these detectors before and after the experiment using a [228]Th α decay source. The [228]Th source's 5.685, 6.288, 6.778, and 8.785 MeV decay lines were used to calibrate the energy spectrum for the segments of each silicon detector. The
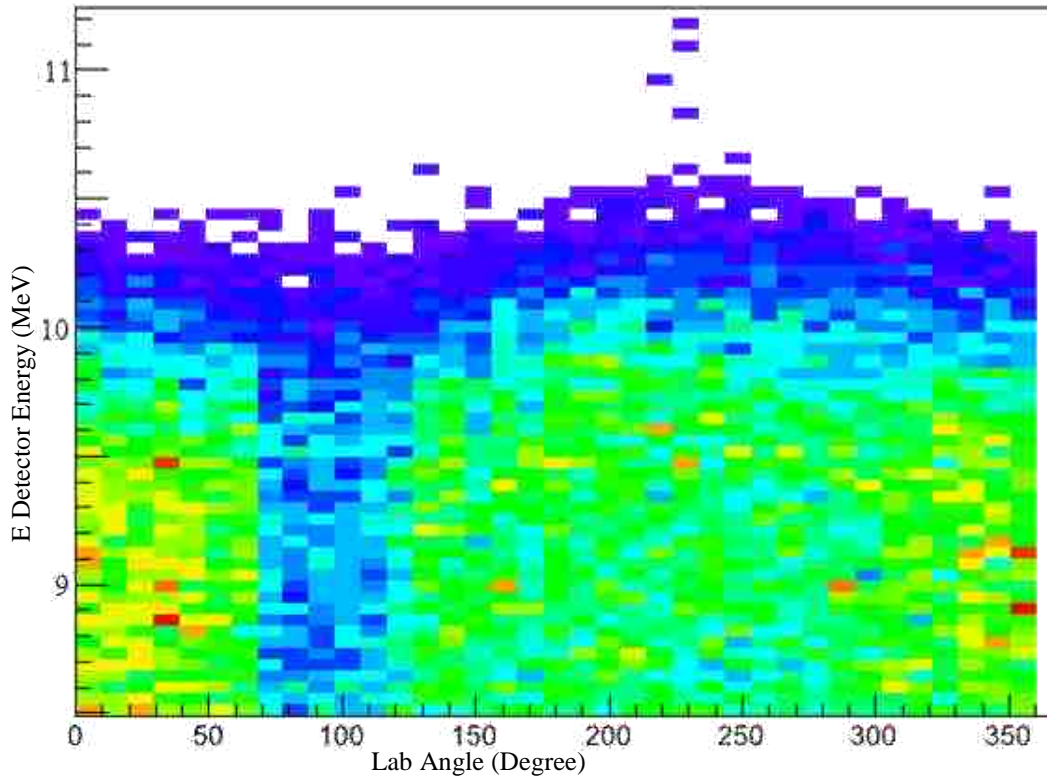
Figure 7-14 E Detector Energy (MeV) versus Lab Angle (Degree) with -2.6 mm x and -4.0 mm y beam offset.

5.42 MeV line was not used in the calibration since it was not always well separated from the 5.29 MeV line as can be seen in Figure 7-15.

To extract the centroid channel, we performed a Gaussian fit to each of the peaks corresponding to alpha-decay lines used in the calibration. In Figure 7-15 a histogram of the counts versus energy for a sample silicon segment is shown along with Gaussian fits to the peaks used in the calibration. A linear fit of the known energy to centroid channel was then performed to extract linear calibration coefficients for each signal of the detector. These calibration coefficients were then used in the analysis to determine the measured energy for each signal. In Figure 7-16 we plot the calibrated energy vs. segment number for one of the silicon strip detectors to illustrate the precision of the energy calibration.

There were two complications with using the [228]Th source calibration as an absolute calibration of the detected proton energy. First, the chamber had to be vented to insert and remove the source for calibration, which could introduce some slight changes in the energy calibration. Second, as mentioned previously many of the protons have signals in the ΔE detector that are below threshold. To use these events we must correct for the energy that is not

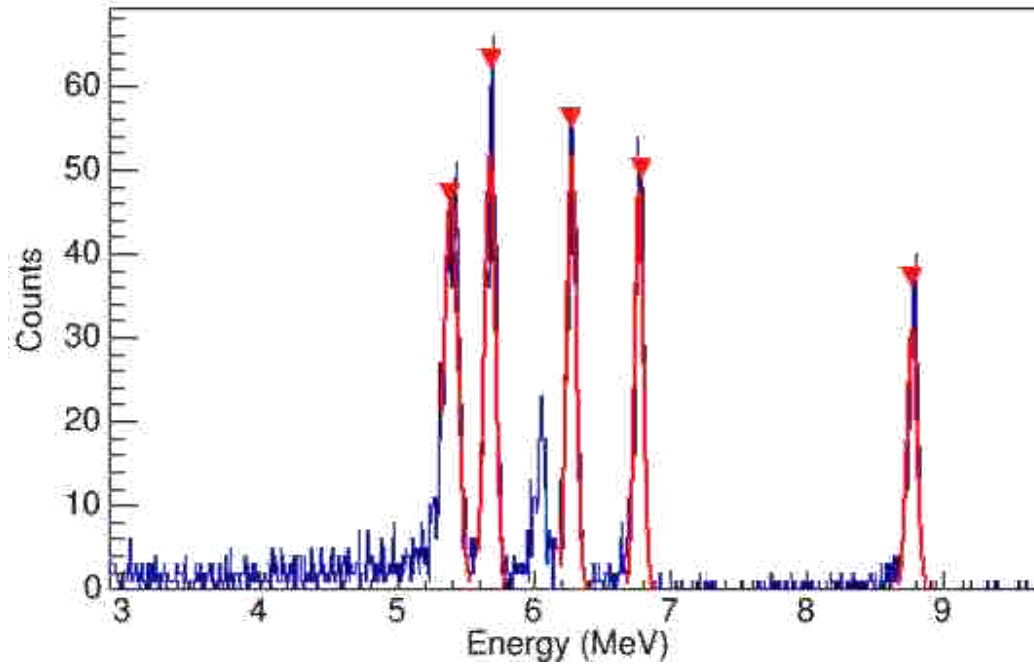Figure 7-15 A counts versus energy plot for a segment of a S2 silicon detector for a calibration run with the [228]Th α decay source.
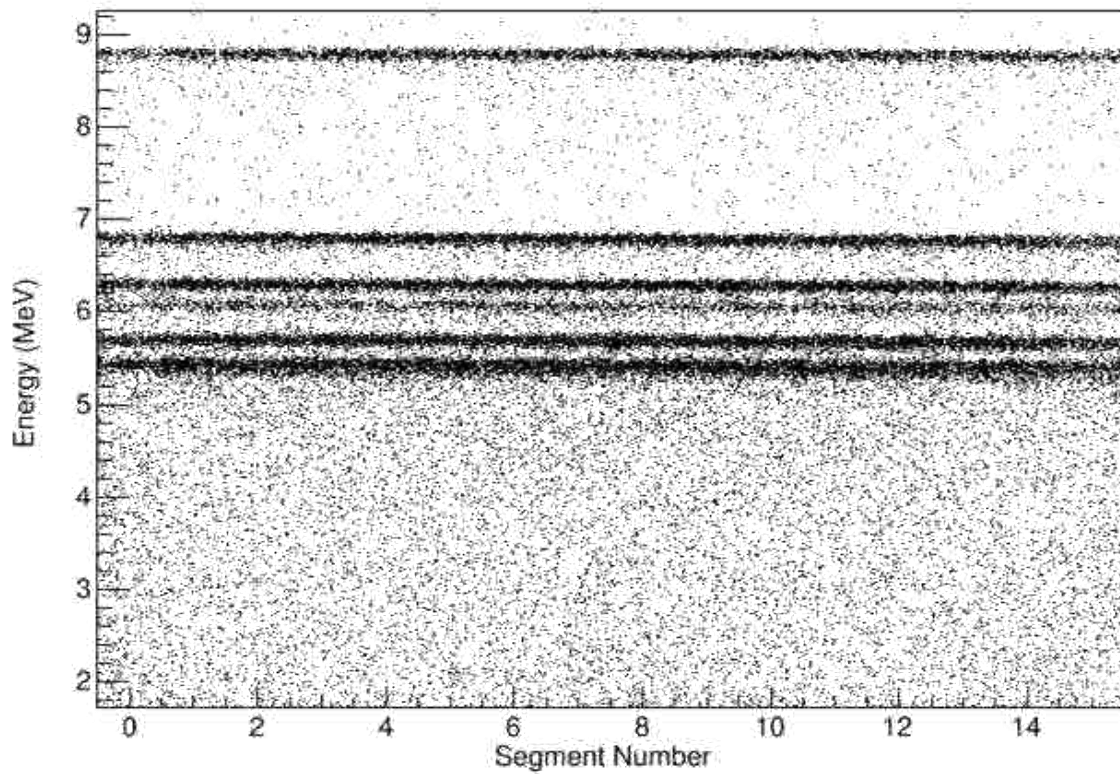

Figure 7-16 Calibrated energy versus segment number for one of the S2 silicon detectors for the [228]Th spectrum.

detected in the ΔE detector. Since this is a significant fraction of events, and the fraction varies with proton energy, it is safest to approach the data by treating the ΔE as essentially an inert absorber for the purposes of energy calibration. We used the angle calculated with the beam offset and the energy detected by the E silicon detector in LISE++ to calculate the energy loss from the protons passing through the 65 μm ΔE silicon.

Since the laboratory angle is well determined from the position on the silicon, with only a very small correction for the misalignment of the beam, the determined lowest center of mass energy should be unique for every position on the silicon target. We determined the lowest center-of-mass energy for each position on the silicon detector independently. With the corrected measured proton energy and the laboratory angle, we used LISE++ to calculate by kinematics the average ^{17}F beam energy that would be measured at the downstream edge of the target. Figure 7-17 shows the proton spectrum of a cell, a single ring and segment combination, and the high and low FWHM are highlighted with red lines. A selection of cells in Figure 7-18 depicts the properties of the individual cells before the center of mass calibration. In Figure 7-19 we plot a histogram of the number of positions versus the lowest reconstructed center-of-mass energy. The relatively small range of energies indicates the reliability with which we can determine the beam energy measurement. We fit the distribution with a gaussian to extract the mean ^{17}F beam energy at the downstream edge of the target to be 34.95 MeV. The small variation from position-to-position is likely due to variations in thickness of the DE detector, though there may also be a contribution from changes in the calibration between when the data was taken and venting the chamber to insert the ^{228}Th source.

In addition to the statistical uncertainty in the lowest ^{17}F energy that comes from the fit to the distribution shown in Figure 7-19, there may also be a systematic uncertainty with the dominant factor likely to be a difference in mean thickness from the 65 micron thickness as taken from the manufacturers specifications. We test for this systematic uncertainty in several ways. One test is to use the measured ^{17}F low energy scattered protons to check the thickness and the energy loss in the ΔE detector.

Another test is to use the highest energy protons which should be indicative of the incident beam energy. For the half maximum of the highest energy protons we used the laboratory angle and the energy measured by the E silicon detector to calculate, with LISE++, the energy loss from the protons passing through the 65 μm ΔE silicon detector. From this new adjusted energy and the laboratory angle we used LISE++ to calculate the energy lost by the proton in passing through all of the 2 mg/cm^2 polypropylene target. Finally, using the laboratory angle, the final corrected energy of the proton, and LISE++ we calculated the E$_{cm}$ and the ^{17}F beam energy for each cell.
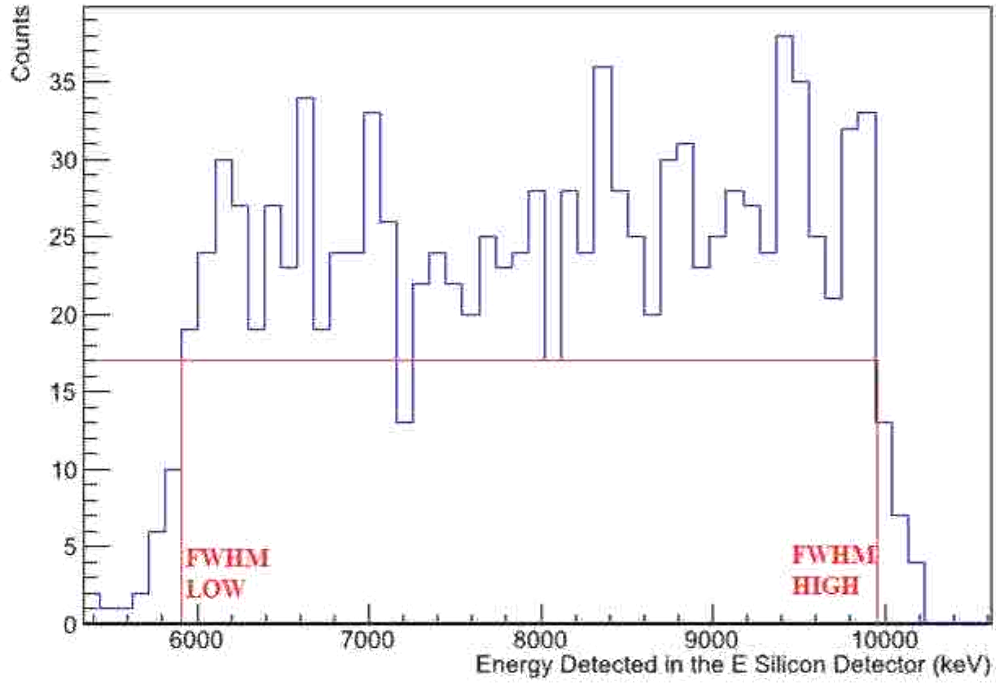
Figure 7-17 Counts versus Energy detected by the E detector and FWHM calculation of the cell being shown.
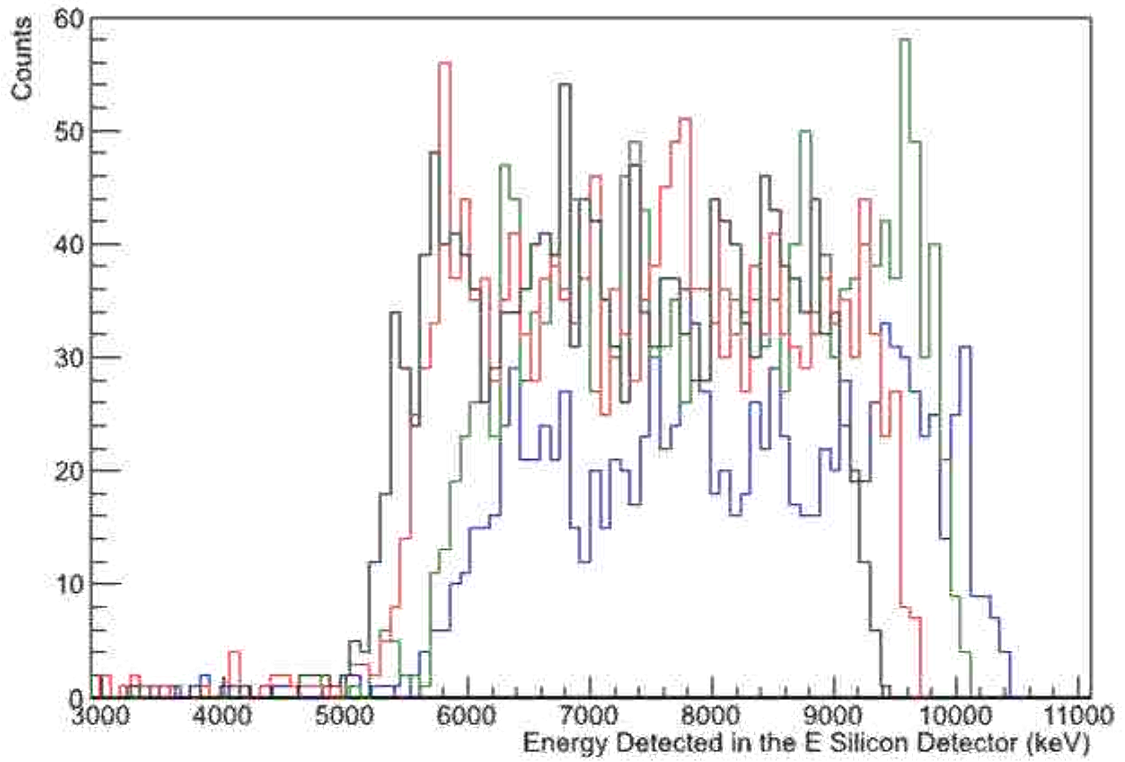

Figure 7-18 Counts versus Energy detected in the E silicon detector (keV) for various cells randomly across the detector.
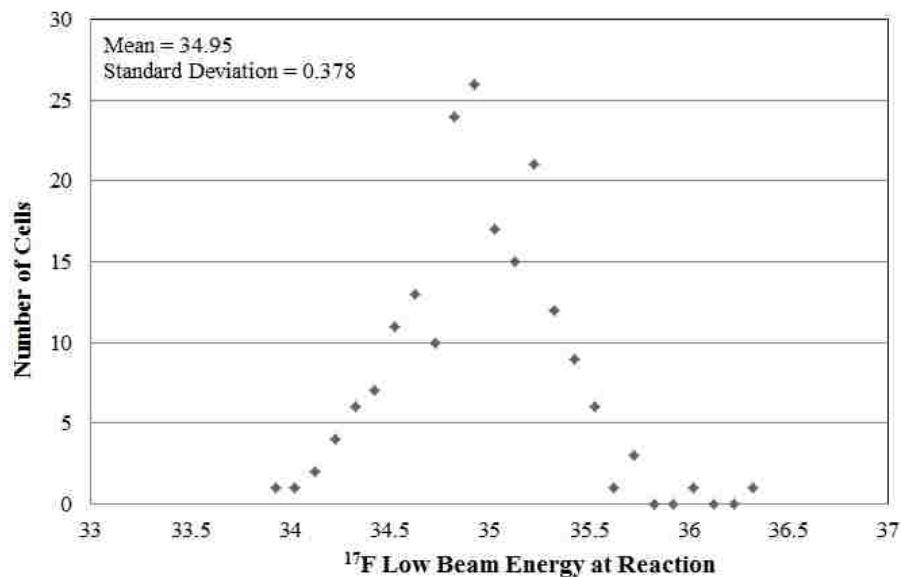
Figure 7-19 Number of cells versus calculated ^{17}F low beam energy at reaction (MeV).

Figures 7-19 and 7-20 show the calculated ^{17}F high and low beam energies for all the cells checked, respectively. The data are narrowly peaked around 34.95 and 55.09 MeV with a standard deviation of 0.378 and 0.469, respectively. From this we have determined that the experiment has an E_{cm} range of 1.96 to 3.08 MeV. To double check the calibration performed on the protons we studied all the energy data collected around the lowest energy protons of our experiment. The lowest energy protons deposited the highest amount in the 65 μm thick silicon ΔE detector. For the low energy protons, we summed the energies of the ΔE and E silicon detectors and compared it to the calculated low end beam energy. The difference in this procedure was within half of a standard deviation.

To calibrated the energy shift of each cell, we calculated the highest and lowest proton energy possible for every cell's angle from the above method and values. Then, we identified the lowest or highest energy protons from the position of the half maximum for each cell of the E silicon detector, as shown for example in Figure 7-17.

With each cell calibrated, the energy measured by the E silicon detector is translated into a center of mass energy for the protons. The previous cells in Figure 7-18 are correctly aligned by this method in Figure 7-21. This is shown in full effect in Figure 7-22 where all the proton data in coincidence with fluorine ions from the silicon detectors is shown as a combined set.

The energy resolution is dominated by three main effects. The intrinsic energy resolution of the detectors and electronics was determined from Gaussian fits to the alpha lines from the ^{228}Th calibration (see Figure 7-15). The
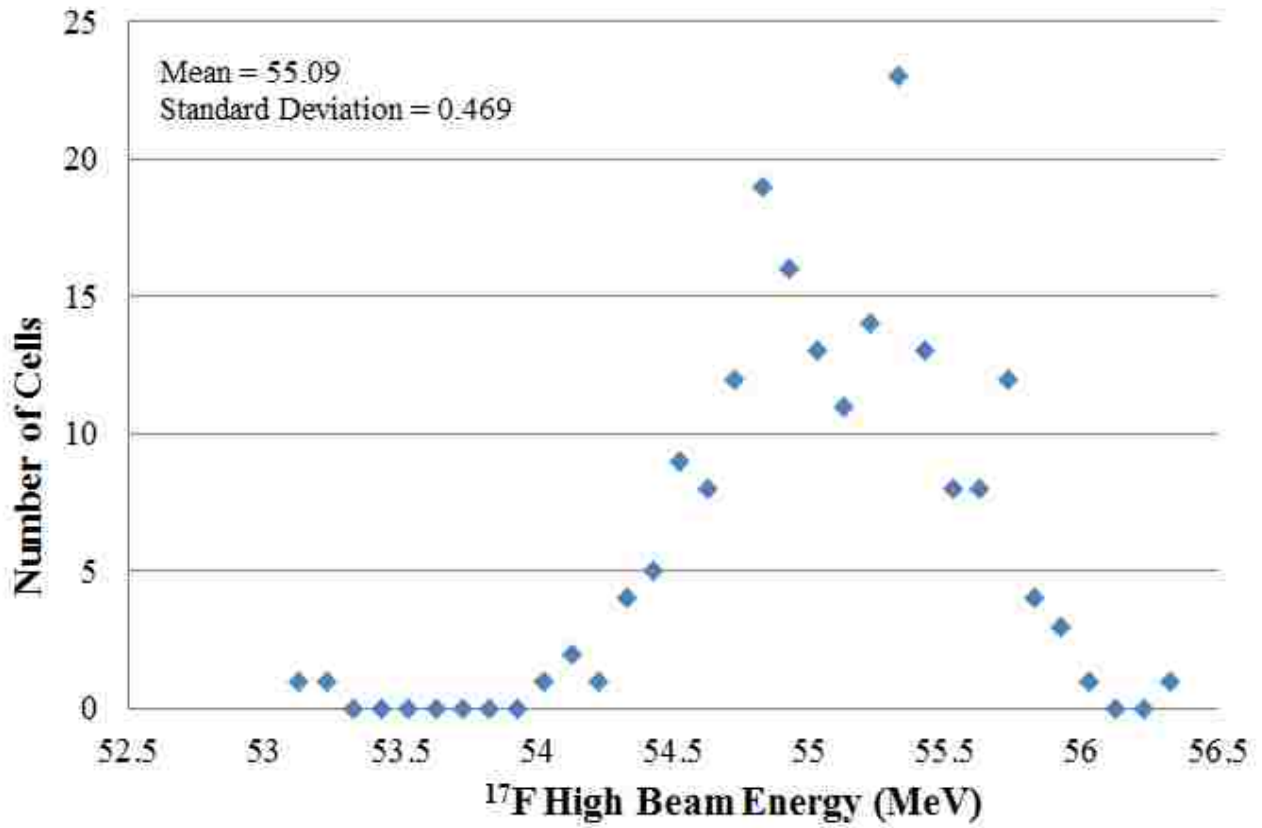
Figure 7-20 Number of cells versus ^{17}F high beam energy (MeV).
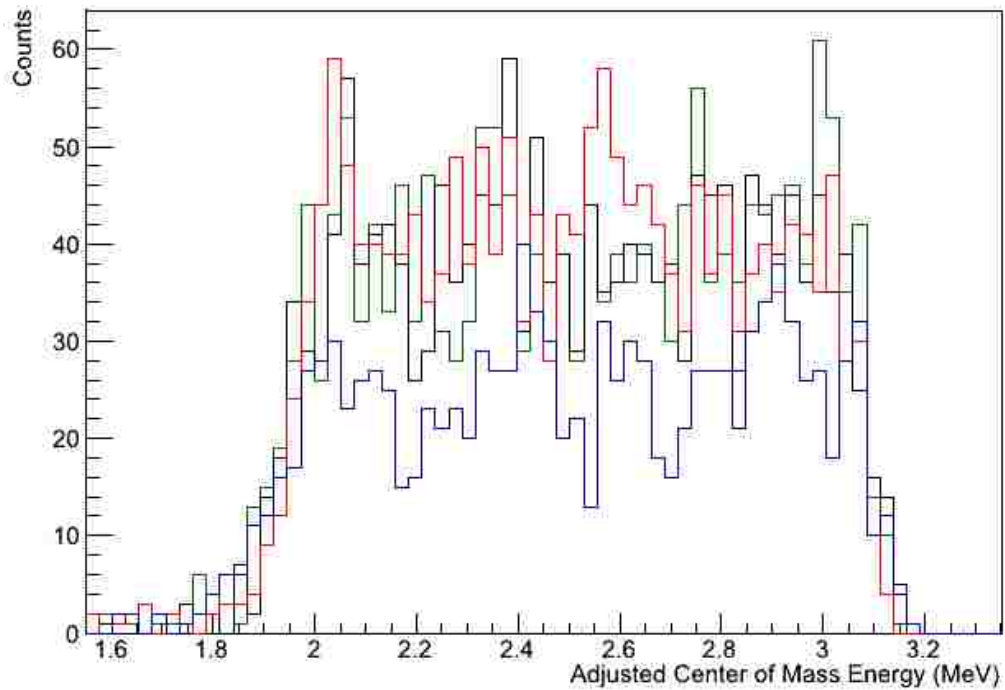

Figure 7-21 Counts versus Adjusted Center of Mass Energy (MeV).
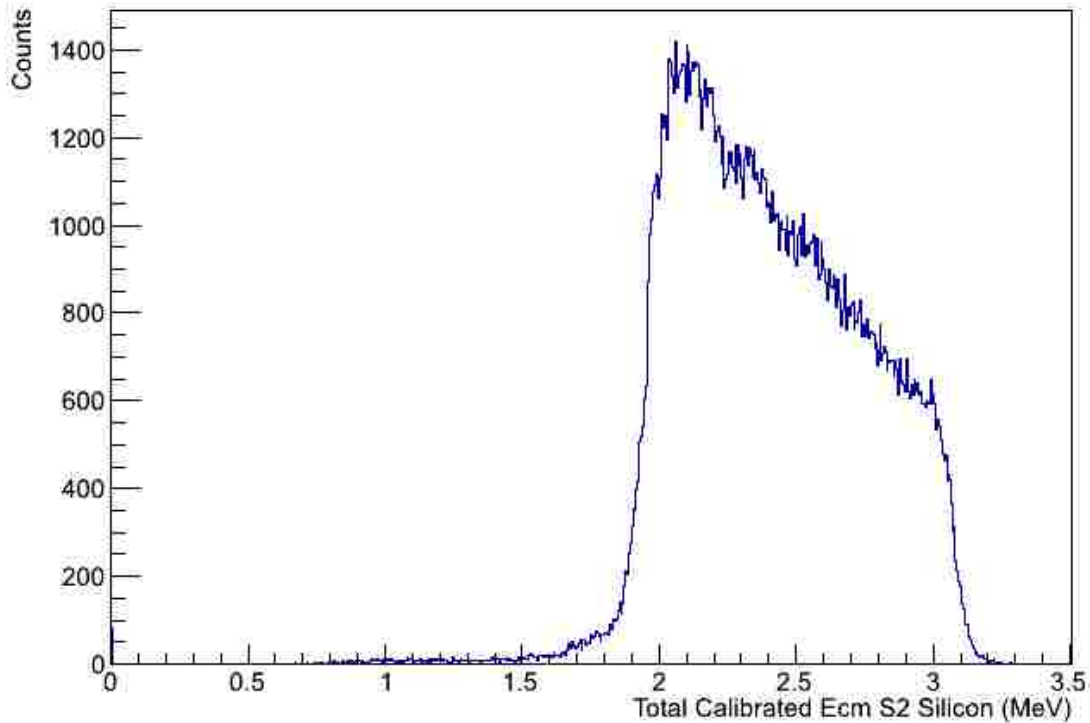
Figure 7-22 Counts versus Si measured energy (MeV) with one ring one segment, time, fluorine, and less than 3 MeV ΔE signal cuts.

resolution for most strips was consistently found to be about 80 keV (FWHM). However, the measured proton energy also suffers from energy straggling of the protons in passing through the 65 μm-thick ΔE silicon strip detector that we treat as an inert absorber. We calculated the straggling of protons in the detector using SRIM. In Figure 7-23 we show a sample calculation for the remaining energy following passage of 7 MeV protons through the 65 μm-thick ΔE detector. We find the proton energy resolution to be about 80 keV (FWHM) resulting from energy straggling, with a somewhat smaller spread in resolution at forward laboratory angles due to the higher proton energy and larger spread at higher laboratory angles. The most important effect is likely the angular resolution. From the strip size on the silicon detectors and the beam spot size, we estimate the angular resolution to be about 1.5°, corresponding to a proton energy resolution of about 115 keV. Adding these three effects in quadrature leads to an expected proton energy resolution of 160 keV, corresponding to 42 keV in the center-of-mass frame. The beam energy resolution and straggling in the target are negligible compared to these three effects. In comparing theoretical calculations with our experimental data we smear the calculated cross sections by a Gaussian resolution function with a FWHM of 42 keV.

63

Figure 7-23. Calculation distribution of proton energies (using SRIM) that result when using 7 MeV protons pass through a 65 μm-thick layer of silicon.

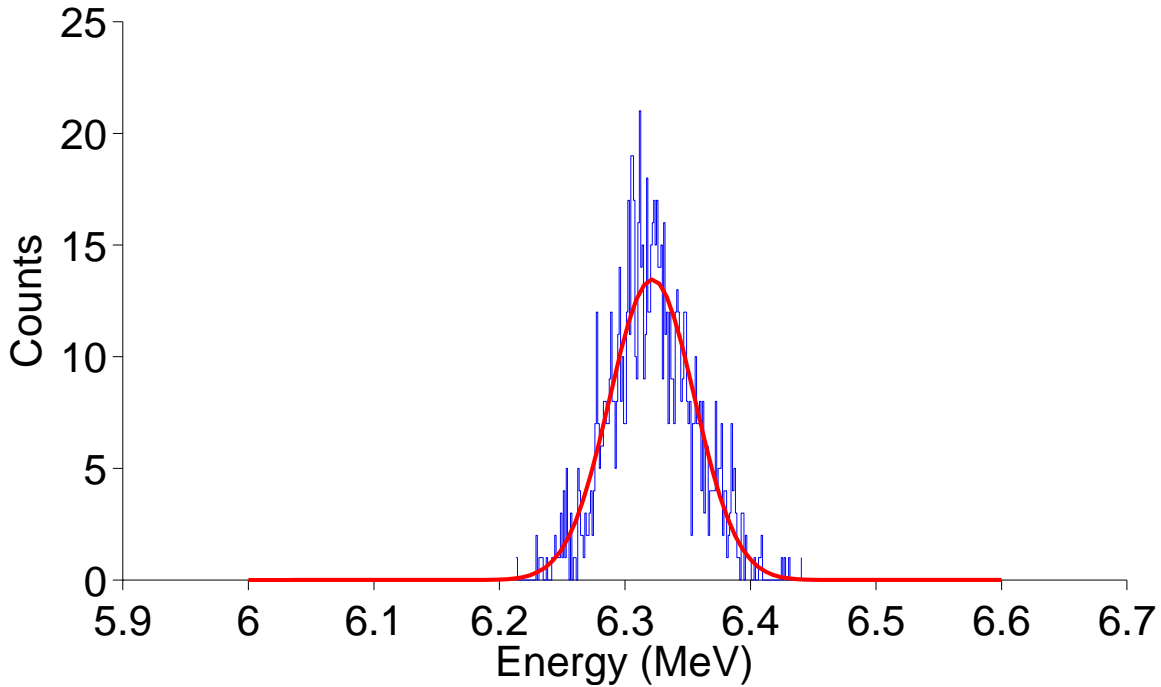Using the corrected laboratory angle detected by the E silicon detector, we were able to calculate the efficiency of the HIRC. The efficiency for the energy anode of the HIRC was calculated by the ratio of valid (one ring one segment and time cuts) silicon signals from the E detector versus the corresponding events found in the HIRC as function of E silicon detector ring ID number. Our calculated efficiencies of the HIRC are shown in Figure 7-24, and depict an angle dependent efficiency of 77 to 92%. From the below graph we can tell that the mylar window in HIRC, which is backed with wires to give it additional support against a pressure differential, has a 5% loss of signal transmission. From this experiment, we learned that each additional wire grid the heavy ion traverses induces an addition 2% loss of signal transmission.

Events that deposit energy in more than one ring or segment at a time either hit the silicon detector in such a way that the energy deposited is split between multiple parts of different cells or they are labeled as a pulser event. Due to this constraint, the efficiency of the silicon was calculated by the ratio of one ring one segment events versus the two ring two segment events as a function of the E silicon detector's ring ID number. The efficiency of our data counts becomes the difference of the cosines of the center of mass angle multiplied by the efficiency for the HIRC and the silicon detectors, as shown in Equation 7-1.

$$\cos(\theta_{cm1} - \theta_{cm2})(Effciency_{HIRC})(Effciency_{Silicon}) \tag{7-1}$$
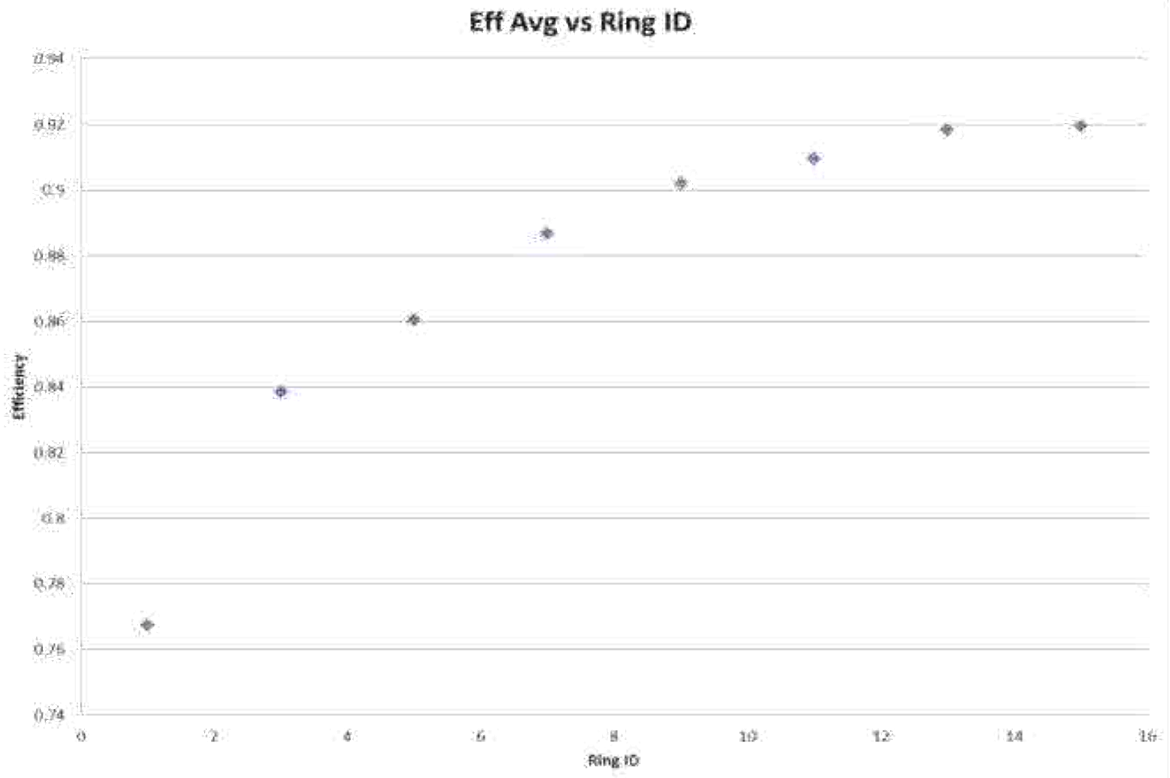
Figure 7-24 Average Efficiency versus E Silicon Ring ID.

CHAPTER 8. R-MATRIX ANALYSIS

8.1 Proton Analysis

Phenomenological R-Matrix theory provides a powerful framework for describing the energy dependence of nuclear reaction cross sections in terms of poles in the scattering matrix that can be related to properties of resonances corresponding to states in the compound nuclear system [Lan58, Bay13]. This relationship is established by matching the scattered wavefunction at an arbitrary channel radius to interior basis states described by their energy, spin-parities, and reduced-width amplitudes. The approach has been widely utilized for extracting resonance properties from scattering data and for extrapolating cross sections to low energies for astrophysics. We have analyzed our measured proton scattering excitation functions using cross section predictions made using the multi-channel R-matrix code MULTI [Nel85].

The excitation energies, angular momenta and parities of all states in the compound nucleus ^{18}Ne with $E_x < 6$ MeV are fairly well established from previous work (See Table 5.1). Most important of these low energy states are broad s-wave resonances at 4.52 MeV (1^-) and 5.11 MeV (2^+). These states have a significant influence on the cross section in the region of interest, changing both the shape of the cross section with energy and overall normalization. We fix the energies and widths of these states to those from previous measurements by Bardayan [Bar99] and Park [Par99], respectively, and do not vary them in our analysis.

The 4.52 MeV (3^+) and 4.59 MeV (0^+) states have very narrow width and are too far from the energy regime of interest to influence the cross section in our analysis, and these states can obviously be neglected. The 5.15 MeV (3^-) and 5.47 MeV (2^-) states correspond to p-wave resonances in the elastic scattering channel. They could have a minor influence on the cross section in the region of interest if their widths are significant and are deserving of more careful consideration. The only direct experimental information on the widths of these states in ^{18}Ne comes from a high resolution measurement of the ^{20}Ne(p,t)^{18}Ne reaction, resulting in weak constraints of $\Gamma = 8\ (5)$ keV for the 5.15 MeV state and $\Gamma < 12$ keV for the 5.47 MeV state [Par99]. However, the 5.10 MeV (3^-) state in ^{18}O is the mirror to the 5.15 MeV state in ^{18}Ne and was fairly strongly populated in the ^{17}O(d,p)^{18}O reaction [Li76]. The single-particle neutron spectroscopic factor was determined to be $S_n = 0.03$, or perhaps less depending on the particular partial wave contribution. A proton spectroscopic factor for the corresponding state in ^{18}Ne of $S_p = 0.03$ would imply $\Gamma_p = 3$ keV for the 5.15 MeV (3^-) state, consistent with the implications of [Par99] of $S_p = 0.08\ (0.05)$ but with a width on the lower end of the experimental range.

On the other hand, the 5.53 MeV (2⁻) state in ^{18}O, which is the mirror to the 5.47 MeV state in ^{18}Ne, was not observed in the ^{17}O(d,p)^{18}O reaction, indicating that its single particle spectroscopic factor should be significantly less than that of 5.10 MeV state, i.e. $S_n \ll 0.03$ [Li76]. A proton spectroscopic factor for the 5.47 MeV (2⁻) state in ^{18}Ne of $S_p = 0.03$ would imply $\Gamma_p = 6$ keV, indicating that the upper limit of $\Gamma < 12$ keV from [Par99] is conservative. We performed R-matrix calculations to study the possible effects of these states by including a 5.10 MeV (3⁻) state with $\Gamma_p = 8$ keV and a 5.53 MeV (2⁻) state with $\Gamma_p = 12$ keV. In Figure 8-1 we show the fractional difference between computed cross sections where both these states are included to a calculation where they are not included. Realistic parameters are assumed for the other resonances to illustrate the effect caused by interference of these states with other resonances in the region of interest. While there is an overall change in the cross section of about 1%, the shape of the excitation function with energy varies by less than 0.4%. This is significantly less than the statistical precision of our measurement, averaging about 2%, and therefore, it seems safe to neglect the effect of the 5.15 and 5.47 MeV states in our analysis.

The cross section in the region of interest is substantially affected by the properties of states at higher excitation energies, which have large uncertainties. Broad resonance states are expected, and the tails of these resonances may extend to significantly affect the shape of the cross section in the energy regime of interest. Such broad high energy states must often be included in R-matrix analyses to model the effects of the continuum and accurately reproduce measured cross sections. States with various orbital angular momentum configurations may contribute, and a challenge in extracting resonance parameters from R-matrix fits to experimental data is finding the best overall fit to the data amongst a multitude of local minima in the many dimensional parameter space.

To try to produce the best overall fit, we tried to introduce a minimum number of parameters in fitting the proton scattering data. We also employed a hybrid fitting approach combining a Monte Carlo algorithm with a gradient search technique. The algorithm utilizes a Monte Carlo approach, introducing a number of higher energy resonances with a selected set of spin-parities, for those high energy states over a broad range of parameter space. The differential cross section is then calculated for each data point using MULTI, and the χ^2 calculated using the traditional approach assuming uncorrelated uncertainties:

$$\chi^2 = \sum w \left[\left(\frac{d\sigma}{d\Omega} \right)_{data} - \left(\frac{d\sigma}{d\Omega} \right)_{Rmatrix} \right]^2$$
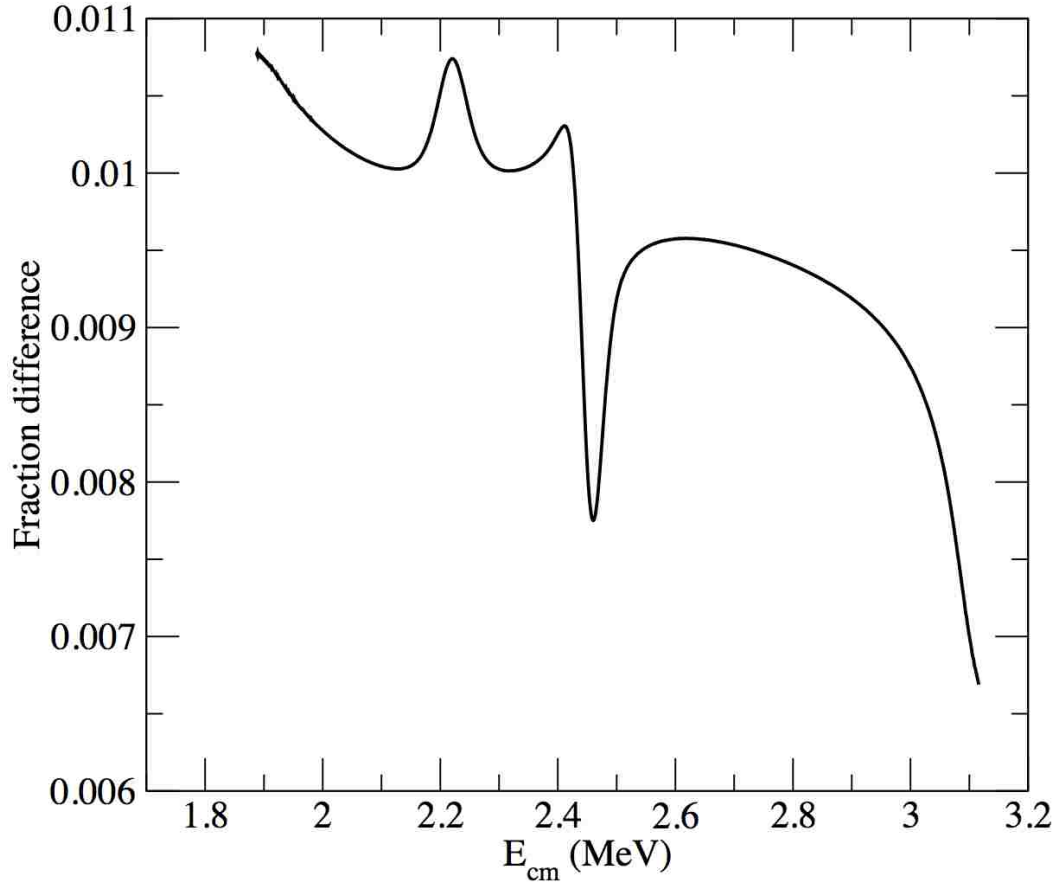
(8-1)

Figure 8-1 Fractional difference in the computed R-matrix cross section when states are included at 5.10 MeV (3⁻) with Γ_p= 8 keV and 5.53 MeV (2⁻) with Γ_p= 12 keV to the result when these states are not included.

where the weighting for each data point, w, is taken to be the square of the reciprocal of the statistical uncertainty in the data.

The parameter sets from the Monte Carlo approach that produce the lowest values for χ^2 are subsequently used as starting points for a gradient search algorithm that is converged to a local minimum value for χ^2. This approach was followed using different numbers of resonances with various choices for spin-parities, and the resulting fits were then compared and evaluated manually. In following this procedure, we often found that the fits rapidly converge to solutions with high resonance energies and/or small widths for some resonances, which likely have very little influence on the cross section at the energies of interest. In such cases, the resonances suspected of having little influence on the cross section were eliminated from the calculation and the gradient search re-evaluated to see if there was any change in the χ^2 or in the other fit parameters. This approach allows a broad region of parameter space to be explored and maximizes the probability of finding the best global minima.

We first considered fits to the data that included no resonances in the measured region of interest. The extracted average $^{17}F(p,p)^{17}F$ measured cross sections integrated over all angles are plotted as a function of the reconstructed center-of-mass energy in Figure 8-2. The highest and lowest energy data points are excluded from the fits since they are affected by the ends of the target, resulting in a total of 117 data points being used in the analysis between $E_{cm} =$ 2.053 to 2.985 MeV. The same data are also shown in Figure 8-3 with a suppressed zero and two R-matrix cross sections: one including no resonances above 2 MeV (dashed blue curve), and one including two resonances at higher energies (solid black curve). The filled black circles are data points that were included in the R-matrix fit to the data, while the open red circles are data at the extremes of the target that were excluded from the fit. In the no resonance fit (dashed blue curve), only the overall normalization of the calculated cross section was varied (requiring about a 2% adjustment for best fit), while the parameters of the only states included (the 3^+ and 2^+ states at 4.52 MeV and 5.11 MeV, respectively) where held fixed to their previously measured values [Bar99, Hah96, Par99].

We generally obtain better fits to the data by adding two higher energy resonances from the ^{18}Ne level scheme, a very broad negative parity 2^- state and a narrower 4^+ resonance just above the energy range of interest. By eliminating either of these states, fits become statistically worse. However, a broad range of possible values for these two resonances do result in comparable fits. The broad "state" prefers a negative parity (with $\ell = 1$ orbital angular momentum), and fits are shown assuming a 2^- state, though comparable fits often also could be obtained using 1^- or 3^- states with different energies and partial widths. The preferred values for the 4^+ resonance roughly agree with properties of a known state [Har02, Hah96]. This 4^+ resonance gives the slight upturn to the cross section at higher energies. The solid curve is a 5 parameter fit to the data where the overall normalization and energies and widtha of the 2^- and 4^+ state were varied. The fit parameters are summarized in Table 8-1.

Any of the fits to the data are not very good when resonances are excluded from the energy region measured. When no resonances are included at higher energies (dashed blue curve in Figure 8-3), the best fit results in $\chi^2 = 474$, corresponding to $\chi^2/\nu = 4.09$ as there is only one free parameter (the overall normalization). The best fit we obtained while adding two higher energy resonances (solid black curve in Figure 8-3) corresponds to $\chi^2 = 193$ or $\chi^2/\nu = 1.68$ (5 parameter fit). Many other combinations of higher energy resonances were added to try to improve the fit. The improvement we found, however, was always statistically insignificant as the shape of the cross section with two higher energy resonances already follows the general trend of the data in the region of interest fairly well.
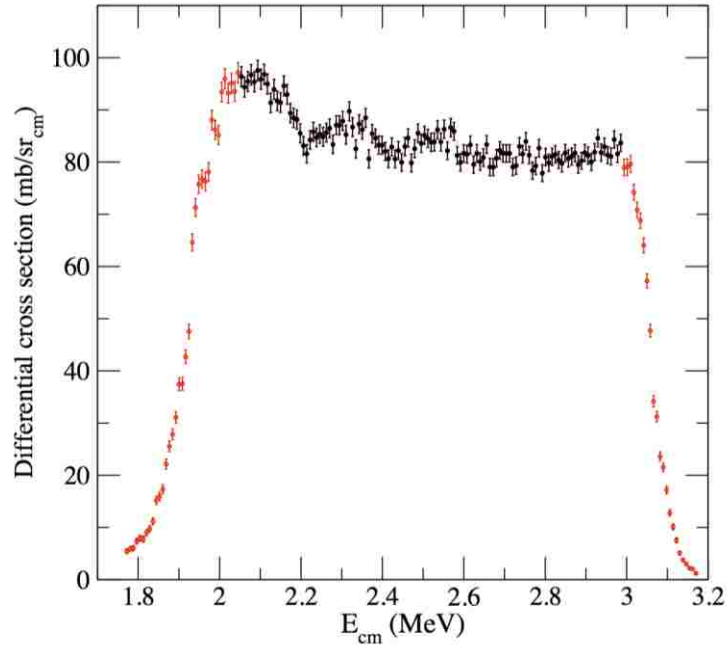
Figure 8-2 Measured differential cross section for the ^{17}F(p,p)^{17}F reaction over the entire detector averaging θ_{cm}=144.7°. The 117 filled black data points are used in R-matrix fits, while the open red data points are affected by the ends of the target and are excluded from fits.
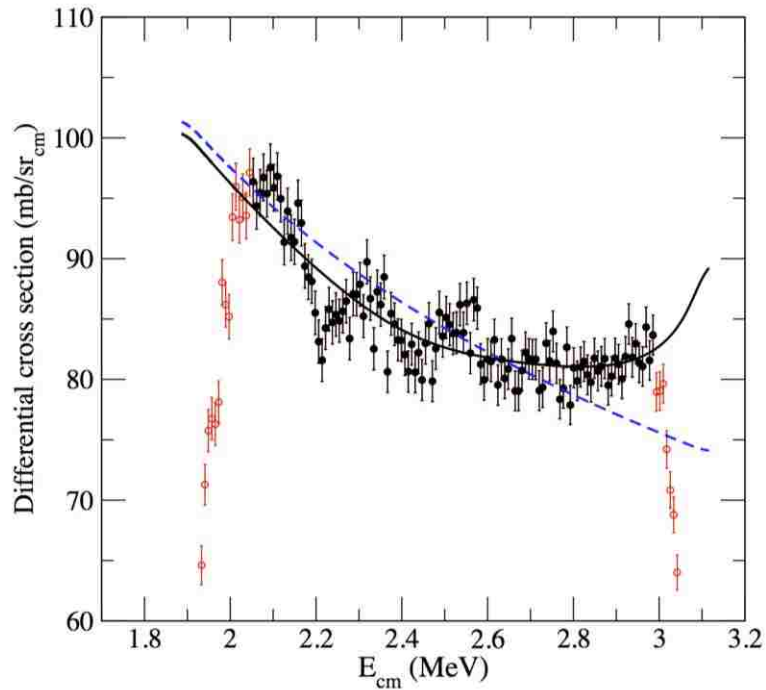
Figure 8-3 The same data as in Figure 8-2, but shown over a more limited range. The dashed blue curve is a fit to the data varying only the overall normalization, with only states included at E_x=4.5 and 5.1 MeV with properties fixed to previously measured values (see Table 5-1). The solid black curve is a 5 parameter fit that includes a 4^+ and a broad 2^- state at higher energies.

Table 8-1 Summary of best fit resonance parameters.

| χ^2	# param	χ^2/ν	E_r (1⁻)	Γ_p (1⁻)	E_r (3⁻)	Γ_p (3⁻)	E_r (2⁻)	Γ_p (2⁻)
193	5	1.68	-	-	-	-	-	-
137	8	1.26	2220	42	-	-	-	-
112	11	1.06	2220	42	2451	5	-	-
98	11	0.92	2220	42	-	-	2432	119
98	14	0.95	2220	53	2483	3	2424	62
98	14	0.95	2220	53	2420	2	2451	87
100	14	0.97	2424	104	2475	2	2224	52*

*Best fit 2⁻ resonance at 2.22 MeV includes a proton partial width to the first excited state of 17 keV

The shape of the measured excitation function exhibits two relatively narrow features around $E_{cm} \cong 2.2$ MeV and 2.4 MeV that are not described by smooth changes in the excitation function which are caused by tails of other resonances. The features are present at excitation energies in the region corresponding to $E_x = 6.1\text{-}6.3$ MeV where 3 previous states have been observed in ^{18}Ne that likely have a significant influence on the ^{14}O(α,p)^{17}F reaction rate. As discussed in Section 5, these states all have negative parity and can be populated by $\ell = 1$ (p wave) in the ^{17}F+p entrance channel.

The lowest energy of these states at 6.15 MeV is well separated from the other two states (by at least $\Delta E_{cm} \cong 150$ keV) and may give rise to the lowest energy feature in our excitation function. As discussed in Chapter 5, this state is constrained to be either 1⁻ or 2⁻. The two higher energy states in the region are separated by only about $\Delta E_{cm} \cong 50$ keV, are likely not resolved in our measurement, and probably give rise to the feature in the excitation function near $E_{cm} \cong 2.4$ MeV. One of these two states is almost certainly the mirror to the 6.40 (3⁻) state in ^{18}O. We fit the measured excitation function by adding a single 1⁻ resonance to the excitation function in this energy region, which is shown in Figure 8-4 as a dashed blue line. We also fit the excitation function by adding both a 1⁻ and a 3⁻ state, and this fit is shown in Figure 8-4 as a solid red curve. Adding the single 1⁻ state produces a best fit with χ^2=137 (χ^2/ν=1.26 from 8 parameter fit) and adding both a 1⁻ and a 3⁻ state results in a fit with χ^2=112 (χ^2/ν=1.06 from 11 parameter fit). The best fit results are summarized in Table 8-1. The substantial improvement in the fit obtained in each case demonstrates that we have observed at least two $\ell = 1$ (p wave) resonances in the energy range where they are expected from the previous transfer and scattering measurements.
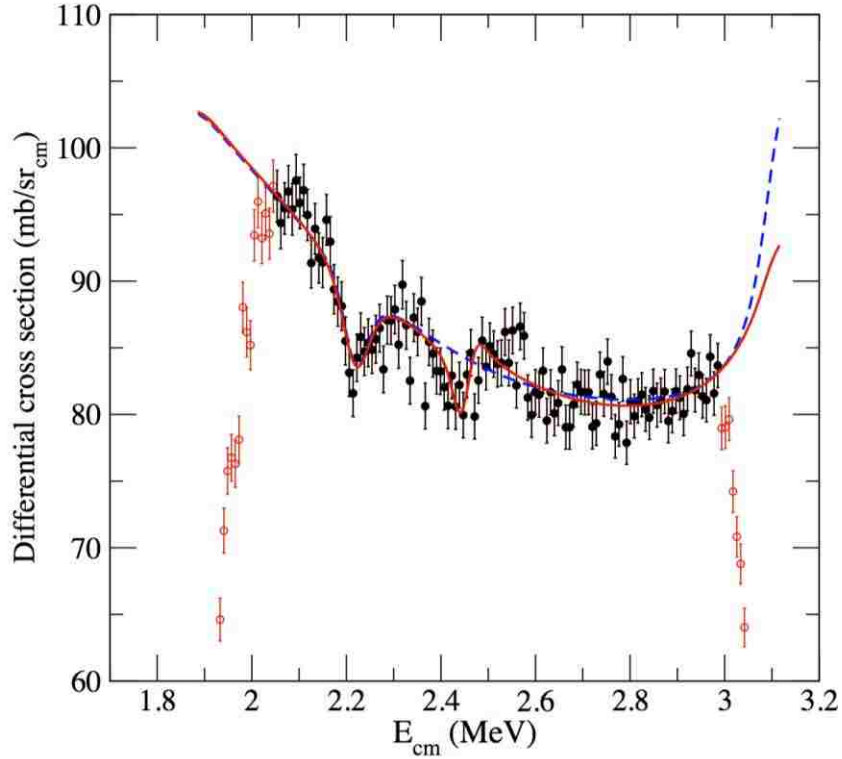
Figure 8-4 Same data as in 8-3, but shown in comparison to fits including a 1⁻ resonance in the energy range covered in the measurement (dashed blue curve) and including both a 1⁻ and 3⁻ resonance (solid red line).

Previous measurements indicate that the feature at E_{cm}=2.4 MeV is likely an unresolved doublet. The resonance at E_{cm}=2.2 MeV is well fit by a 1⁻ assignment as shown by the fits in Figure 8.4. If this is the case, then the doublet of states corresponding to the resonance at E_{cm}=2.4 MeV should have J^{π} of 2⁻ and 3⁻ based on mirror assignments and previous ^{18}Ne measurements. We first fit the data including just a single 2⁻ state near E_{cm}=2.4 MeV and achieve a significantly better fit to the data than using a 3⁻ state alone. The best fit is shown in Figure 8-5 as a solid blue curve, which corresponds to χ^2=97.6 (χ^2/ν=0.92 from an 11 parameter fit). While this is an excellent fit, it may not be a true representation of the data. The best fit parameters (given in Table 8-1) result in a width for the single 2⁻ resonance of Γ_p = 120 keV, in contradiction to studies of ^{20}Ne(p,t)^{18}Ne that indicate a much smaller width for this state (see Table 5-1). While we do not resolve two resonances near E_{cm}=2.4 MeV, the (p,t) measurements indicate two states with an energy difference of $\Delta E_{cm} \cong 50$ keV, and this likely gives rise to erroneous values for the widths when a single resonance is used in place of the doublet in our fit. Therefore, the data need to be fit using all 3 resonances in the region of interest to reliably extract the parameters for the states.
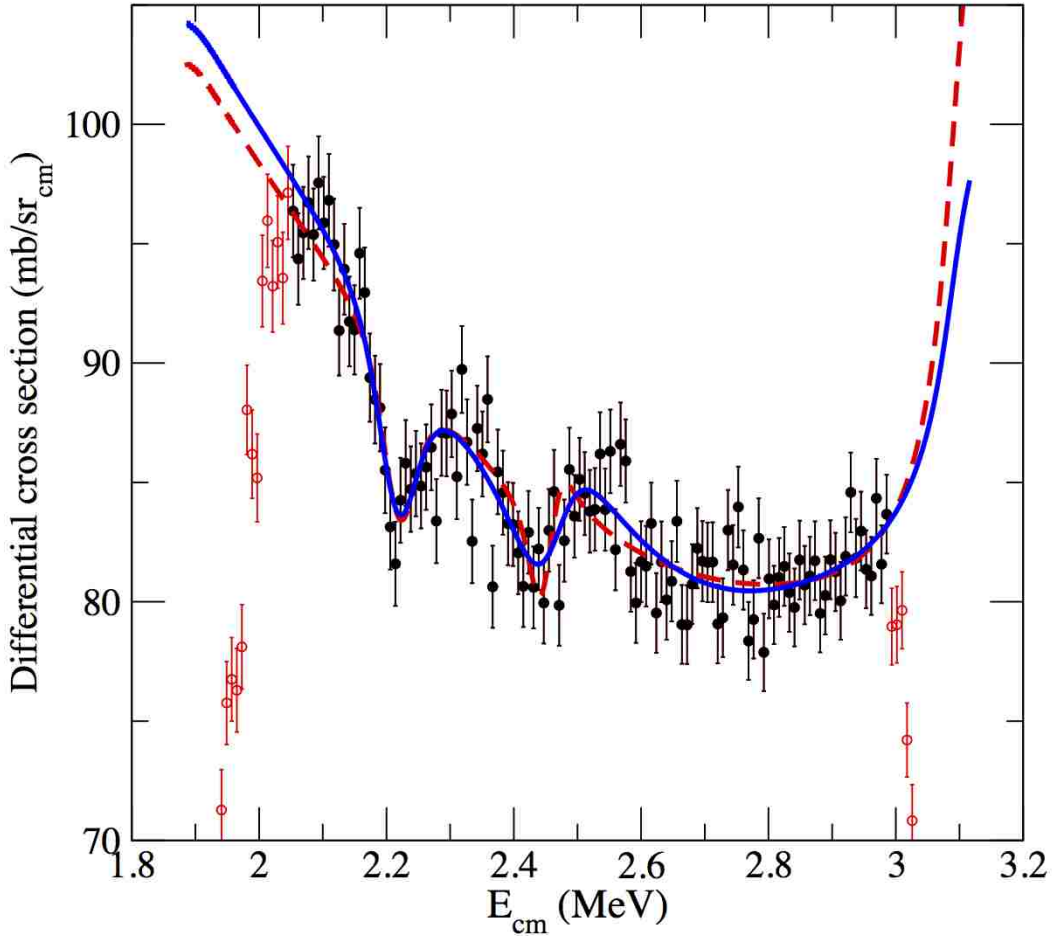
72

Figure 8-5: Same data as in 8-3, but shown in comparison to fit including both a 1⁻ and 2⁻ resonance (solid blue curve). The dashed red curve is the same fit shown in Figure 8.3 as a solid red curve (using 1⁻ and 3⁻ states) for comparison.

In Figure 8-6 we show a fit to the data using a 1⁻ state near E_{cm}=2.2 MeV and a doublet of 2⁻ and 3⁻ states near E_{cm}=2.4 MeV. The fit in this case is nearly identical in quality to that achieved using a 2⁻ state only. In this case the widths obtained for the 2⁻ and 3⁻ states are in better agreement with results from the two nucleon transfer reactions. However, there is another issue. Our best fit to the doublet of states has the highest energy resonance being a 3⁻ state, with the 2⁻ state at an energy of about E_{cm}=2.42 MeV. However, the previous $^{20}Ne(p,t)^{18}Ne$ data show that it is this state that is by far the most strongly populated of the 3 resonances, and can not have unnatural parity. For a fit to the data to be in agreement with previous results, we must require that the state near E_{cm}=2.42 MeV be natural parity. This then begs the question of whether a fit comparable to the best fit to the data can be achieved with such a requirement. Before we examine this question in detail, we should first comment on the uncertainties in the resonance parameters.
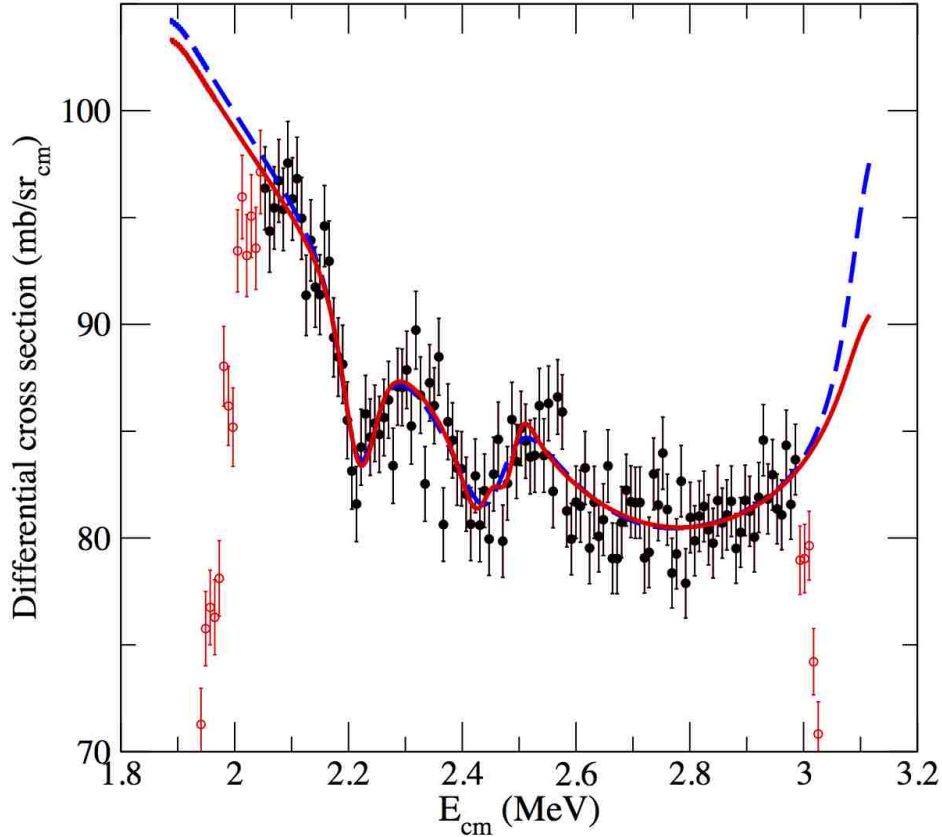
73

Figure 8-6 The best fit (solid red curve) using three resonances (1^-, 2^- and 3^-) is shown in comparison to the fit using only a (1^- and 2^- states) given by the dashed blue curve which was represented an a solid blue curve in Figure 8-5.

In order to determine the uncertainties in the properties of states allowed by our data, we varied the properties of parameters in the fit and evaluated the variation in χ^2 as a function of the parameter values. If parameters are uncorrelated, then the statistical uncertainty in each parameter can be determined by varying each parameter independently. This reduces the error determination to a 1 dimensional problem, and the 1σ uncertainty is determined when the value of χ^2 increases by 1. In our case, resonance structures near $E_{cm}=2.2$ MeV and $E_{cm}=2.4$ MeV are sufficiently well separated that it is a good approximation to treat parameters affecting each of the features as being independent from each other. However, the parameters for one state can not necessarily be treated as being independent of other parameters of that same feature. To properly assign the uncertainties associated with any one resonance, we simultaneously varied all of the parameters to evaluate the shape of the χ^2 function over the multidimensional surface and the correlations between parameters.

In the case of the resonance at $E_{cm}=2.2$ MeV, the resonance energy is fairly tightly constrained by our fit to the

data and is relatively independent of the partial widths. In Figure 8-7 we show a one dimensional slice through the χ^2 surface varying only the resonance energy and holding all other parameters fixed, essentially treating the resonance energy as an uncorrelated parameter. This results in $E_{cm} = 2.220 \pm 0.005$ MeV (1σ uncertainty). Other slices through the χ^2 surface give a similar result, which seems robust. It should be emphasized that this uncertainty in the resonance energy represents the statistical uncertainty only.

The partial widths of the $E_{cm} = 2.2$ MeV resonance are strongly correlated, and to determine the uncertainty in the partial widths we must examine the behavior of χ^2 over the parameter space. In Figure 8-8 we plot the change in χ^2 as a function of the ground state proton width, Γ_p, and the total width, Γ. The total width, Γ, is fairly tightly constrained, and we find that any change in Γ of more than 12 keV causes an increase in χ^2 of more than 1σ regardless of the partial widths. The relative partial widths themselves, however, are not well constrained except for a lower limit set on Γ_p. Specifically, we find $\Gamma = 45 \pm 12$ keV (with 1σ uncertainty) and $\Gamma_p > 15$ keV with 90% confidence. This is logical given the effect of these parameters on the resonance structure observed in the elastic scattering cross section. The parameter Γ_p determines the coupling of the resonant state to the entrance channel and essentially sets the depth of the resonance, while the total width essentially sets the total width of the resonance. Our sensitivity to Γ_p is reduced due to the limited energy resolution in the measurement that results from straggling in the silicon ΔE detector.

With these results for the 1- state, an interesting question is whether a satisfactory fit for the doublet can be found that is in agreement with previous measurements. As previously discussed, we find a best fit with the highest energy resonance being natural parity. However, this appears to be in strong contradiction to the results from ^{20}Ne(p,t)^{18}Ne. To better understand this issue we have studied the behavior of our R-matrix calculations throughout the six dimensional parameter space that determines the shape of the resonance structure at $E_{cm} = 2.4$ MeV. In this exercise we have restricted the highest energy resonance to be 2⁻, with a 3⁻ state somewhat lower in energy. With this restriction, we are able to obtain a comparable description of our data to those shown in Figure 8-8 with the highest energy state being 2⁻, but such a fit also requires a relatively broad width for the highest energy 2⁻ state. In Figure 8-9 we show our best fit to the data with the requirement that the highest energy resonance be 2⁻. In Figure 8-10 we show a 2D slice through the χ^2 surface where we vary the energy of the 2⁻ resonance and its total width. There
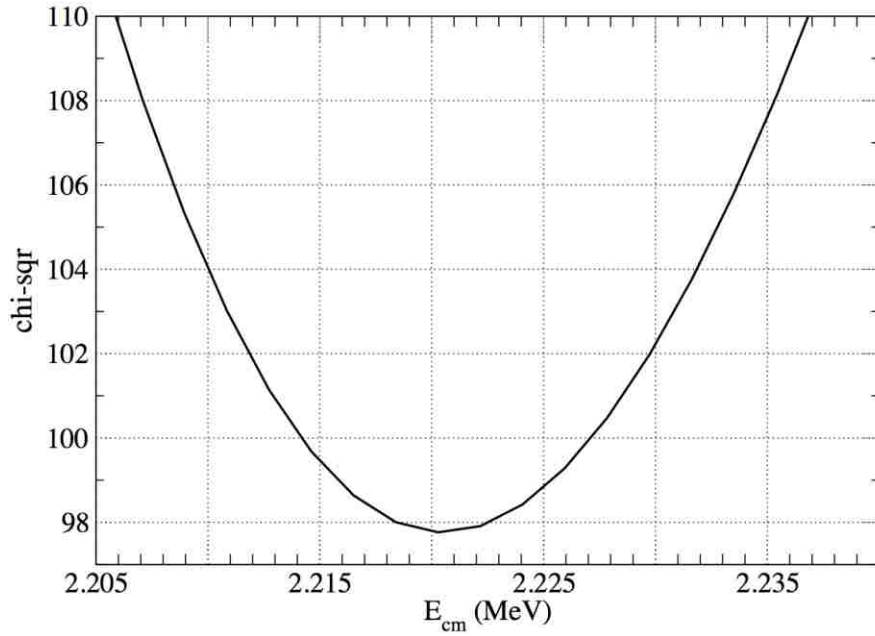
Figure 8-7 The best energy fit for the 1⁻ state was determined by the minima in a chi-square versus E_{cm} graph.
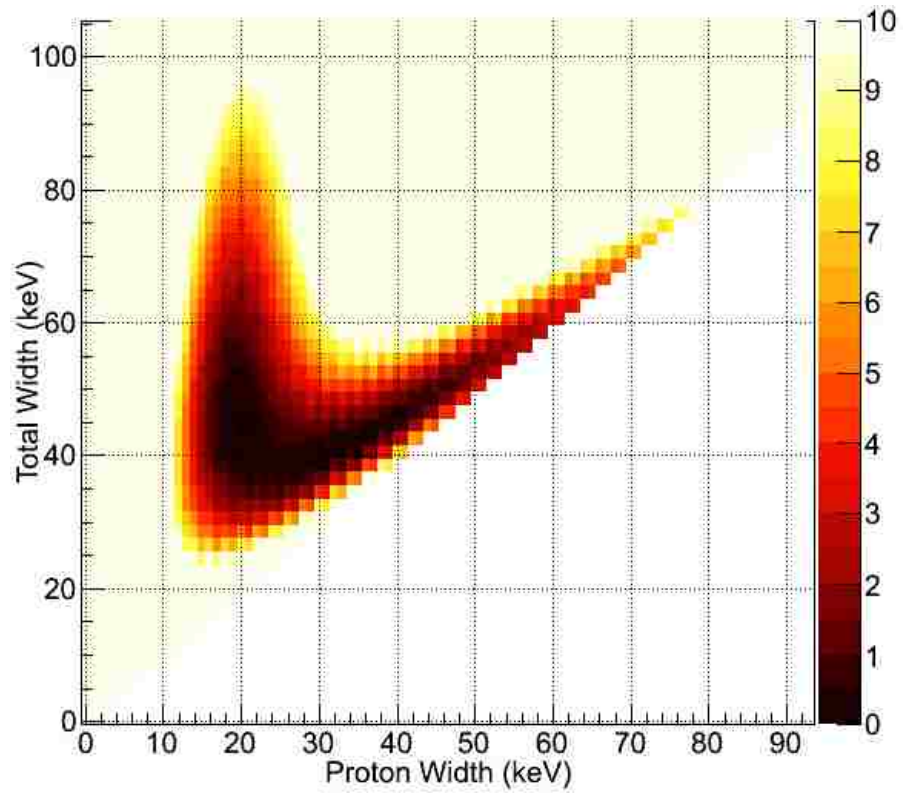
Figure 8-8 The change in χ^2 from the best fit is plotted against Γ_p and Γ for the 1⁻ state at $E_{cm} = 2.2$ MeV.
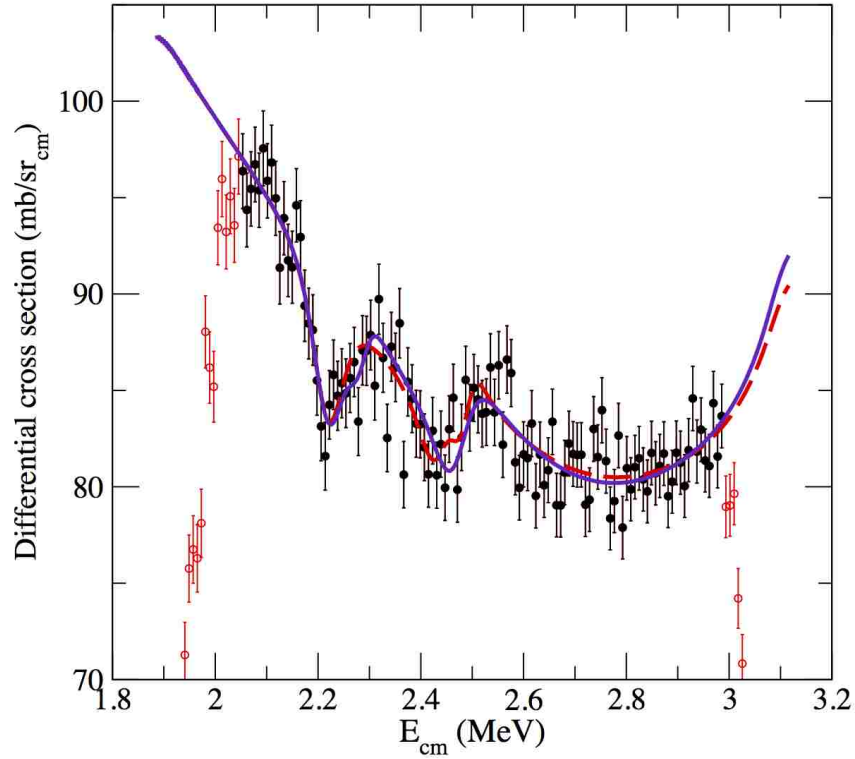
Figure 8-9 Fit to the data with states of 1⁻, 3⁻, and 2⁻ in order of increasing energy (solid blue line) is compared to fit with ordering of 3⁻ and 2⁻ states reversed (dashed red curve), which is same as solid red curve in Figure 8-6.

Figure 8-10 A 2D plot of Proton Width versus E_{cm} for a higher energy 2⁻ resonance, where E_{cm}=2.451 (0.008) MeV and Γ_p=87 (15) keV.

is some correlation between the parameters, and we adopt values for the 1σ uncertainties that encompass all the parameter space with a total χ^2 within 1 of the best fit values. We thus find E_{cm}= 2.451 (0.008) MeV and Γ_p = 87 (15) keV. Our results for the resonan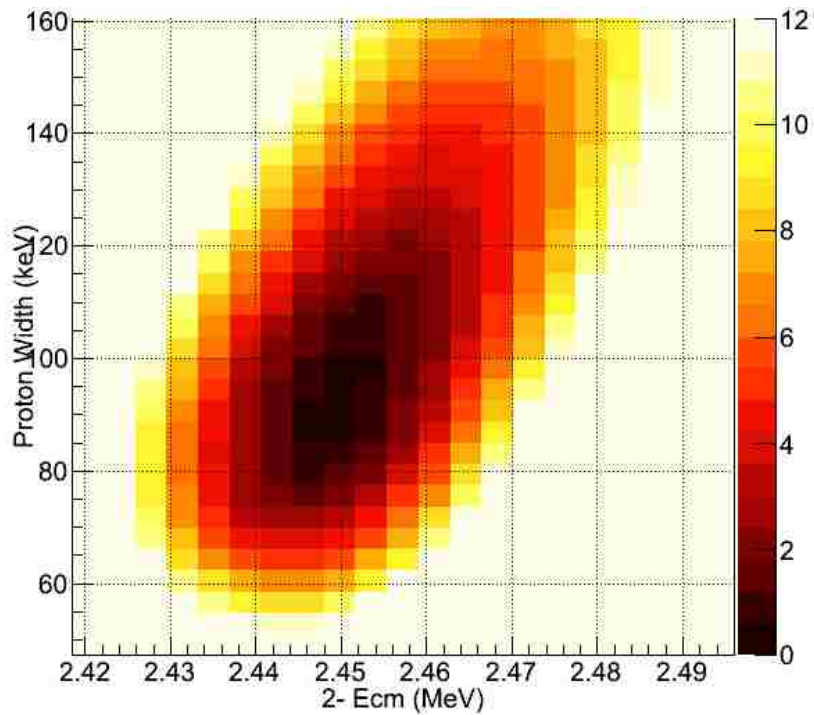ce energy are in fairly good agreement with previous results (See Table 5-1), but we find a total width for the 2⁻ resonance that is nearly 3σ greater than the measurement of [Par99]. It is worth noting that the 2.45 MeV resonance is significantly broader than the 2.22 MeV resonance, indicating that we are likely not limited by instrumental resolution.

It should also be noted that the broad width we observe for the 2.45 MeV state can not be attributed to the neighboring 3⁻ state. In fact, we are able to set a fairly restrictive limit on the width of the 3⁻ state from our data since an increase in the width of the 3⁻ state results in a quite pronounced structure in the elastic scattering cross section. To illustrate this fact, in Figure 8-11 we show another slice through the χ^2 parameter space where we vary the energy and width of the 3⁻ state. We are not able to place a good constraint on the energy of the 3⁻ state since it is not resolved from the 2⁻ state; however, we are able to set an upper limit on its width of Γ_p < 4 keV at the 90% confidence level. Note that while it appears from Figure 8-11 that we observe a width that is statistically different from zero, this is not the case as parameter slices with a larger width for the 2⁻ state can produce a similar fit with a negligible or even zero width for the 3⁻ state, as is illustrated by the fit shown in Figure 8-5 and 8-6. Thus, we can not claim observation of the 3⁻ state, but do set a significant upper bound on its width.

All uncertainties quoted thus far are purely statistical in nature. The dominant systematic uncertainty in the resonance energies comes from the alpha energy calibration. The 5 alpha lines used for calibration provide an accurate measure of the energy alphas deposit in the sensitive volume of the silicon detector over a range of energies comparable to those of the protons of interest. However, the silicon strip detectors have a thin dead layer on the surface that results in the detected alpha energy being slightly less than incident alpha energy. Calculations of the alpha energy loss in this dead layer using the manufacturers specifications indicate that the alpha energy is degraded by about 70 keV before entering the sensitive region of the detector. Previous experience with the dead layer on the detectors indicates that this correction could be as large as 100 keV. To account for this dead layer, we adjusted the alpha energies to account for the energy loss by the manufacturers specifications, and include a 30 keV systematic uncertainty on the resonance energies resulting from this uncertain dead layer. This uncertainty spans the range of any realistic corrections, and is consistent with no correction at the 2 sigma level. This systematic uncertainty in the
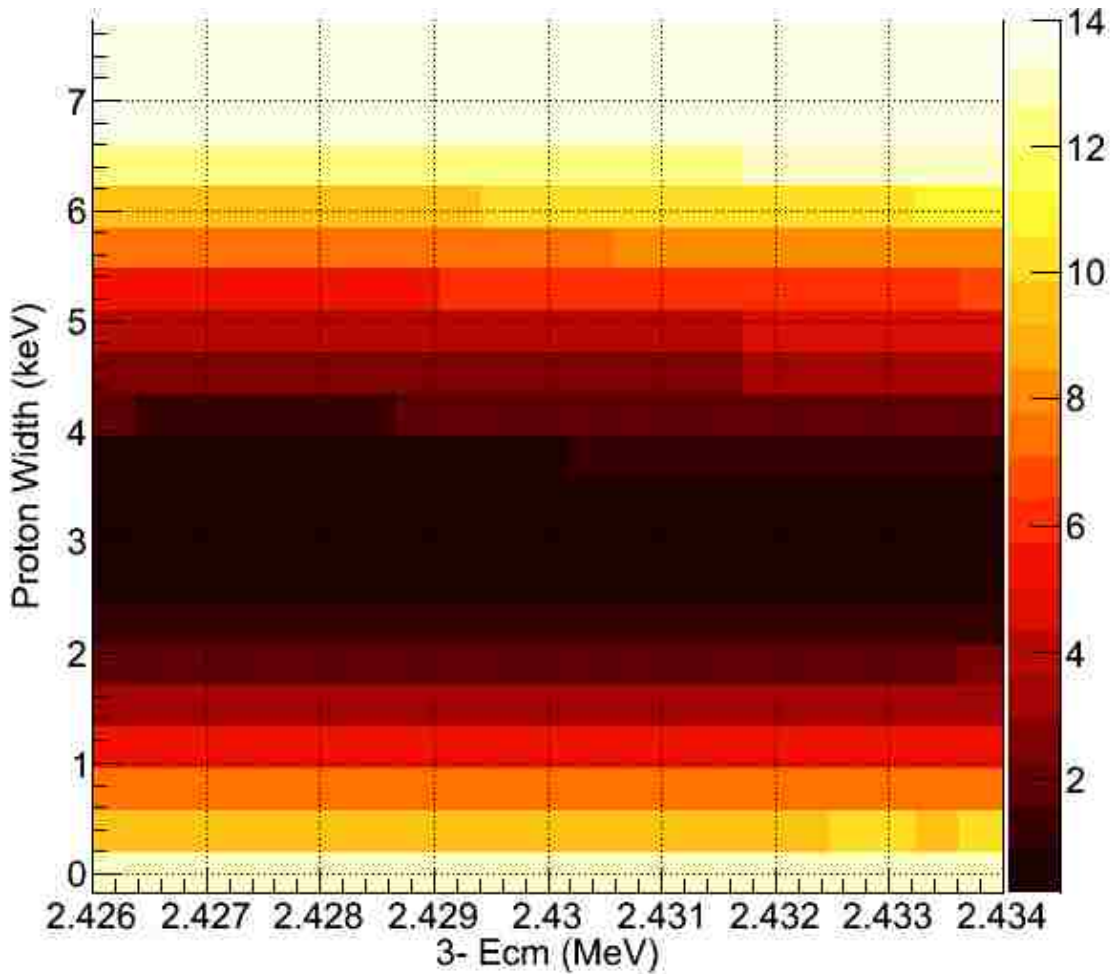
Figure 8-11 A comparable plot for the characteristics of the 3⁻ state. We do not resolve the 3⁻ from the neighboring 2⁻ state but are able to set an upper limit on its width of $\Gamma_p < 4$ keV (90% confidence level).

energy calibration translates to a systematic uncertainty in the measured resonance energies (in the center-of-mass frame) of 8 keV.

It should be noted that the previous measurements of the width of the 2⁻ state come from studies of the (p,t) transfer reaction which much more strongly populates the neighboring, narrow, natural parity 3⁻ state. The relatively broad width of the 2⁻ state, and its close proximity to the more strongly populated 3⁻ state make it challenging to reliably extract widths from this doublet of states from the (p,t) study. However, the different shapes resulting of the interference of the 2⁻ and 3⁻ states with Rutherford scattering provide a different sensitivity as the width of the resonance is related to the amplitude of the structure and not just its width.

With the systematic uncertainty given above, our final results for the observed excitation energies are 6142 $(5)_{stat}$ $(8)_{sys}$ keV (1⁻) and 6373 $(8)_{stat}$ $(8)_{sys}$ keV (2⁻), in agreement with previous measurements with comparable total

uncertainty. It should be noted that the systematic uncertainty in our resonance energies is an overall shift and does not effect the energy difference between the 1$^-$ and 2$^-$ states, which we find to be 231 (9) keV. This is in excellent agreement with the difference 224 (5) keV obtained if we take the most accurate previous values for the 1$^-$ resonance of 6134 (1) keV [Bar12] for the 2$^-$ resonance of 6358 (5) keV [Par99]. It should also be noted that our systematic uncertainty does not affect the partial widths extracted for the states observed. Only factors that contribute to the energy resolution of our experiment could affect the uncertainty in the total widths extracted, and we estimate these to be negligible compared to the systematic uncertainties in our extracted widths.

Finally, let us now return to an assumption that we made when we began our analysis of the data. When we first fit the E_{cm} = 2.2 MeV resonance, we began by assuming that it resulted from a 1$^-$ state in ^{18}Ne. As discussed previously, this assignment is somewhat controversial, and a 2$^-$ assignment is also possible. An important question to investigate is whether our data are consistent with a 2$^-$ assignment for the E_{cm} = 2.2 MeV resonance. While it is not possible to produce a maximum in the elastic scattering excitation function from a 1$^-$ resonance, which only allows channel spin 2$^+$ in the entrance channel, it is possible to fit a minimum with either a 1$^-$ or 2$^-$ assignment. We fit our data with the requirement that the lowest energy resonance corresponding to the structure at E_{cm} = 2.2 MeV corresponds to a 2$^-$ state in ^{18}Ne, and fit the doublet of states corresponding to the structure at E_{cm} = 2.4 MeV with a 1$^-$ and 3$^-$ state. We are able to obtain a nearly comparable fit with this assignment, and a fit to the data is shown in Figure 8-12 in comparison to the fit with the 2.22 MeV state being a 1$^-$ state. The resonance parameters are also compared in Table 8-1. While overall the fit is comparable, to fit the higher energy structure with a 1$^-$ resonance requires a quite broad width for the 1$^-$ state. This width is in strong contradiction to the width extracted from (p,t) transfer reaction studies. This middle 2.4 MeV resonance corresponds to the state that is very strongly populated in ^{20}Ne(p,t)^{18}Ne, and the constraint on the width of this state is much more robust than for the much weaker state at higher energies. In addition, one of the strong arguments [He10b] for a 2$^-$ assignment for this resonance is the shape of the resonance structure (a maximum) observed in a previous measurement of ^{17}F(p,p)^{17}F elastic scattering that used a similar technique as ours (see Figure 5.2) [Gom00]. The structure observed in our data is not consistent that that of Reference [Gom00], exhibiting a very different shape of the excitation function in the region of the E_{cm} = 2.2 MeV resonance. Therefore, the results of our experiment provide another piece of strong evidence that favors a
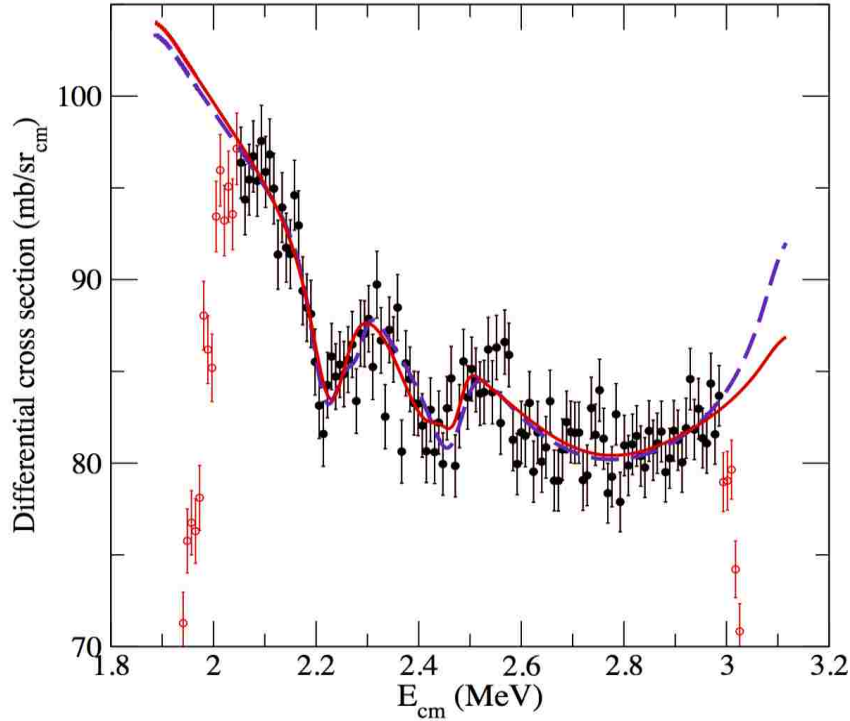
Figure 8-12 Fit to the data with states of 2⁻, 1⁻, and 3⁻ in order of increasing energy (solid red curve) is compared to fit with ordering of 1⁻, 3⁻ and 2⁻ (dashed blue curve), which is same as solid red curve in Figure 8-9.

1assignment for the 6.13 MeV state in ^{18}Ne. The best approach to finally and conclusively establish the spin assignment of this resonance is to directly measure the resonance yield of the ^{14}O(α,p)^{17}F reaction, or the inverse ^{17}F(p,α)^{14}O reaction.

8.2 Alpha Analysis

One conclusive way to assign the spin parity of the 1⁻ and 2⁻ states is through a measurement of the ^{17}F(p,α)^{14}O reaction that cannot populate unnatural parity states in ^{18}Ne due to angular momentum conservation. The ^{17}F(p,α)^{18}Ne reaction is the time inverse of the ground state branch of the ^{14}O(α,p)^{17}F reaction, and the yield of alpha particles can also be used to determine the alpha width of the important 1- resonance once it is identified. We clearly distinguish alpha particles from other charged particles through ΔE-E particle identification in the silicon strip telescope as illustrated in Figure 7-6. We also are able to clearly identify recoiling oxygen ions in coincidence using the ΔE-E signals from the HIRC as is illustrated in Figure 7-8.

Figure 8-13 is a 2D graph of the alphas' total energy (MeV) found in the silicon telescope versus the oxygen ions' total energy as measured by the HIRC. The alpha graph is done with a standard one ring one segment
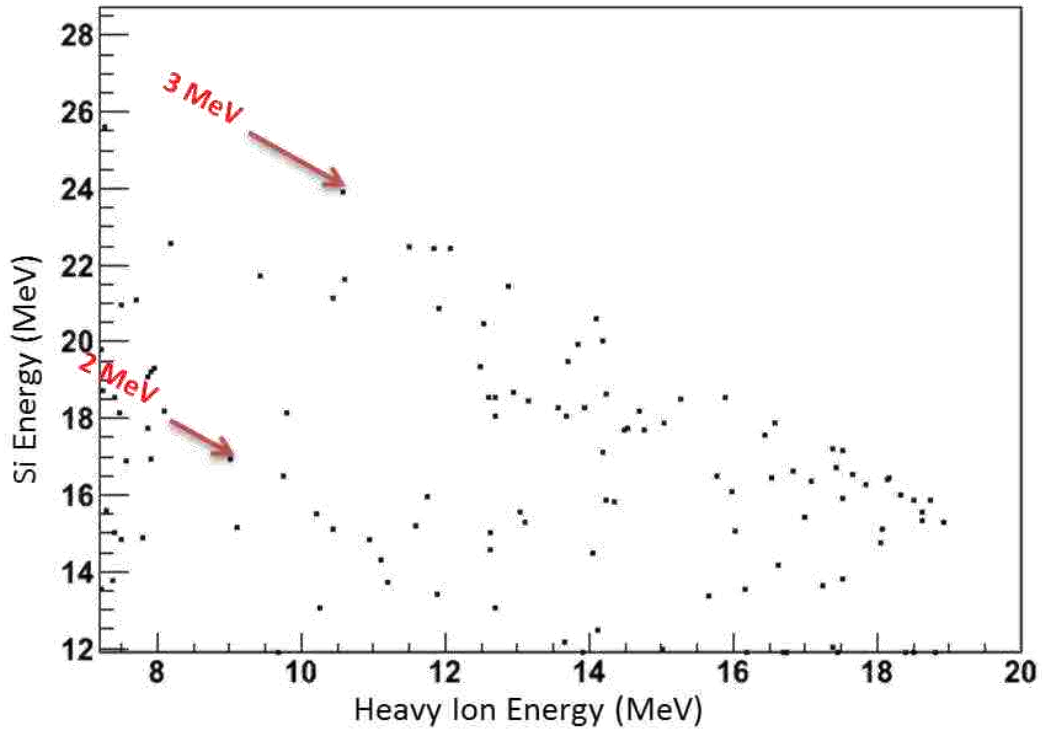
Figure 8-13 A graph of total silicon energy (MeV) of the alphas versus total HIRC energy (MeV) of the coincidence oxygen ions.

condition, time cut, alpha cut, and oxygen cut. This creates a scan of the region of interest measured by this experiment from the top right corner down to the bottom left corner of Figure 8-13. The two red arrows point down diagonal lines to show the center of mass energy that corresponds to the lab energies detected. As expected, there is a steady decrease of $^{17}F(p,\alpha)^{14}O$ particle reactions as a function of center of mass energy. Resonances in $^{17}F(p,\alpha)^{14}O$ reaction would be distinguished in this plot as lines with negative slope corresponding to an unique sum energy. At a close regard, there is no clear resonant structure that can be observed through the alpha data in the region of interest. Unfortunately, over the course of our experiment we only detect 88 documented alphas, and the statistics seen are not sufficient to allow resonant states to be identified by the $^{17}F(p,\alpha)^{14}O$ yield.

CHAPTER 9. THE DEVELOPMENT OF ANASEN

9.1 ANASEN Improvements

The ^{17}F+p scattering experiment was the first radioactive ion beam experiment towards the development of ANASEN. Since that time, we have continued to develop and commission ANASEN. A campaign of experiments was completed between the summer of 2011 and the spring of 2013 during which time we gradually implemented new components of ANASEN. These experiments included measurements of ^{19}O(d,p)^{20}O, ^{6}He+^{4}He scattering, and a measurement of ^{18}Ne(α,p)^{21}Na. We briefly summarize some of these experiments and the development of ANASEN here.

First, we changed the design of the HIRC to increase its acceptance and improve efficiency we moved from a 1mm spacing between the wires to double that to 2 mm. Then we add position sensitivity by developing circuit board anodes to replace the first two anodes in the ionization chamber, shown in Figure 9-1. These circuit boards were made with 34 pads across the top of a central 13.49 cm squared-window in 21.59 cm diameter circuit board, shown in Figure 9-2. The pads have the dimension of 2 mm (height) x 3 mm (laterally across the window). There is a 1 mm gap in between the pads. We place the thin (20 μm) gold coated tantalum wires 2mm apart, attaching two wires per pad. The wires were best attached to the circuit board with regular solder and then A12 double compound epoxy over the top of the solder joints. The wires were attached on the opposite side of the window by the same A12 epoxy. Each pad was traced as in individual signal to a 2x17 regular-density male-male right angle-header with a shroud. The first two anodes in the new HIRC are circuit board anodes, rotated by 90° from each other. The signals are routed out in a circuit board feed thru and read by LSU-72 channel preamp box. This manner leaves 8 extra channels that can be used for up to 8 non position sensitive anodes from the new ionization chamber. We also changed the design of the conductive rings used for the anodes and the grounding planes for the remainder of the HIRC to a larger circular ring with a 7 inch diameter opening to increase the acceptance of the HIRC.

9.2 The ^{19}O(d,p)^{20}O Experiment

The second ANASEN commissioning experiment used a compact setup of the ANASEN Super-X3 detectors in conjunction with S2 annular strip detectors at forward and backward directions, respectively. This created a wide angular coverage for the measurement of the ^{19}O(d,p)^{20}O reaction. This experiment provides the first data using the position-resolution of the Super-X3 detectors and is being used to develop the calibration and analysis software for

Figure 9-1 A picture of the full heavy ion recoil chamber innards attached to a NW250 flange, complete with two position sensitive circuit boards.
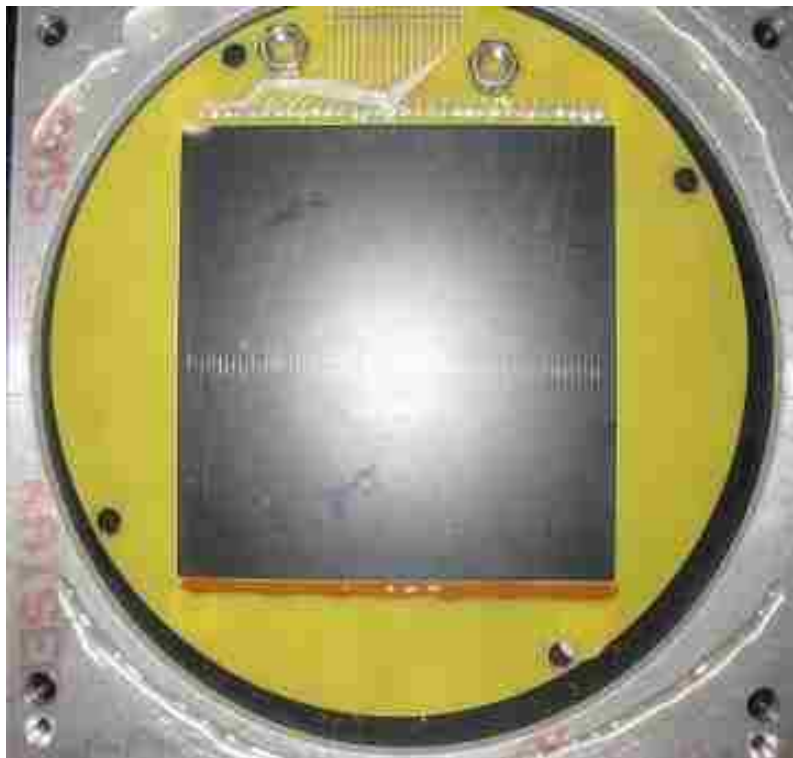

Figure 9-2 A close-up picture of the position sensitive circuit board for the heavy ion recoil chamber.

these detector systems. This experiment forms part of the Ph.D. thesis of FSU student Daniel Santiago-Gonzalez, who graduated in 2013 and is now a post doctor researcher with the LSU nuclear physics group.

The location of the neutron-drip line in the oxygen isotopes is a very fruitful ground for the study of the nuclear mean-field in exotic nuclides. The excitation energy of the $d_{3/2}$ orbital determines the location of the drip line. The fact that ^{28}O is unbound, which contradicts most mean-field calculations, has recently been attributed to the importance of three-body interactions on the energy of loosely-bound orbitals [Ots10].

In this experiment with the early-implementation of the ANASEN setup (performed in July 2011), we measured the angular distribution of the ^{17}O(d,p)^{18}O and ^{19}O(d,p)^{20}O reactions in order to determine the $d_{3/2}$ spectroscopic factors of excited states of ^{20}O. A recent experiment performed with the HELIcal Orbit Spectrometer (HELIOS) at Argonne National Laboratory used the same reaction to study the spectrum of low-lying states up to 6 MeV in excitation energy. [Hof12]. Figure 9-3 displays spectra obtained from our experiment, which identifies the states observed in [Hof12]. In addition, we observe a strongly populated, unbound 4^+ state at 7.75 MeV, which is expected to be based mainly on $d_{5/2}$ x $d_{3/2}$ configurations. The forward angle detectors show a large amount of background from protons produced in fusion-evaporation and from elastic scattering from the small ^{1}H contaminant in the CD_2 targets. The data analysis is in progress, with the aim of reducing the background in the forward detectors through a tighter coincidence requirement with the energy of the recoiling particle.

In the spring of 2102, we also remeasured this experiment with the complete ANASEN gas-filled system using a pure D_2 gas as target that provided a much increased angular coverage, a higher yield and better efficiency beyond the 7.75 MeV state.

9.3 ^{4}He(^{6}He,^{6}He)^{4}He

Clustering in A=10 nuclei has attracted a lot of attention recently due to the exciting possibility that a molecular-type configurations with valence nucleons "orbiting" the two center α−α core may play an important role. It has been suggested that the 6.179 MeV 0+ state in ^{10}Be has an extended α:2n:α configuration. The rotational band with an unusually large moment of inertia that is built on this 0+ state with a 2+ member at 7.54 MeV and 4+ at 10.15 MeV has been identified [Fre06]. Existence of the 6+ member of this rotational band was predicted in [Wol10]. We studied the structure of ^{10}Be using a beam of ^{6}He from RESOLUT with ANASEN in active gas target mode with ^{4}He gas with a small admixture of CO_2. This was the first measurement using helium gas in the ANASEN proportional counter. All components of ANASEN were used in the experiment except for the forward
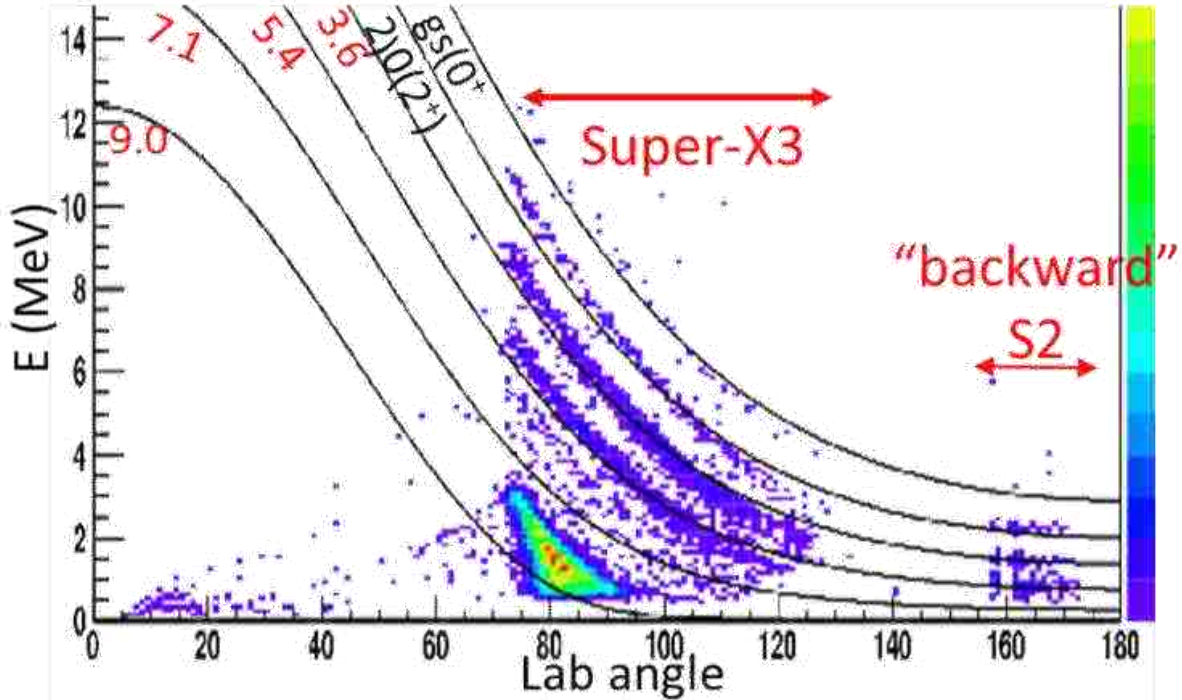
Figure 9-3 Proton energy (MeV) versus detection angle (degrees) reconstructed from the $^{19}O(d,p)^{20}O$ experiment, measured with the early implementation of ANASEN detectors. The data shows the two detector groups, one at backward angles, one around 90 degrees. Marked are the kinematic curves for the known states.

angle QQQ3detectors and the CsI detectors. The main goals of this measurement were to confirm the spin-parity assignment and large degree of clustering for the 4+ state at 10.15 MeV reported in [Fre06] and to search for the 6^+ member of the α:2n:α rotational band. The excitation functions for elastic and inelastic $^6He+^4He$ scattering were measured in the excitation energy range between 9 and 17 MeV. The 4^+ resonance was observed, and based on preliminary evaluation of the cross section data at peak energy its reduced alpha-width is very large (more than the alpha single-particle limit), in agreement with [Fre06]. Analysis of the higher energy excitation function is still in progress.

9.4 $^{14}N(α,p)^{17}O$ With Active Gas Target

The position-sensitive proportional counter is a key component of ANASEN that provides for tracking capability making ANASEN an active target detector. We performed initial tests of the active gas target approach using elastic scattering reactions. In 2013, we performed our first test measurement of an (α,p) reaction using the active gas target mode. A 30 MeV beam of ^{14}N from the FSU tandem accelerator entered the ANASEN target chamber through a thin kapton window. The ANASEN chamber was filled with ^4He gas with a small (1%)

86

admixture of CO_2. Charged particles are detected by 19 7-µm-diameter carbon-fiber anode wires, arranged cylindrically around the beam axis, and by the ANASEN silicon-strip detectors.

Protons and alpha particles were easily identified by their energy loss in the proportional counter. The center-of-mass energy for each reaction was determined on an event by event basis from the trajectory of the ions based upon their position as measured by the proportional counter and by the silicon strip detector. In addition, the measured energy of the particles in the silicon allows the excitation energy of the final state to be determined. This complete excitation function was measured simultaneously with a center of mass energy resolution of roughly 70 keV FWHM.

9.5 ANASEN at the NSCL

The successful first campaign of experiments with ANASEN at FSU was brought to a close in March of 2013. In April the ANASEN detectors and electronics were moved to the National Superconducting Cyclotron Laboratory (NSCL) on the campus of Michigan State University to be used in the first commissioning experiments with low energy accelerated beams from the new ReA3 Facility under development there. A new set of hardware (vacuum chambers, pumps and supporting infrastructure) was developed at LSU and transported to the NSCL in preparation for arrival of the detectors. The ANASEN installation at the NSCL was completed in April-June of 2013. A photograph showing ANASEN at ReA3 is shown in Figure 9-4.

The first stable low energy beams were delivered to ANASEN in July of 2013 for commissioning and development. A beam of $^{16}O(q=7^+)$ from the Electron Beam Ion Trap (EBIT) Charge-Breeder was mass analyzed and accelerated by the RFQ and ReA3 Superconducting linac to 2.4 MeV/u before being transported through the L-Line and newly completed L-Line Extension beamline and delivered to the ANASEN target. The incident ^{16}O beam was scattered from a thin carbon target and detected in the ANASEN silicon strip detectors. The beam energy spread was determined from the measured width of the elastic scattering peak shown in the forward silicon strip detector array and found to be less than or about 2% (FWHM), in good agreement with expectations for the accelerator performance.

Next proton elastic scattering was measured using a ^{12}C beam from the EBIT and ReA3 accelerator to bombard a thick, polypropylene target. The center of mass energy was determined from the measured energy and lab angle of each particle using an approach that was similar to that used for the $^{17}F+p$ elastic scattering experiment and will be employed for the first radioactive ion beam experiments using beams from the ReA3 facility. The calculated center-
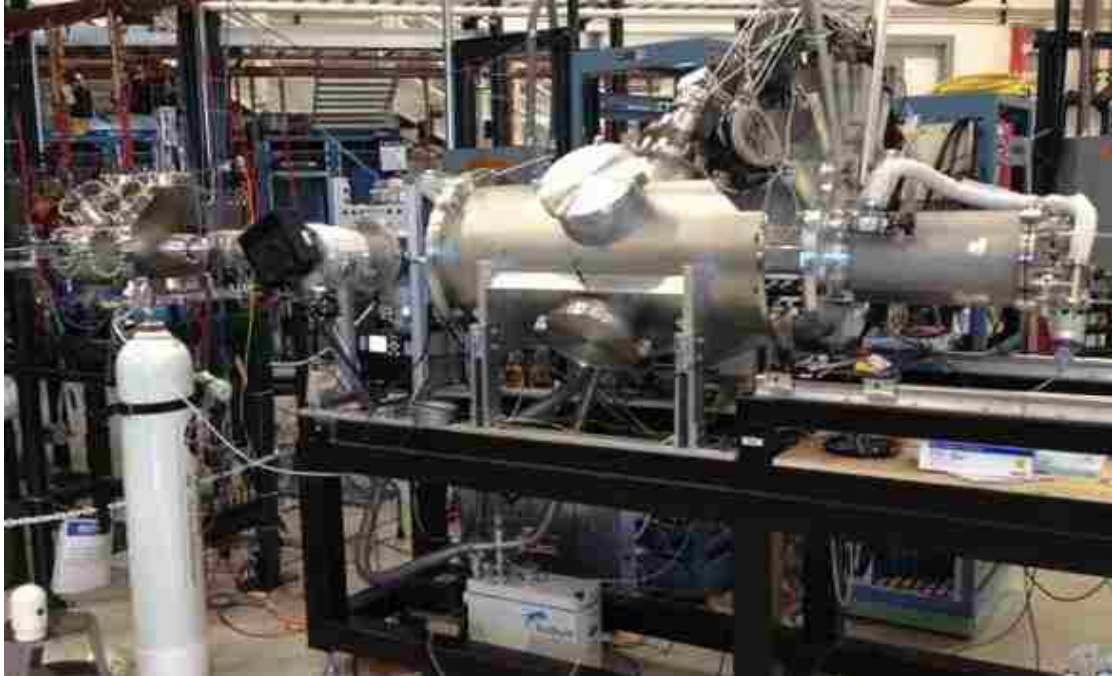
Figure 9-4 A photograph of ANASEN at MSU's NSCL.

of-mass energy spectrum is shown Figure 9-5. The sharp peak at 5.2 MeV in the lab frame corresponds to the well-known doublet of states, $\frac{5}{2}^+$ and $\frac{3}{2}^-$, in ^{13}N at 3.5 MeV excitation energy. The excellent energy resolution obtained shows that the combination of reaccelerated beams from the ReA3 facility with ANASEN provides a sensitive technique for observing resonant structures via elastic scattering.

In August of 2013 ANASEN was used in the first experiment using reaccelerated radioactive ion beams from the ReA3 facility at the NSCL. A beam of ^{37}K (half-life of 1.2 s) with an energy of 2.3 MeV/u bombarded a solid 1.2 mg/cm^2 CH$_2$ target. Elastically scattered protons were detected by the ANASEN silicon strip detectors in coincidence with recoiling heavy nuclei in the gas ionization chamber located downstream around zero degrees. The experiment was designed to search for strong resonances in ^{38}Ca, relevant for the $^{37}K(p,\gamma)$ reaction that is important for X-ray bursts. The average intensity of the ^{37}K beam was about 300 particles per second, which was contaminated with a similar intensity of ^{13}C ions. A particle identification plot from the gas ionization chamber showing energy loss in the first segment of the ionization chamber versus total energy is shown in Figure 9-6. Use of the gas ionization chamber at zero degrees was crucial for distinguishing scattering events initiated by ^{37}K from those initiated by ^{13}C. While the statistics obtained (totaling about 1000 $^{37}K+p$ coincidence events) are relatively low in this short run, this experiment demonstrates both strengths and challenges to be addressed in the future experimental
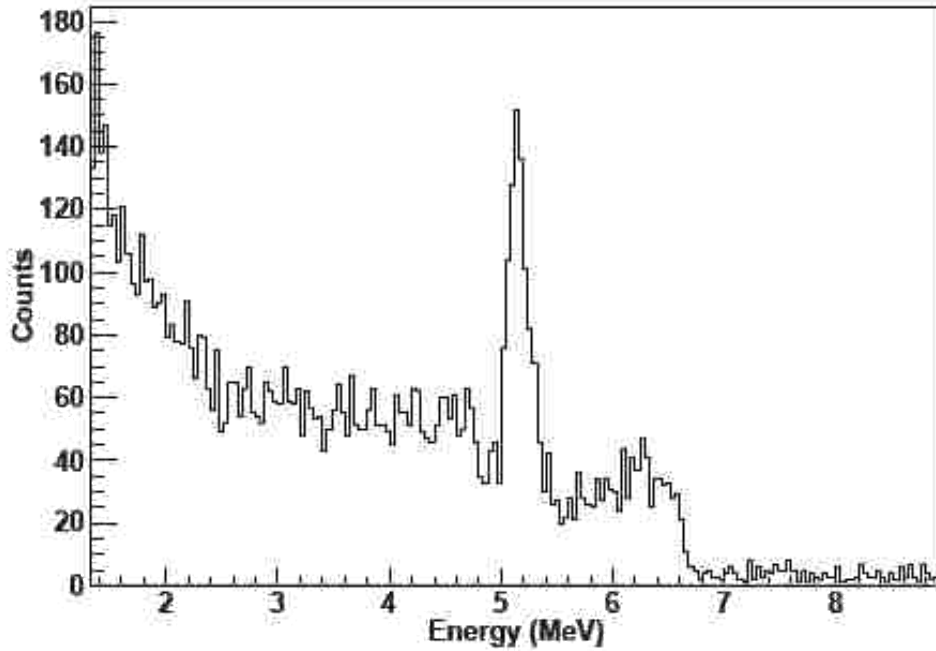
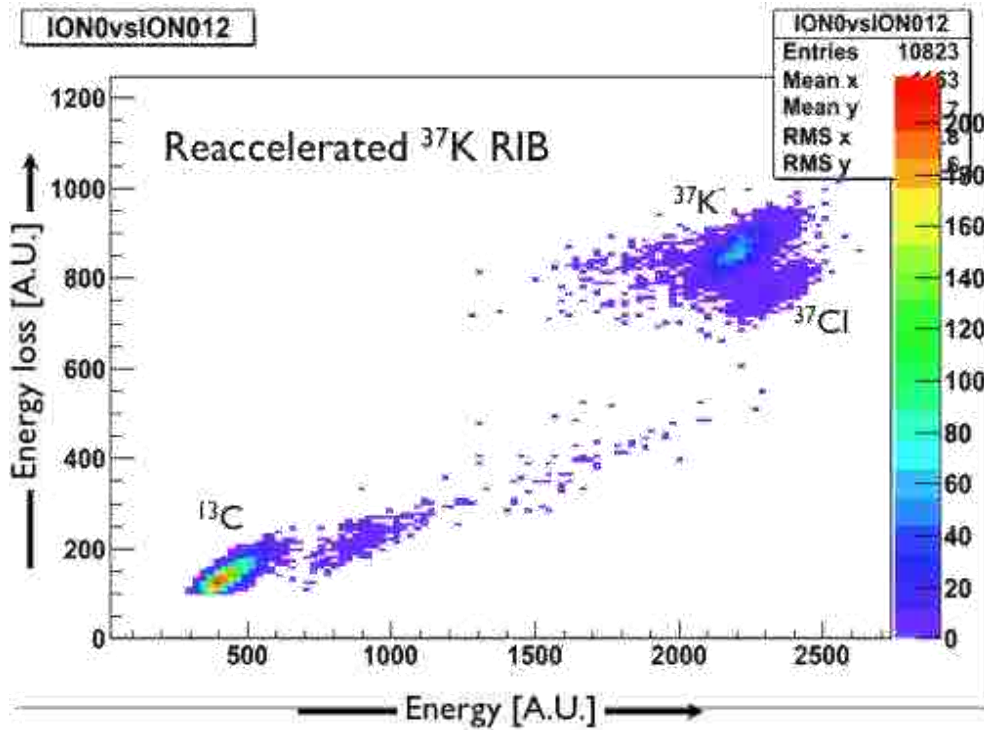Figure 9-5 Counts versus center of mass energy with a ^{12}C beam.

Figure 9-6 Relative Energy Loss [Arbitrary Units] versus Energy [Arbitrary Units] for a ^{37}K beam bombarding a CH$_2$ target at the ReA3 facility at the NSCL.

program. For example, the beam emittance and energy resolution coupled with the capabilities of ANASEN allow events to be reconstructed in the center-of-mass with high resolution even using a thick target. However, the time structure of the EBIT results in challenges in detecting and identifying events with a beam of mixed composition. The development of intense beams with better purity and time structure will be a focus of future work. We have developed and submitted a proposal now under consideration by the NSCL PAC to remeasure the ^{37}K+p elastic scattering reaction that will form the basis for the thesis of a future LSU student.

CHAPTER 10. SUMMARY

The LSU-FSU Array for Nuclear Astrophysics and Structure with Exotic Nuclei (ANASEN) is an array of charged-particle detectors that enables reaction studies with radioactive ion beams to measure the resonant properties that are needed to understand the most important reactions occurring in novae and X-ray bursts. ANASEN is designed to be used primarily for direct measurements of (α,p) reactions and indirect studies of resonant properties using reactions like proton elastic and inelastic scattering using radioactive ion beams. Measurements with a partial implementation of ANASEN were first performed at the RESonator SOLenoid Upscale Transmission (RESOLUT) radioactive beam facility of FSU during the summer of 2011. This included stable beam commissioning experiments and measurements of the ^{17}F(p,p)^{17}F and ^{17}F(p,α)^{14}O reactions that are important for understanding the structure of ^{18}Ne and the ^{14}O(α,p)^{17}F reaction rate. We used a 55 MeV beam of ^{17}F to bombard a 2 mg/cm^2 thick polypropylene target. Scattered protons were detected in a silicon strip detector array in coincidence with recoiling heavy ions detected in a gas ionization chamber that provided clean identification of the reaction channels.

In this thesis we presented an analysis of the ^{17}F(p,p)^{17}F proton scattering data from 2.053 through 2.985 MeV center of mass energy. The measured cross sections were fit with theoretical cross sections using phenomenological R-matrix theory. We conclusively observe two resonances. One corresponds to a 1^- state in ^{18}Ne, and we determine this state to have an $E_x = 6142$ (5)$_{stat}$ (8)$_{sys}$ keV with total width $\Gamma = 45$ (12) keV. We are also able to set a lower limit on the proton partial width to the ground state of $\Gamma_p > 15$ keV at the 90% confidence level. We also observe a 2^- state that we determine to be at $E_x = 6373$ (8)$_{stat}$ (8)$_{sys}$ keV with a total width equal to the partial width to the ground state of $\Gamma = \Gamma_p =$ of 87 (15) keV. While we can not resolve a previously reported 3^- resonance in this same energy regime, we can set a stringent limit on its proton partial width to the ^{17}F ground state of $\Gamma_p < 4$ keV at the 90% confidence level.

One of the ways to resolve the 2^- and 3^- states would be a direct measurement of these states through a direct ^{14}O(α,p)^{17}F measurement using a gas helium target. The complete ANASEN setup includes an active gas target/detector which uses a position-sensitive annular gas proportional counter that allows direct measurement of (α,p) reactions in inverse kinematics. Since the completion of the ^{17}F experiment presented in this dissertation, a campaign of experiments was completed between the summer of 2011 and the spring of 2013 during which time we

gradually implemented new components of ANASEN. These experiments included measurements of ^{19}O(d,p)^{20}O, ^{6}He+^{4}He scattering, and a measurement of ^{18}Ne(α,p)^{21}Na.

In April 2013 the ANASEN detectors and electronics were moved to the National Superconducting Cyclotron Laboratory (NSCL) on the campus of Michigan State University to be used in the first commissioning experiments with low energy accelerated beams from the new ReA3 facility under development. The ANASEN installation at the NSCL was completed in April-June of 2013. In July and August of 2013 ANASEN was used in stable beam commissioning measurements and in a first measurement of ^{37}K+p elastic scattering using a 2.3 MeV/u beam of ^{37}K. We have developed and submitted a proposal now under consideration by the NSCL PAC to remeasure the ^{37}K+p elastic scattering reaction at higher energies that will form the basis for the thesis of a future LSU student. The development of ANASEN has now set the stage for a program of measurements that should improve our understanding of nuclear reactions that are important in X-ray bursts and classical novae.

REFERENCES

[Ade70] E.G. Adelberger and A.B. McDonald, Nucl. Phys. A **145** (1970).

[Bar99] D.W. Bardayan *et al.*, Phys. Rev. Lett. V **83** (1999) 45.

[Bar12] D.W. Bardayan *et al.*, Phys. Rev. C **85** (2012).

[Bay13] Daniel Baye and Pierre Descouvemont., The R-matrix theory in nuclear and atomic physics. Scholarpedia, 8(1):12360., (2013) revision #129959.

[Bla03] J.C. Blackmon *et al.*, Nuc. Phys. A**718** (2003) 127c.

[Cam01] J. Gomez del Campo *et al.*, Phys. Rev. Lett. **86** (2001) 43.

[Dav01] B. Davin, *et al.*, Nucl. Instrum. Methods Phys. Res. A **473** (2001) 302.

[Eng07] G. L. Engel, *et al.*, Nucl. Instrum. Methods Phys. Res. A **573** (2007) 418.

[Fis08] J.L. Fisker, H. Schatz and F.K. Thielemann Astrophys. J. Suppl. Series **174** (2008) 261.

[Fre06] M. Freer *et al.,* Phys. Rev. Lett. **96**, 042501 (2006).

[Gal08] D.K. Galloway *et al.*, Astrophys. J. Suppl. Series **179** (2008) 360.

[Hah96] K.I. Hahn *et al.*, Phys. Rev. C**54** (1996) 1999.

[Har02] B. Harss *et al.*, Phys. Rev. C**65** (2002) 035803.

[He10a] J. J. He *et al.*, arXiv:1001. 2053v1 (13 Jan 2010).

[He10b] J. J. He *et al.*, Nuc. Phys. A**834** (2010) 670c.

[He11] J. J. He *et al.*, Eur. Phys. J. A**47** (2011).

[Heg07] A. Heger *et al.*, Astrophys. J. **671** (2007) L000.

[Hof12] C. Hoffman *et al.,* Phys. Rev. C **85**, 054318 (2012).

[Ili97] C. Iliadis, Nuc. Phys. **A618** (1997) 166.

[Jun10] J. Sun-Jun *et al.*, Chin. Phys. Lett. V**27**, No.3 (2010).

[Kno00] G. F. Knoll, Radiation Detection and Measurement: Third Edition. Hoboken, NJ: John Wiley & Sons, 2000.

[Li76] T.K. Li, D. Dehnhard, R.E. Brown, and P.J. Ellis, Phys. Rev. C**13** (1976) 55.

[Mic14] Micron Semiconductor ltd, *Micron Catalogue Product Information for S2 DC Radial Detector*. March 1, 2014. http://www.micronsemiconductor.co.uk/pdf/s.pdf.

[Nel85] R.O. Nelson, E. G. Bilpuch, and G. E. Mitchell, Nucl. Instrum. Methods Phys. Res., Sect. A **236** (1985) 128.

[Pai07] S.D. Pain *et al.*, Nucl. Instrum. Methods Phys. Res. B**261** (2007).

[Par08] A. Parikh et al., Astrophysics J. S. S. 178, 110 (2008).

[Par99] S.H. Park *et al.*, Phys. Rev. C **59** (1999) 1182.

[Pep09] P.N. Peplowski *et al.*, Phys. Rev. C**79** (2009) 032801.

[Rol73] C. Rolfs, Nucl. Phys. A**217** (1973).

[Rol88] C. Rolfs and W. Rodney, Cauldrons in the Cosmos. University of Chicago Press, Chicago 1988.

[Sch99] H. Schatz *et al.*, Appl. Phys. Jour. **524** (1999) 1014.

[Sin83] L.M. Singh and H. L. Duorah, Astrophys. Space Sci., **143** (1983).

[Sta99] S. Starrfield. Physics Reports, V **311** (1999) 371.

[Str02] T.E. Strohmayer and C.B. Markwardt, Astrophys. J. 577 (2002) 997-345.

[SPM08] Subcommittee of Performance Measures, *Report to the Nuclear Science Advisory Committee*. August 11, 2008. http://science.energy.gov/~/media/np/nsac/pdf/docs/perfmeasevalfinal.pdf.

[Tar08] O.B. Tarasov and D. Bazin, Nucl. Instrum. Methods Phys. Res. B**266** (2008).

[Til02] D. R. Tilley *et al.*, Nucl. Phys. A 708 (2002) 3-163.

[Wol10] R. Wolsky *et al.,* Phys. At. Nucl. **73**, 1405 (2010).

[Wor13] H. Worpel, D.K. Galloway, and D.J. Price, Astrophys. J. 772 (2013) 94.

[Zam12] M. Zamfir, A. Cumming, and D.K. Galloway, Astrophys. J. 749 (2012) 69.

VITA

Laura Elizabeth Pratt was born in Texas. At age two, she moved to South Carolina, where she learned to swim and roller blade. After completing high school in South Carolina, she moved to New Orleans, Louisiana. While attending classes at Tulane University she enjoyed the food and parades of New Orleans. While she had a talent for science and math, her love of people made her decision to study physics unexpected. Her parents believed in power tools and using their children to help build and fix things around the house, this background helped secure her place in an experimental condensed matter laboratory. Laura found her talent, building experimental setups for research. In 2008, she graduated from Tulane University with a Bachelor's of Science in Physics.

Not done with research, Laura continued on to graduate school. Within a month of earning her Bachelor's, she joined the Department of Physics and Astronomy at Louisiana State University. Dr. Jeffery Blackmon convinced her to change fields, from condensed matter to experimental nuclear astrophysics; the idea of running particle accelerators in her free time was too tempting for Laura to pass up. Throughout the past six years, Laura worked in laboratories around the country, including Yale, Florida State University, Colorado School of Mines, Oak Ridge National Laboratory, and Argonne National Laboratory. Laura plans to graduate Spring 2014 with a PhD in Physics; her next project is yet to be determined.